Long-lived Spin Coherence in Radical Pair Compass Magnetoreception



Hamish Hiscock

A thesis submitted in partial fulfilment of the requirements

for the degree of Doctor of Philosophy

University of Oxford

Physical and Theoretical Chemistry Laboratory

Lady Margaret Hall

Trinity Term 2018

Abstract

Long-lived Spin Coherence in Radical Pair Compass Magnetoreception

Hamish Hiscock

Abstract of a thesis submitted for the degree of Doctor of Philosophy

The ability of night migratory birds to utilise the Earth's magnetic field as a directional cue is thought to arise from a light-activated radical pair reaction in the birds' eye. The field of magnetoreception encompasses a broad range of research areas, from behavioural experiments to theoretical studies. Unfortunately, the computational challenge presented by modelling the multinuclear organic radicals thought to be involved in the sensing mechanism severely hampers the interpretation of experimental results in the framework of the radical pair hypothesis. This thesis presents novel algorithms for more efficient simulation of multinuclear radical pairs as well as a discussion of the insights avilable from calculations using these new computational tools.

I first present improved algorithms for simulating radical pair reactions in a static external magnetic field. With these more efficient algorithms, I am then able to explore in more detail the behaviour of different radical pair systems, and discuss their potential relevance to magnetoreception in Chapter 4. In particular, I examine whether a highly accurate "compass needle" could arise from a radical pair sensor.

One of the most significant behavioural observations in the field of magnetoreception is the finding that exceedingly weak time-dependent magnetic fields can disrupt magnetic orientation in birds. The added complexity of a time-dependent interaction means that simulating the experimental conditions is a considerable challenge. In Chapter 3 I present a calculation method based on a reformulation of Floquet theory which remains the only viable algorithm for modelling multinuclear radical pairs in an oscillatory magnetic field. In Chapter 5 I discuss the effect of these weak time-dependent fields on different candidate radical pairs, and examine the compatibility of the observed behavioural results with the radical pair hypothesis.

Finally in Chapter 6 I present a new Information theory-based analytical tool which allows me to assess the accuracy of a radical pair compass without having to make assumptions about the signalling cascade. I consider how a radical pair compass would operate under low light conditions, and how the impact of the limited number of available photons could inform my computational analysis from previous chapters and in future work.

Acknowledgements

My first thanks must go to Profs. Peter Hore and David Manolopoulos for guiding and mentoring me throughout my DPhil, and keeping me to the highest standards of rigour and clarity.

Thanks also to the members of the Hore group over the last four years, who have not only offered useful sounding boards, but a tea time respite from the computer. In particular, Dr. Daniel Kattnig for many intriguing chats and all his (usually) excellent ideas. Also to Susannah Worster who has been in parallel with me these last four years and not only offered sage wisdom but put up with me on many conferences and trips.

To my family, my parents for their support and for providing a holiday destination for me to retreat to. And also to Tom for many discussions about science in general as well as our specific projects, and all his grand ideas.

Contents

1 Introduction **1**

I The radical pair mechanism . . . 3

A. Experimental evidence . . . 5

B. Computational evidence . . . 6

II The magnetite hypothesis . . . 9

III The candidate magnetoreceptor . . . 10

A. The sensing radical pair . . . 12

IV Spin . . . 15

A. Individual spins . . . 16

B. Multi-spin systems . . . 17

V Interactions in a radical pair . . . 18

A. Zeeman interaction . . . 19

B. Hyperfine interaction . . . 20

C. Electron-electron coupling . . . 21

D. Recombination . . . 22

E. Calculating the product yield . . . 23

VI Outline of thesis . . . 24

2 Simulating radical pair reactions **27**

I Density matrix formalism . . . 28

II Symmetric recombination . . . 29

A. Existing methods . . . 31
B. Discretising in frequency space . . . 35
III Asymmetric recombination . . . 36
A. General method . . . 37
B. Non-Hermitian Perturbation Theory . . . 38
C. Evaluating the Singlet Yield . . . 41
IV Conclusions . . . 42

3 Floquet Theory of radical pair reactions 45
I Existing methods . . . 46
II Floquet Theory in Quantum Mechanics . . . 48
A. Floquet's Theorem in matrix notation . . . 49
B. An infinite-dimensional eigenvalue problem . . . 50
C. The propagator and expectation values in Floquet space . . . 51
D. Diagonalising the Floquet Hamiltonian . . . 58
III Application to Radical Pair reactions . . . 61
A. Simplifying the infinite sum . . . 62
B. The algorithm . . . 63
C. Approximations . . . 64
IV Testing the method . . . 65
A. Monochromatic field . . . 66
B. Broadband noise . . . 70
V Phase average . . . 72
VI Conclusions . . . 73

4 A Quantum Compass Needle? 75
I An accurate compass . . . 75
II CRY-based compass needle . . . 77
A. FAD-Z radical pair . . . 77

B. FAD-Trp radical pair . . . 78
C. Larger spin systems . . . 80
III Origin of the spike in Φ_S . . . 82
A. An avoided crossing . . . 84
B. Requirements for the counter radical . . . 88
C. Relation to resonances in Floquet space . . . 90
IV Relevance to magnetoreception . . . 90
V Conclusions and further work . . . 93

5 Disrupting the avian compass 95
I Existing results . . . 97
A. Behavioural studies . . . 97
B. Computational studies . . . 100
II Results . . . 102
A. Modelling the RF conditions . . . 102
B. FAD-Z radical pair . . . 104
C. FAD-Trp radical pair . . . 108
III Relation to experiment . . . 110
A. Unrealistic parameters? . . . 111
B. Discriminating between RPs . . . 113
C. Experimental protocols . . . 115
IV Conclusions . . . 116

6 Quantum Noise in the Radical Pair Compass 119
I Origin of noise . . . 120
II Binomial distribution . . . 121
III Information Theory . . . 124
IV Deriving the lower bound heading error . . . 129
A. Shannon entropy . . . 129

B. Mutual Information 130
V Computing the lower bound heading error 131
A. The conditional entropy 133
B. Signal entropy 133
VI Magnetoreceptors in the retina 136
A. Visual Modulation Patterns 138
B. Estimate of N 138
VII Model system 141
A. Artificial data processing 143
B. Testing the compass needle 143
VIII Realistic Radical Pairs 144
A. Comparing radical pairs 144
B. Full FAD-Trp system 145
C. Focal point 148
IX Conclusions 149

7 Conclusions **153**

A Hyperfine tensors **157**
I FAD Radical 157
II Tryptophan Radical 159
III Experimentally measured components 162
IV Ascorbate Radical 163

Chapter 1

Introduction

Migratory birds are known to navigate over vast distances between their breeding and wintering sites year after year with exceptional accuracy.[36,44,80,155] They are known to use visual cues, such as the stars,[40,147,201] the sun[1,67,109,140] and landmarks along the route[139,142] to help them navigate with such reliability. It is now also well established that birds, along with a number of other animals, utilise the Earth's magnetic field in their migratory journeys.[213,214]

The 3-dimensional vector of the geomagnetic field is generally described using three quantities: the intensity of the magnetic field; the declination angle, the angle of magnetic North relative to true North; and the inclination angle, the angle the field makes with the horizontal.[136] Each of these parameters varies across the globe, meaning that there is not only directional information available, but it is possible that a "magnetic map" could also be constructed using these parameters, thereby allowing true navigation between fixed geographical points using solely magnetic cues (given a geographical reference for calibration).

Other than tracking free flying birds using radio transmitters,[28] studies testing the magnetic orientation of birds are done using Emlen funnel experiments.[41] The birds are tested in so-called Emlen funnels, which are designed to give the bird no directional cue other than an external magnetic field. If the funnels are placed within a coil system, the magnetic field can be artificially controlled.[101] During their migra-

tory season the birds will exhibit behaviour known as migratory restlessness,[63] which means that they attempt to escape from the Emlen funnel in their appropriate migratory direction. An experimental study takes the escape direction of many birds and analyses the statistical significance of any preferred orientation. Behavioural experiments of this kind have been widely used to probe different aspects of the magnetic sense, in order to offer insight into the *in vivo* sensing mechanism.

Emlen funnel experiments,[211,213] as well as tracking experiments,[28] have established the existence of an avian magnetic compass sense.[144] The prototypical evidence for this directional sense is a preferred orientation which rotates when the direction of the external magnetic field is rotated.[211] There is also a growing body of evidence that adult birds have a magnetic map sense.[106,107,144] For instance, the work described in Ref. 24 showed that experienced Eurasian Reed Warblers (*Acrocephalus scirpaceus*) were able to change their orientation to compensate for a virtual magnetic displacement. The declination of the external magnetic field was artificially altered so that the magnetic conditions mirrored those in Eastern Scotland, rather than Rybachy (Kaliningrad Oblast, Russia) where the experiments were taking place (the intensity and inclination of the field were unchanged). It was found that adult birds were able to adjust their preferred orientation direction to account for this virtual displacement, demonstrating both the expected compass orientation behaviour, but also the ability of the birds to detect their longitude using the magnetic declination angle.

Despite the extensive behavioural literature characterising the magnetic field-dependent behaviour of migratory birds, as well as a number of other animals[202] from woodmice[135] to sea turtles,[85] the biophysical mechanism underlying this magnetic sense is still unknown, and is one of the most significant unsolved problems in sensory biology. This thesis will be devoted to examining some of the experimental observations of the biological magnetic sense in the framework of one of the proposed mechanisms: the Radical Pair (RP) mechanism.

I The radical pair mechanism

The RP hypothesis of magnetoreception is currently the leading proposal for the directional magnetic sense observed in migratory birds[(1)]. The hypothesis states that the biological compass is based on a magnetic field-dependent chemical reaction.[176,177]

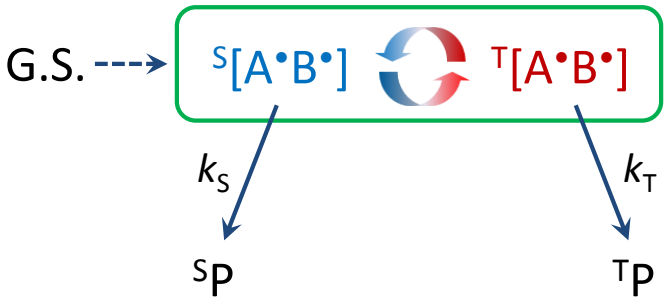


Figure 1.1: A model radical pair reaction scheme. The AB radical pair is created in the singlet state by activation of the ground state, and recombines spin selectively to distinct products with rate constants k_S and k_T respectively.

A radical pair is a reaction intermediate involving two radicals whose unpaired electrons are spin-correlated. The basic elements of a magneto-sensing RP reaction are as follows[165] (see Fig. 1.1):

1. A ground state or precursor species (G.S.) is activated, generally through photoexcitation.

2. Following electron transfer steps, this excited state forms the [A•B•] radical pair. It is presumed that the ground state is in the singlet electronic state, and that the photoexcitation and electron transfer steps are all spin-conserving, meaning that the RP is formed initially in the singlet electronic state.

3. The unpaired electron spins in the RP are coupled to the nuclear spins present in the radicals (hyperfine interactions), as well as to the external magnetic

(1) It is assumed that the magnetic map and compass senses have distinct mechanisms.

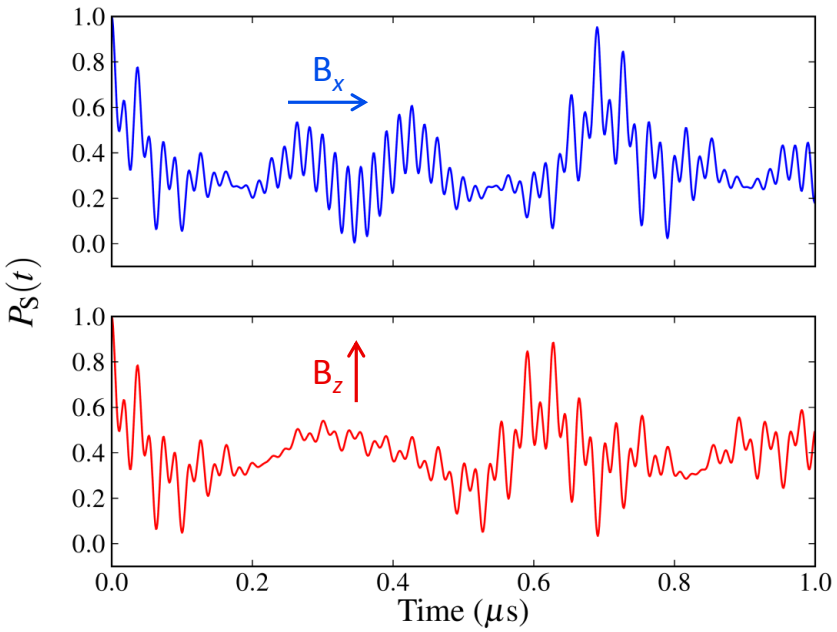


Figure 1.2: The singlet probability of the toy radical pair (see Section 3.IV) for the first 1 μs in the presence of a 50 μT external magnetic field along either the x or the z axis, but in the absence of recombination or spin relaxation.

field (Zeeman interaction). These magnetic interactions mean that the singlet initial state is a non-equilibrium/non-stationary state.

4. The RP therefore exhibits coherent oscillations between the singlet (S) and triplet (T) electronic spin states (Fig. 1.2). As the RP is in a non-equilibrium state, its dynamics can be influenced by even very weak magnetic fields, and it is the effect of an external magnetic field on this interconversion between S and T which is the basis of the field-dependence of the RP reaction.

5. If the internal interactions in the RP (namely, the electron-nucleus hyperfine couplings) are anisotropic, the effect of an external magnetic field will also be anisotropic. This is the basis of the RP model of a magnetic compass, as the S-T interconversion exhibits a dependence on the direction of an external magnetic field (Fig. 1.2).

6. Finally, there is spin-selective recombination of the RP. Because of the con-

servation of spin, the T state of the RP cannot recombine directly to a singlet ground state (and *vice versa*). In the simplest reaction scheme (Fig. 1.1), the S and T states recombine to distinct products, with rate constants k_S and k_T. The probability that the RP follows the singlet (triplet) recombination pathway is proportional to the probability the RP is in the S (T) state at a given time.

Importantly, because the coherent oscillations between S and T states in the RP intermediate are influenced by the *direction* of an external magnetic field (Fig. 1.2), this direction-dependence will be captured in the relative yields of the singlet and triplet products. It is thought that one of these species is (or is the precursor to) the signalling state in the magneto-sensing mechanism.

A. Experimental evidence

There is an increasingly significant body of evidence from behavioural, *in vitro* and computational studies in support of the RP hypothesis.[81]

Several behavioural studies have found that the biological compass is light-mediated, not only in birds[148,209,212,216] but also in newts,[162] fruit flies[161] and beetles.[198] Not only this, some studies have found a wavelength dependence of the avian compass,[148,209] thought to be indicative of a specific absorption spectrum of the RP precursor.

Another aspect of the biological compass compatible with the RP hypothesis is that it is an inclination and not a polarity compass.[207,213] Birds tested with an inverted magnetic field maintained the same preferred direction as with the reference field. It is therefore concluded that the birds are sensing the inclination but not the polarity of the magnetic field vector. Because of the symmetry of the RP interactions under the time-reversal operator, it can be shown that the fractional yield of a RP reaction is similarly invariant under inversion of the external magnetic field.[124]

An artificial RP magnetoreceptor has been designed[129] as a proof-of-principle model. A triad molecule made up of a carotenoid and a fullerene separated by a porphyrin linker was found to show a magnetic field effect (MFE) in Earth strength magnetic fields, and even a direction dependence, albeit in stronger fields (3.1 mT).[129] Additionally cryptochrome, the proposed receptor protein, has been shown to form magnetically sensitive RPs *in vitro*[128,130] (discussed below).

While the above evidence supporting the RP hypothesis is circumstantial, it is thought that behavioural studies in which the magnetic orientation of the test birds is disrupted by very weak time-dependent magnetic fields[43,167,168,179] provide direct evidence for the RP mechanism. Importantly, the observed effect is thought to rule out the competing magnetite hypothesis of the magnetic compass sense (discussed below). The observation that the exceedingly weak oscillatory fields present in these experiments can perturb magnetic orientation has been rationalised as resonance effects on the coherent oscillations of the RP.[68,170] Despite the potential importance of these experiments, there remains some controversy surrounding the interpretation of the results[97] which is discussed in detail in Chapter 5.

B. Computational evidence

This body of experimental evidence is augmented by numerous complementary computational studies, demonstrating the feasibility of realising a RP compass *in vivo*.[4,19,21,32,56,74,116,159,224] The quantum nature of the RP mechanism has lead to a great deal of interest in the suggestion that it is the basis of the biological magnetic sense and there has been a wide variety of theoretical studies exploring the various quantum effects inherent in a RP compass.

The principle that a RP reaction could exhibit sensitivity to Earth-strength magnetic fields is by now relatively well established, with many studies confirming that, under certain conditions, a variety of biologically plausible RP systems could exhibit an MFE at such weak fields.[27,165,171] The discussion has progressed further

as the size and shape of the signals available from different proposed sensing RPs have been used as evidence for or against their involvement *in vivo*. For instance, a large signal anisotropy[77] or a sharp, needle-like feature[74] have both been cited as significant evidence for different RPs being the sensing species in the mechanism (discussed in Chapter 4).

However, there is also some debate over the validity of some of these results. Firstly, as the inclusion of many nuclear spins in a fully quantum mechanical calculation becomes very difficult for large organic radicals (such as those thought to be involved in the compass sense) there are reservations about drawing conclusions from simulations of simplified spin systems. Indeed, Ref. 124 uses an approximate semiclassical method to investigate the effect of truncating the spin system in calculations of the lead candidate sensing RP (FAD-Trp, see below). The author found that the signal becomes so small when all the nuclear spins are included in the calculation that it seems ill suited to functioning as the basis of a compass (discussed in Chapter 6).

Given this potential problem with the RP hypothesis, some more recent work has suggested that the current model of the RP compass is incomplete, and some more complex variant of the RP reaction scheme is realised in the sensing mechanism. For instance, Ref. 160 has suggested that a fast looping of the photoexcitation and recombination to the ground state could act as a "signal amplifier". Another study[94] has proposed the involvement of a third radical, which could again amplify the signal available from a RP sensor by introducing a "scavenging" side reaction.

Compounding these question marks over the suitability of different RPs, there is no consensus as to what a "complete" description of the system looks like. A number of studies have included an investigation of more exotic quantum phenomena that could be important for the functioning of a RP compass. From quantum control[19] to the quantum Zeno effect[32,91] to the role of entanglement,[19,56,76] many different aspects of the mechanism have been explored. Unfortunately, the majority

of these studies have dealt with vastly simplified RP systems, and any conclusions taken from them can only be tentative, and their relevance to the functioning of an *in vivo* sensor remains debatable.

Spin relaxation

One of these quantum phenomena which is undoubtably important to take into account when studying magnetic field effects in RPs is spin relaxation. As the RP is formed in a non-equilibrium initial state, along with the coherent oscillations between S and T, the spin state will relax to the equilibrium configuration (25% singlet and 75% triplet with equal population in the three triplet states) because of the random fluctuations of the local magnetic environment due to, for instance, thermal motion of the radicals. As the spins relax to equilibrium, the correlation between them is lost and the coherent oscillations (Fig. 1.2) decay in amplitude, after which an external magnetic field can no longer influence the yield of the spin selective products, thus reducing the compass sensitivity.

Spin relaxation is of particular importance because it is estimated that both the reactive and coherence lifetimes of the RP should be at least 1 μs to observe an MFE in an Earth-strength magnetic field[81] (see below). The relaxation of the electron spins is thought to be dominated by fluctuations of the electron-nuclear hyperfine interactions caused by thermal motion of the sensing protein, and including an accurate description of the spin relaxation involves finding a representative description of the vibrational and rotational motions within the protein.

Studies accounting for these effects have generally concluded that the spin coherence lifetime can be long enough to observe an MFE for Earth-strength magnetic fields,[95,218] although the size of the signal is generally attenuated by inclusion of relaxation. However, it is possible that the situation is even more complicated than a simple decay of the coherent oscillations in the spin dynamics. For instance, Ref. 95 found that certain spin relaxation mechanisms can actually significantly enhance

the sensitivity of a RP compass.

Modelling experiments

The problem of spin relaxation becomes particularly acute when attempting to rationalise the observed disorientation of birds in the presence of exceptionally weak time-dependent magnetic fields.[167] Several studies have attempted to discuss these results[56,73,203,220] in the framework of the RP mechanism, but have largely been hampered by the computational difficulty of modelling RPs in the presence of oscillatory magnetic fields.

The consensus of these studies appears to be that for a RP to be sensitive to the exceedingly weak oscillatory fields used in the experimental studies, the spin coherence lifetime of the RP must be many orders of magnitude longer than 1 μs. Several studies have pointed out that spin coherence lifetimes of up to milliseconds are unheard of in room temperature organic RP systems,[81,97] and that seemingly implausible molecular motion would be required to realise such slow relaxation *in vivo*:[95] the magnitude and frequency of the vibrational and rotational modes of the radicals would have to be significantly different from the traditional behaviour of proteins. The interpretation of these experiments is therefore controversial and is discussed in extensive detail in Chapter 5.

II The magnetite hypothesis

For completeness, we present a brief outline of the competing hypothesis for the mechanism of magnetoreception: the magnetite hypothesis.[103,105] The basis of this hypothesis is that the biological magnetic sense is more analogous to a man-made compass needle, and is based on a crystalline form of iron oxide, magnetite (Fe_3O_4) which exhibits a more classical response to an external magnetic field.

In the simplest model, a single-domain crystal of magnetite with a diameter of around 50 nm has a permanent magnetic moment large enough to align with a

50 μT magnetic field,[103,104,188,189] thereby giving a compass bearing. Alternatively, smaller crystals with a diameter of around 20 nm, which are superparamagnetic, would have a magnetic moment induced by an Earth strength external magnetic field. If there were chains of these small particles, the induced magnetic moment would cause adjacent crystals to attract or repel,[31,104] shortening or lengthening the chain, which could be detected by mechanoreceptors or by gating ion channels, and used as the basis of an intensity or direction sensor.[87]

The primary evidence against this hypothesis is that such iron-based magnetic sensors have not be unequivocally found.[143] However, there is a growing body of evidence that the magnetic *map* sense is based on iron-containing particles.[81] It has been observed that the ophthalmic branch of the trigeminal nerve in the upper beak, which has often been linked to a magnetite-based sensor, has a relevance for magnetic tasks.[141] For instance, it was found that reed warblers could only correct for a 1,000 km displacement if this nerve remains intact,[106] although it has been found that intact trigeminal nerves are not necessary for compass orientation.[8,222] Related to this, other studies have found that strong magnetic pulses lead to changed orientation in migratory birds.[78,79] These pulses could remagnetise a magnetite sensor, suggesting that this trigeminal nerve-mediated magnetic map sense is based on a magnetite mechanism.

III The candidate magnetoreceptor

When the radical pair hypothesis of magnetoreception was first presented in 2000, the authors predicted that the then recently discovered mammalian form of the photoreceptor protein cryptochrome (CRY)[22] was ideally suited as the *in vivo* sensing protein.[165] As evidence, the authors cited the similarity of cryptochromes to photolyases, which are known to form radical pairs under light excitation as an essential part of their function.[173] Additionally, cryptochromes contain the flavin adenine dinucleotide cofactor (FAD) which is a chromophore with an absorption

spectrum (400-500 nm) that broadly agrees[165] with the action spectrum of magnetic orientation observed in Ref. 215 (400-565 nm).

This prediction has proved to be exceptionally far-sighted as cryptochrome remains the leading candidate magnetosensor protein.[81] There is a compelling body of evidence which suggests that cryptochromes are indeed involved in magnetoreception, but evidence that it is the sensing moiety is less clear cut. For instance, there have been many studies showing that magnetic field-dependent behaviours in fruit flies[49,52,57,221] and cockroaches[7] is CRY-mediated. However, these results do not necessarily mean that cryptochrome is the magnetic sensor, as it could merely be involved in the signalling pathway.

Being a light-dependent mechanism, the most obvious place to house the magnetoreceptor proteins would be in the eye,[165] particularly in the outer or inner segments of photoreceptor cells which both contain organised and aligned membrane structures.[185] These structures appear ideally suited as a scaffold on which to align cryptochromes which was part of the original model proposed in Ref. 165 thought necessary to capture an anisotropic signal. It is therefore considered important that cryptochrome proteins have been found in photoreceptor cells.[13,146,152,153] Of particular interest is the conclusion of a recent study,[62] that the expression of mammalian CRY4, which is located in double cones and long-wavelength single cones, is increased during the migratory season.

Futher evidence that the primary magnetic sensor is located in the eye of migratory birds has been provided by neuroanatomy studies. It has been found that retinal ganglion cells and an area in the forebrain called Cluster N, known to be part of the visual signalling pathway, are particularly active during magnetic orientation behaviour.[50,66,146,146,223] Additionally, when Cluster N is lesioned, European robins were unable to magnetically orient, but could still use their sun and star compasses.[222]

Despite this evidence about the signalling pathway from a neuroanatomy point

of view, one of the major problems hampering computational and *in vitro* studies is that next to nothing is known about the molecular details of the signal transduction pathway, in particular the interaction partner and the identity of the signalling state.[81] In Chapter 6, we present a novel analytical tool which allows us to circumvent the issues associated with making conclusions about a RP sensor without knowing how the reaction yields correspond to a biological signal.

A. The sensing radical pair

Given the amount of evidence for a cryptochrome-based RP magnetic sensor, it is perhaps surprising that possibly the most significant unknown is the identity of the *in vivo* RP. There are currently two different proposed cryptochrome-based sensing RPs: FAD-Trp[130] and FAD-Z,[77,186] details of which are given below. An overarching theme of this thesis will be a discussion of the computational evidence for and against these two RPs being involved in the sensing mechanism.

FAD-Trp radical pair

As mentioned above, one compelling piece of evidence for cryptochrome being the receptor protein is that cryptochromes have been shown to form magnetically sensitive RPs *in vitro*.[128,130] It is known that FAD is photoreduced in many cryptochromes and photolyases via consecutive electron transfers along the "tryptophan triad" (Fig. 1.3) – three highly conserved tryptophan (Trp) residues – to give the flavosemiquinone radical ($FAD^{\bullet -}$) and terminal tryptophan radical ($Trp_CH^{\bullet +}$).[12,20,60]

For both *Arabidopsis thaliana* CRY1 and *Escherichia coli* photolyase, it was found that [$FAD^{\bullet -}Trp_CH^{\bullet +}$] is magnetically sensitive, forms in the singlet state, and reacts according to the scheme in Fig. 1.4.[130] After photoreduction, the RP either recombines back to the (singlet) ground state or reacts via a spin independent change of protonation state of one or both radicals to form a second RP which is thought to be, or to be related to, the signalling state (Fig. 1.4).

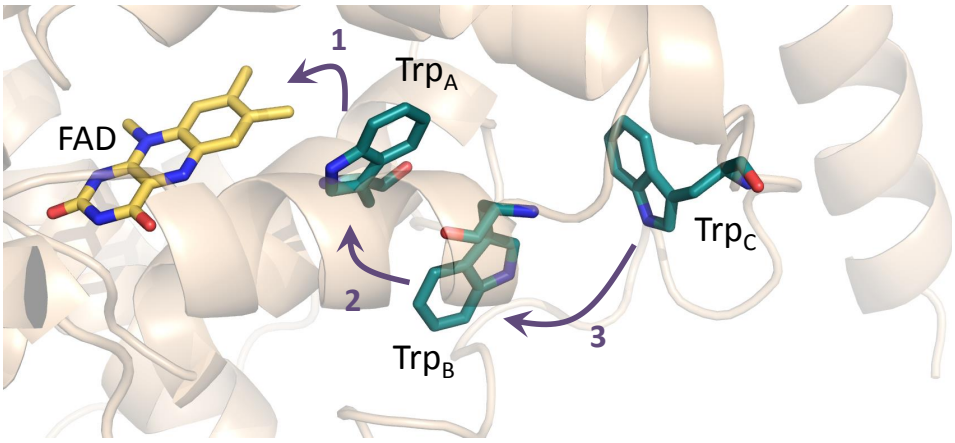


Figure 1.3: The positions of the flavin adenine dinucleotide cofactor (FAD) and tryptophan (Trp) triad in cryptochrome. The structure is that of *Arabidopsis thaliana* cryptochrome 1 (Protein Data Bank ID: 1U3C(21)). After photo-excitation of the FAD chromophore, there are three sequential electron transfers along the Trp triad to give the magnetically sensitive FAD-Trp$_C$ radical pair.[81] The FAD sidechain is truncated at the first carbon.

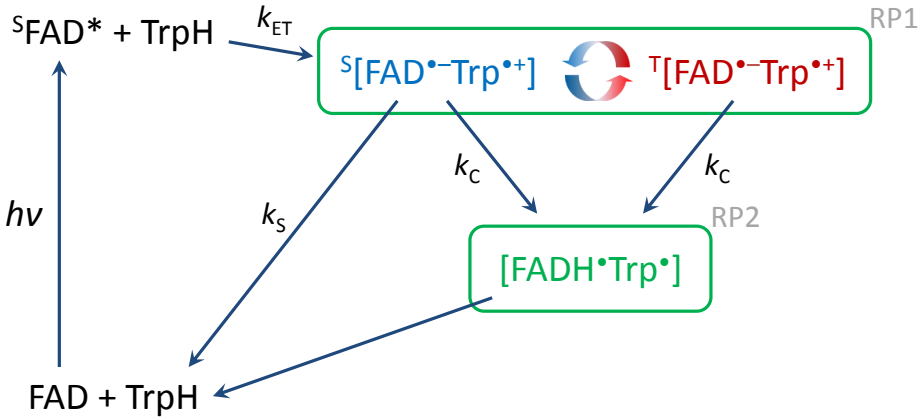


Figure 1.4: The proposed reaction scheme for the FAD-Trp radical pair sensing mechanism. After photo-excitation of the cryptochrome, electron transfer along the tryptophan triad occurs on the nanosecond time scale. This forms the magnetically sensitive radical pair 1 (RP1). This species recombines either back to the ground state with rate constant $k_S \sim 1\ \mu s^{-1}$ or, by a change of protonation state, to a second radical pair (RP2) which is not thought to exhibit magnetic-field effects, but instead is proposed as the signalling state, with rate constant $k_C \sim 1\ \mu s^{-1}$. The approximate lifetime of RP2 is ~ 10 ms.[130]

There is some suggestion that the photochemistry of the sensing CRY is different *in vivo*. For instance, it has been found that there may be other important electron transfer pathways in the protein,[42,126,156,157] in particular it was found that in *Drosophila melanogaster* cryptochrome, there is an additional tryptophan residue which may be involved in the RP.[149]

FAD-Z radical pair

The other proposed sensing RP assumes that the photochemistry *in vivo* is indeed different from these studies of purified proteins. The proposed reaction scheme is outlined in Fig. 1.5. The first step is the same photoreduction as above, followed by a second photoreduction of the flavin to the fully reduced flavin anion. The combined absorption spectrum of this reaction scheme better agrees with the observed operational window of magnetic orientation.[148,209,215] Following this, it is hypothesised that on reoxidation of the flavin by an as yet unknown electron acceptor (Z in Fig. 1.5) the magnetic field-dependent RP [$FADH^{\bullet}Z^{\bullet}$] is formed.

One of the features of this proposed mechanism is that the magnetically sensitive step in the reaction scheme occurs in the dark. Supporting this idea, a recent study[208] found that birds were able to orient despite the magnetic field and light not being present together in the experiment. The conditions were periodic over 1 second intervals, the birds exposed to light for the first 300 ms in the absence of a magnetic field, which is then introduced in the dark in the following 700 ms.[208] However, it has been suggested[93] that the time interval in the experiments is slightly contrived and is perhaps unsuitable for the proposed reaction scheme.

Further experimental evidence cited as being proof of this reaction scheme is the disorientation of birds by weak time-dependent magnetic fields.[167] In particular, it has been observed that an oscillatory field at the Larmor frequency (see below) has a disorienting effect at particularly low field strengths. This has been interpreted to mean that one of the radicals in the RP contains no hyperfine-coupled nuclei

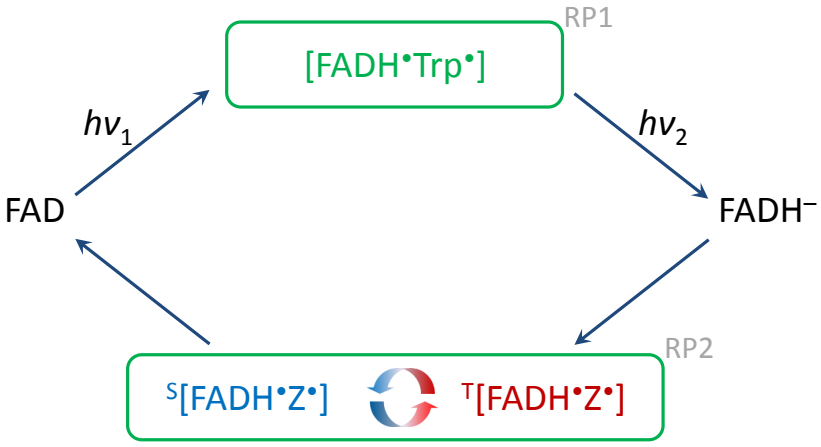


Figure 1.5: The proposed reaction scheme for the FAD-Z radical pair sensing mechanism. The first step is photo-activated reduction of the flavin cofactor to form radical pair 1 (RP1), similar to the first steps in the FAD-Trp reaction scheme. ν_1 is in the UV-A to blue range, up to 500 nm. In this model, RP1 is not thought to be magnetically sensitive. The second step is further photo-reduction (ν_2 is in the UV to 570 nm wavelength range) of the $FADH^{\bullet}$ to the fully reduced form, $FADH^{-}$. This fully reduced form can then be reoxidised without further absorption of light via a second radical pair (RP2). The counter radical ($Z^{\bullet}$) is currently unknown, and RP2 is thought to be the magnetically sensitive radical pair.[208]

(discussed in Chapter 5). It has been suggested[208] that this is the $Z^{\bullet}$ radical, which is as yet unknown but could be a superoxide radical, $O_2^{\bullet -}$. The details of the spin dependent recombination pathways and signalling state remain entirely unknown for this hypothesised RP.

However, there is a considerable amount of controversy surrounding this interpretation of the experimental results.[97] In addition, it has been suggested that a superoxide radical would undergo exceedingly fast spin relaxation,[77,89,90] making it unsuitable as a sensing RP.

IV Spin

Having established the hypothesised framework of the RP mechanism, we now present an outline of how RP systems can be modelled, starting with the description of spin. A fundamental property of electrons and nuclei, spin is an intrinsic angular

momentum which is revealed on solving the relativistic Schrödinger equation[33,34] and endows an intrinsic magnetic moment to the electron/nucleus. The general interest in the RP mechanism is in no small part due to the idea that spin, a purely quantum mechanical property with no classical analogue, could be an integral part in a biological sensing mechanism.

A. Individual spins

Spin is described by two quantum numbers: the spin quantum number S and the spin projection quantum number m_S. By convention, when referring to nuclear spins, these quantum numbers are often denoted I and m_I respectively. S can take integer or half-integer values, and is a fundamental property of electrons, for which $S = 1/2$, and nuclei, for which I can take many different values. In organic radicals, the most common nuclei with non-zero spin are hydrogen-1 ($I = 1/2$) and nitrogen-14 ($I = 1$). m_S can take values from $-S$ to S in integer steps, meaning that there are $2S + 1$ different states for a given spin.[3]

These quantum numbers are related to the eigenvalues of different eigenstates under the square magnitude spin angular momentum operator ($\hat{S}^2$) and the operator for the z-projection of the spin ($\hat{S}_z$)[(2)]:

$$\begin{aligned} \hat{S}^2|S, m_S\rangle &= S(S+1)|S, m_S\rangle, \\ \hat{S}_z|S, m_S\rangle &= m_S|S, m_S\rangle. \end{aligned} \tag{1.1}$$

For electrons, $S = 1/2$ meaning m_S can take values $\pm 1/2$, which are commonly referred to as the "spin up" and "spin down" states, and are usually written in the following compact notation

$$|1/2, +1/2\rangle = |\alpha\rangle, \quad |1/2, -1/2\rangle = |\beta\rangle. \tag{1.2}$$

[(2)]Here and throughout this thesis we use angular frequency units for which $\hbar = 1$ to simplify expressions.

In the methods presented in the following chapters, we use a Hilbert space matrix formalism to perform calculations of RP reactions. As there are $2S + 1$ states for a given spin, the dimension of the matrices representing the quantum mechanical operators is $2S + 1$. In the above basis set, the Cartesian spin operators for an electron are related to the Pauli matrices,[111] $\hat{S}_\alpha = \frac{1}{2}\sigma_\alpha$

$$\sigma_x = \begin{pmatrix} 0 & 1 \\ 1 & 0 \end{pmatrix},$$
$$\sigma_y = \begin{pmatrix} 0 & -\mathrm{i} \\ \mathrm{i} & 0 \end{pmatrix}, \tag{1.3}$$
$$\sigma_z = \begin{pmatrix} 1 & 0 \\ 0 & -1 \end{pmatrix}.$$

Similar matrices can be constructed for any spin with any S (or I).

B. Multi-spin systems

The task of modelling RP reactions essentially involves modelling a number of coupled (electron and nuclear) spins. The interactions which couple these different spins are outlined below.

One of the important results of including many coupled spins in our description is that, in order to include all possible combinations of spin states for each individual spin, the dimension (Z_{tot}) of the combined Hilbert space (the tensor product space), and therefore the matrix operators used in the calculation, is the product of the number of states of each spin

$$Z_{\mathrm{tot}} = \prod_{\text{electrons}} (2S_i + 1) \times \prod_{\text{nuclei}} (2I_j + 1). \tag{1.4}$$

One of the major challenges in performing spin dynamics calculations on RPs is that the size of the matrices needed to describe the system becomes unmanageable if we

want to be able to model realistic, multi-nuclear organic radicals.[132] Much effort has been dedicated to trying to accurately describe RP systems by circumventing this problematic scaling, using for example semi-classical approaches.[125,132,177]

In the context of RPs, when we couple the electron spins, we are specifically interested in whether the electrons are in the singlet

$$|\mathrm{S}\rangle = |0,0\rangle = \frac{1}{\sqrt{2}}\Big(|\alpha\rangle_1 \otimes |\beta\rangle_2 - |\beta\rangle_1 \otimes |\alpha\rangle_2\Big), \tag{1.5}$$

or the triplet state

$$\begin{aligned} |\mathrm{T}_+\rangle &= |1,1\rangle = |\alpha\rangle_1 \otimes |\alpha\rangle_2, \\ |\mathrm{T}_0\rangle &= |1,0\rangle = \frac{1}{\sqrt{2}}\Big(|\alpha\rangle_1 \otimes |\beta\rangle_2 + |\beta\rangle_1 \otimes |\alpha\rangle_2\Big), \\ |\mathrm{T}_-\rangle &= |1,-1\rangle = |\beta\rangle_1 \otimes |\beta\rangle_2. \end{aligned} \tag{1.6}$$

When the electron spins are paired in the product states of the RP, the exchange interaction (see below) dominates. As the singlet and triplet states are eigenstates of the exchange operator, and the recombination step is spin-conserving, this is the pertinent basis for determining the fractional yields of a RP.

V Interactions in a radical pair

Now that we have outlined the matrices describing the spin operators for individual electrons and nuclei, we move on to the Hamiltonians describing the various interaction terms present in a RP. The total spin Hamiltonian, which governs the time dependence of the spin dynamics of the RP, is the sum of four different terms[138,190]

$$\hat{H}_{\mathrm{tot}} = \hat{H}_1 + \hat{H}_2 + \hat{H}_J + \hat{H}_D. \tag{1.7}$$

$\hat{H}_i$ is the individual spin Hamiltonian describing the internal interactions in radical i, which contains two terms: the Zeeman and hyperfine interactions. $\hat{H}_J$ and $\hat{H}_D$

arise from electron-electron coupling terms. We shall consider each operator in turn.

A. Zeeman interaction

In the presence of an external magnetic field, there is an interaction between the intrinsic magnetic dipole associated with the electron spin[(3)] and the external field, called the Zeeman interaction,[58]

$$\hat{H}_{\mathrm{Ze}} = \boldsymbol{\omega} \cdot \hat{\mathbf{S}} = -\gamma_{\mathrm{e}} \mathbf{B} \cdot \hat{\mathbf{S}}, \tag{1.8}$$

where $\boldsymbol{\omega} = -\gamma_{\mathrm{e}}\mathbf{B}$ is used by convention with $\gamma_{\mathrm{e}} = -g_{\mathrm{e}}\mu_{\mathrm{B}}$ (again with units where $\hbar = 1$) is the gyromagnetic ratio of an electron which is related to the Bohr magneton (μ_{B}) and the electron spin g-factor (g_{e}). $\hat{\mathbf{S}}$ is the vector of Cartesian electron spin operators $\{\hat{S}_x, \hat{S}_y, \hat{S}_z\}$. This equation presumes an isotropic g-factor equal to that of a free electron, as we are dealing with organic radicals in which the spin orbit coupling is thought to be small.[171]

In the absence of any other interaction terms, this system can be solved exactly. Without loss of generality, we choose the external field to lie in the z direction, which causes the $|\alpha\rangle$ and $|\beta\rangle$ states to split in energy and have new energies $-\gamma_{\mathrm{e}} m_S |\mathbf{B}|$. The energy gap between these states defines the so-called Larmor frequency (in Hz)[168]

$$\nu_{\mathrm{L}} = \frac{\gamma_{\mathrm{e}}|\mathbf{B}|}{2\pi}. \tag{1.9}$$

This frequency is often used as a rough guide of the time scale over which the external magnetic field will have a significant effect on the spin dynamics of the electron.[81] This is the basis of our statement above, that we would require a RP lifetime of around 1 μs for a 50 μT magnetic field to cause a significant change in the relative product yield, as $1/\nu_{\mathrm{L}} = 2\pi/\gamma_{\mathrm{e}}|\mathbf{B}| \simeq 700$ ns.

[(3)] There is an analogous interaction between the nuclear spins with the external field, though since the gyromagnetic ratios of H and N are far smaller than γ_{e}, we neglect these interaction terms.

There have been several studies which have found that a magnetic field oscillating at the Larmor frequency has a particularly strong disorienting effect on birds' response to magnetic cues.[168] If a radical only experiences the external magnetic field, an oscillatory field at this frequency would have a particularly significant effect on the spin dynamics as it would drive transitions between the $|\alpha\rangle$ and $|\beta\rangle$ states in the radical. This is the basis of the interpretation of these results as meaning that one of the radicals in the sensing RP is devoid of any hyperfine interactions.

B. Hyperfine interaction

The other term in the individual radical Hamiltonians describes the interaction between the unpaired electron spin with the surrounding nuclear spins, and is called the hyperfine interaction. There are two contributions to this coupling which depend on the molecular orbital describing the electron's spatial state in the RP^3 which is generally calculated using a density function theory (DFT) method.[116]

First, there is a term arising from the direct dipolar interaction between the magnetic moment of the spin of the unpaired electron and that of the nucleus. This term is in general anisotropic. The other term is known as the Fermi contact interaction and describes the magnetic interaction when the unpaired electron is within the nucleus.[137] This term is isotropic.

Combining these terms, the hyperfine interaction between the unpaired electron in radical i with nucleus k in that radical is given by[58]

$$\hat{H}_{\mathrm{hf}} = \hat{\mathbf{S}}_i \cdot \mathrm{A}_{ik} \cdot \hat{\mathbf{I}}_{ik}. \tag{1.10}$$

The strength and direction-dependence of the hyperfine interaction has been captured in the hyperfine tensor, A_{ik}. $\hat{\mathbf{I}}_{ik}$ is the spin operator for nucleus k in radical i.

The total hyperfine interaction is simply the sum of these individual hyperfine terms over all the nuclei with $I > 0$, meaning the Hamiltonian describing an indi-

vidual radical with N_i nuclei with non-zero spin is

$$\hat{H}_i = -\gamma_e \mathbf{B} \cdot \hat{\mathbf{S}} + \sum_{k=1}^{N_i} \hat{\mathbf{S}}_i \cdot \mathrm{A}_{ik} \cdot \hat{\mathbf{I}}_{ik}. \tag{1.11}$$

C. Electron-electron coupling

The final terms to consider in our description of the RP are interactions between the unpaired electrons on the two radicals. There are two distinct sources of inter-radical coupling: the overlap of the spatial wavefunctions of the two electrons, and the interaction of each electron spin with the magnetic field arising from the other unpaired electron.[169]

The exchange coupling deals with the first of these, and is particularly important for short radical-radical distances. The Hamiltonian term including the exchange interaction is[84]

$$\hat{H}_J = -J\hat{\mathbf{S}}_1 \cdot \hat{\mathbf{S}}_2. \tag{1.12}$$

It is generally assumed that the size of the exchange constant J decreases exponentially with increasing RP separation (r), and is independent of the relative orientation of the radicals, and so can be written as:[138]

$$J(r) \approx J_0 e^{-r/r_J}, \tag{1.13}$$

where J_0 and r_J are empirical parameters.

The interaction between the magnetic fields from each electron is captured by the dipolar interaction, with Hamiltonian given by[45]

$$\hat{H}_D = \hat{\mathbf{S}}_1 \cdot \mathrm{D} \cdot \mathbf{S}_2, \tag{1.14}$$

where D is the dipolar interaction tensor. D is often parameterised by the relative orientation of the two radicals in terms of angle ϕ

$$\mathrm{D}_\phi = \begin{pmatrix} 2\sin^2(\phi) - \frac{2}{3} & 0 & \sin(2\phi) \\ 0 & -\frac{2}{3} & 0 \\ \sin(2\phi) & 0 & 2\sin^2(\phi) - \frac{2}{3} \end{pmatrix} \tag{1.15}$$

and radical-radical distance, r (assuming point dipoles)

$$\mathrm{D}_r = -\frac{3}{2}\frac{\mu_0}{4\pi}\frac{\gamma_\mathrm{e}^2}{r^3}. \tag{1.16}$$

As $\mathrm{D} = \mathrm{D}_\phi \times \mathrm{D}_r$ scales with r^{-3}, as opposed to $J(r)$ which decays exponentially, the dipolar coupling becomes dominant for large r.

D. Recombination

We now have a complete description of the energetic interactions thought to be important in a RP. The final remaining piece of the description we require is a way to model the reactive coupling of the radicals. In order to do this, we use the Haberkorn recombination operator.[64]

While the spin Hamiltonian $\hat{H}_\mathrm{tot}$ governs the unitary, coherent dynamics of the RP, the non-unitary, incoherent recombination is generally described by a recombination operator $\hat{K}$.[64] The general idea is to assess the probability of the RP being in the singlet and triplet states, and therefore the probability of forming the singlet and triplet products, over the lifetime of the RP. To compute these probabilities we use the singlet and triplet projection operators[3]

$$\begin{aligned} \hat{P}_\mathrm{S} &= \frac{1}{4} - \hat{\mathbf{S}}_1 \cdot \hat{\mathbf{S}}_2, \\ \hat{P}_\mathrm{T} &= \frac{3}{4} + \hat{\mathbf{S}}_1 \cdot \hat{\mathbf{S}}_2. \end{aligned} \tag{1.17}$$

In order to simplify our calculations, and as the recombination scheme of the FAD-Z radical pair is unknown, we use the simplified reaction scheme (Fig. 1.1). The conventional approach, which we will be using within this thesis, is to use the phenomenological Haberkorn recombination operator[64]

$$\hat{K} = \frac{k_{\mathrm{S}}}{2}\hat{P}_{\mathrm{S}} + \frac{k_{\mathrm{T}}}{2}\hat{P}_{\mathrm{T}} \tag{1.18}$$

which is inserted into the differential equation governing the time evolution of the RP spin dynamics (Eq. 2.3).

There is some debate as to whether using this form of the operator is valid, and alternative approaches have been suggested, including the Jones-Hore master equation based on a quantum measurement approach.[88] Indeed, recent work has formulated a description of a general spin selective electron transfer reaction in a RP based on non-adiabatic rate theory.[48]

E. Calculating the product yield

With a complete description of the Hamiltonian governing the coherent oscillations in the RP spin dynamics (Eq. 1.7) as well as defining an operator to capture the reaction kinetics (Eq. 1.18), we now consider how we can use these to compute the fractional yield of the singlet and triplet products. By convention, we calculate the fractional singlet yield, denoted Φ_{S}, the triplet yield simply being $\Phi_{\mathrm{T}} = 1 - \Phi_{\mathrm{S}}$.

Using the Hamiltonian and Haberkorn recombination operator defined above, we can model how the spin system evolves over time (see Section 2.I). At any given instant, the probability that the RP will recombine to the singlet (triplet) product is proportional to the probability that the RP is in the electronic singlet (triplet) spin state, $P_{\mathrm{S}}(t)$ ($P_{\mathrm{T}}(t)$). The proportionality constant is given by the rate constant of the singlet (triplet) recombination pathway, as this captures the relative likelihood of following one pathway over the other. To compute the average fractional yield, this probability of forming the singlet (triplet) state must be integrated over time

to capture the coherent oscillations in $P_{\mathrm{S}}(t)$ (Fig. 1.2)

$$\Phi_{\mathrm{S}} = k_{\mathrm{S}} \int_0^\infty P_{\mathrm{S}}(t)\mathrm{d}t. \tag{1.19}$$

VI Outline of thesis

The remainder of this thesis will be presented as follows. In Chapter 2 we outline the standard computational methods for calculating the product yields of RP reactions, distinguishing between symmetric ($k_{\mathrm{S}} = k_{\mathrm{T}}$ in Fig. 1.1) and asymmetric recombination ($k_{\mathrm{S}} \neq k_{\mathrm{T}}$). We also present a novel algorithm for each case, involving a discretisation in frequency space and non-Hermitian perturbation theory respectively.

Chapter 3 contains a derivation of a novel method for simulating RP reactions in the presence of a time-dependent external magnetic field, based on Floquet theory.[183] This method is able to include both single-frequency and band-limited noise oscillatory magnetic fields and is applicable for large, multinuclear RPs. The derivation forms the basis of Ref. 72.

In the following chapter, we discuss the applicability of the two hypothesised sensing RPs – FAD-Z and FAD-Trp – to a biological magnetic compass, in particular outlining conditions in which the FAD-Trp RP could give rise to very high directional precision as first presented in Ref. 74, and discussing its potential relevance to magnetoreception.

In Chapter 5, we discuss the various conflicting observations from behavioural studies which found that extremely weak time-dependent magnetic fields could disrupt magnetic orientation of birds in the context of the RP mechanism. We use our novel Floquet-based algorithm to simulate RPs including a realistic number of nuclear spins in the presence of single-frequency and broadband-noise external magnetic fields. Specifically, we examine the compatability of the experimental observations with the hypothesised FAD-Z and FAD-Trp radical pair sensors. This

work formed the basis of Ref. 73.

In Chapter 6 we investigate the effect of low light levels on the functioning of a (light-dependent) RP compass. We derive a description for the probability distribution of the fractional singlet yield averaged over a finite number of reaction cycles, and use a novel information theory-based[180] analytical tool to model the effect this uncertainty in the singlet yield signal has on the functioning of a RP compass. Importantly, we are able to successfully bypass our ignorance about the signal transduction pathway *in vivo*, and compute a best case compass accuracy. This work will be presented in Ref. 71.

Finally, in Chapter 7 we discuss the conclusions taken from our work and suggest avenues of future research and extensions of the work presented in this thesis.

Chapter 2

Simulating radical pair reactions

The radical pair hypothesis of magnetoreception relies on the yield of a radical pair reaction being sensitive to the direction of an external magnetic field, which *in vivo* is the geomagnetic field.[177] In order to examine various aspects of the mechanism, we need to model the spin evolution of the radical pair. This involves the coherent oscillations between singlet and triplet states due to the interactions described by the spin Hamiltonian outlined in Eq. 1.7,[178] and the incoherent reaction to one of the product states described by the recombination operator in Eq. 1.18.[64]

This chapter will describe a number of algorithms used to calculate the average fractional yield of singlet product of a radical pair in the presence of a static Zeeman field, based on the simple general reaction scheme in Fig. 1.1.[197] Much of the effort in these spin dynamics calculations is dedicated to maximising the total number of spins (electrons plus nuclei) that we can include, in order to model the multinuclear organic radicals proposed as being involved in magnetoreception. The challenge this presents is that, as described in the previous chapter, the size of the Hilbert space scales exponentially with the number of spins,[132] meaning the computational effort of the necessary matrix operations quickly limits our investigations.

We present some novel algorithms that vastly improve the computational efficiency of these calculations. First, existing methods are outlined,[27] from which simple approximations can greatly reduce the number of operations required to per-

form the calculations.

I Density matrix formalism

In order to model radical pair reactions, we use the time evolution of a density matrix. This approach is used when it is necessary to describe a statistical ensemble of states, rather than a single, well-defined quantum state.[47] The radical pair initial state is assumed to be the singlet electronic spin state (Chapter 1), but the spin state of the nuclei is unknown. Therefore, we use a density matrix to describe the behaviour of a pure singlet electronic spin state and the fully mixed state of the nuclear spins, which is the ensemble of all possible nuclear spin state configurations. This corresponds to the following density matrix[132]

$$\hat{\rho}(0) = \left(\hat{P}_{\mathrm{S}}\right)_e \otimes \frac{1}{Z}\mathbb{I}_Z, \tag{2.1}$$

where $\left(\hat{P}_{\mathrm{S}}\right)_e$ is the singlet projection operator in the electronic subspace (Eq. 1.17), $\mathbb{I}_Z$ is the identity operator in the nuclear spin subspace and $1/Z$ is a normalisation over the number of nuclear spin states (or nuclear spin multiplicity, see Section 1.IV):

$$Z = \prod_i (2I_i + 1)\,. \tag{2.2}$$

I_i is the spin angular momentum quantum number of nucleus i. The dimension of the the combined nuclear and electronic subspaces is $4Z$.

We now need to find the density operator at time t given this initial state and the total Hamiltonian $\hat{H}$ (Eq. 1.7) and recombination operator $\hat{K}$ (Eq. 1.18. The time dependence of the density matrix is given by the Liouville-von Neumann equation[16]

$$\frac{\mathrm{d}}{\mathrm{d}t}\hat{\rho}(t) = -\mathrm{i}\left[\hat{H}, \hat{\rho}(t)\right] - \left\{\hat{K}, \hat{\rho}(t)\right\}, \tag{2.3}$$

where $\left[\hat{A}, \hat{B}\right]$ is the commutator and $\left\{\hat{A}, \hat{B}\right\}$ is the anticommutator of operators $\hat{A}$ and $\hat{B}$. With a time-independent Hamiltonian, the solution of this equation gives the density matrix at time t which, with the initial condition $\hat{\rho}(0)$, is[65]

$$\hat{\rho}(t) = U(t;0)\hat{\rho}(0)U(t;0)^{\dagger} = \exp\left(-\mathrm{i}\hat{H}t - \hat{K}t\right)\hat{\rho}(0)\exp\left(+\mathrm{i}\hat{H}t - \hat{K}t\right), \qquad (2.4)$$

where $U(t;0)$ represents the time evolution operator for the time interval $0 \rightarrow t$.

According to Eq. 1.19, we need to find the singlet probability of the RP over time in order to compute the singlet product yield.[178] Using a density matrix, the expectation value of an operator $\hat{A}$ is found using a trace[65]

$$A(t) = \mathrm{tr}\left[\hat{\rho}(t)\hat{A}\right], \qquad (2.5)$$

where the trace runs over all $4Z$ states of the Hilbert space.

II Symmetric recombination

One important simplification that is commonly used is to set the rate constants for the singlet and triplet recombination pathways to be equal i.e. $k_{\mathrm{S}} = k_{\mathrm{T}} = k$ in Fig. 1.1.[197] It is usually reasoned[94] that a very large difference between the rate constants would remove any anisotropy in the product yield and would therefore be unsuitable for a RP compass. If one recombination pathway dominates, effectively 100% of RPs would form the corresponding product, regardless of the direction of a weak external field. Additionally, it is assumed that discarding small differences between the rate constants does not qualitatively change the results of the calculations,[171] and the computational simplification afforded by this approximation is more important than the resulting inaccuracies in the calculations (see Chapter 4 for tests of this assumption).

The important result of setting $k_{\mathrm{S}} = k_{\mathrm{T}}$ is that $\hat{K}$ becomes proportional to the

identity operator[125]

$$\hat{K} = \frac{k}{2}\hat{P}_{\mathrm{S}} + \frac{k}{2}\hat{P}_{\mathrm{T}} = \frac{k}{2}\mathbb{I} \tag{2.6}$$

as the sum of the singlet and triplet projection operators is the sum over a complete set of projection operators. Importantly, the identity operator commutes with any operator, and therefore the recombination terms can be separated from the interaction terms in Eq. 2.4

$$\hat{\rho}(t) = \frac{1}{Z}\exp\left(-\mathrm{i}\hat{H}t\right)\hat{P}_{\mathrm{S}}\exp\left(+\mathrm{i}\hat{H}t\right)e^{-k\mathbb{I}t}, \tag{2.7}$$

where the form of $\hat{\rho}(0)$ from Eq. 2.1 has been inserted. Then, because the identity operator is diagonal, the exponential can be written $e^{-k\mathbb{I}t} = \mathbb{I}e^{-kt}$. Putting this into the trace to find the singlet probability

$$P_{\mathrm{S}}(t) = \frac{1}{Z}e^{-kt}\mathrm{tr}\left[\exp\left(-\mathrm{i}\hat{H}t\right)\hat{P}_{\mathrm{S}}\exp\left(+\mathrm{i}\hat{H}t\right)\hat{P}_{\mathrm{S}}\right] \tag{2.8}$$

we find that the singlet yield is given by[197]

$$\Phi_{\mathrm{S}} = \frac{k}{Z}\int_0^\infty \mathrm{tr}\left[\exp\left(-\mathrm{i}\hat{H}t\right)\hat{P}_{\mathrm{S}}\exp\left(+\mathrm{i}\hat{H}t\right)\hat{P}_{\mathrm{S}}\right]e^{-kt}\mathrm{d}t. \tag{2.9}$$

The form of the integral makes it apparent that symmetric recombination results in a simple exponential decay of the RP population, and decouples the coherent and recombination terms in the spin state evolution. Therefore, we opt to model the coherent evolution in the absence of recombination, and simply insert the appropriate decaying exponential in the singlet yield expression[17]

$$\Phi_{\mathrm{S}} = k\int_0^\infty P_{\mathrm{S}}(t)e^{-kt}\mathrm{d}t. \tag{2.10}$$

$P_{\mathrm{S}}(t)$ in this expression is the singlet probability of the RP including just the interaction terms i.e. Eq. 2.8 without the e^{-kt} term (the same notation is used by

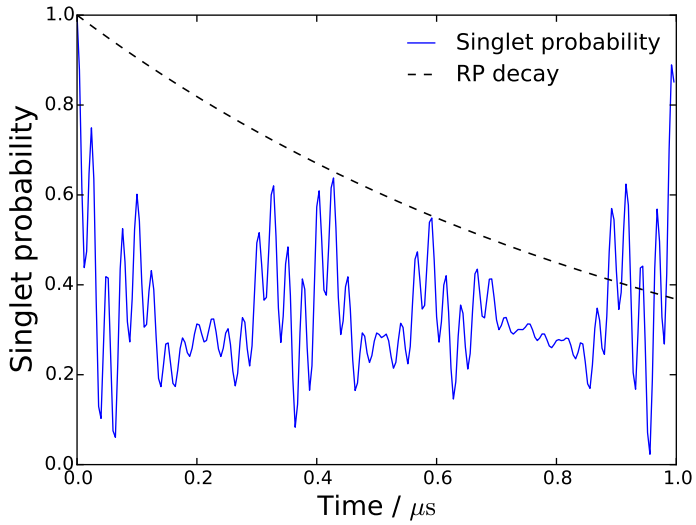


Figure 2.1: The average coherent and reaction dynamics in the first microsecond of a simple RP with $k = 10^6$ s^{-1}. The details of the RP are given in Section 3.3.4.

convention). An example of the time-dependence of these two dynamic processes is given in Fig. 2.1.

A. Existing methods

The most general method to calculate the singlet probability over time is to propagate the system[61] (described in Chapter 3) and evaluate the integral in Eq. 2.10 numerically. However, in this instance, it is easier to find a closed form expression for Φ_S.

The procedure involves inserting resolutions of the identity in terms of eigenstates of the Hamiltonian $\mathbb{I} = \sum_{n=1}^{4Z} |n\rangle\langle n|$

$$\begin{aligned} P_S(t) &= \frac{1}{Z}\mathrm{tr}\left[\exp\left(-\mathrm{i}\hat{H}t\right)\left(\sum_{n=1}^{4Z}|n\rangle\langle n|\right)\hat{P}_S\exp\left(+\mathrm{i}\hat{H}t\right)\left(\sum_{m=1}^{4Z}|m\rangle\langle m|\right)\hat{P}_S\right] \\ &= \frac{1}{Z}\mathrm{tr}\left[\sum_{n,m=1}^{4Z}\exp\left(-\mathrm{i}E_n t\right)|n\rangle\langle n|\hat{P}_S\exp\left(+\mathrm{i}E_m t\right)|m\rangle\langle m|\hat{P}_S\right] \\ &= \frac{1}{Z}\sum_{n,m=1}^{4Z}\exp\left(-\mathrm{i}(E_n - E_m)t\right)\left|\left(\hat{P}_S\right)_{nm}\right|^2 \end{aligned} \tag{2.11}$$

where E_α is the energy of state α and $\left(\hat{P}_\mathrm{S}\right)_{nm} = \langle n|\hat{P}_\mathrm{S}|m\rangle$. We have used the cyclic invariance of the trace and the Hermiticity of $\hat{P}_\mathrm{S}$ in going from the second to the third line.

Inserting into our expression for the singlet yield (Eq. 2.10)[197]

$$\begin{aligned}
\Phi_\mathrm{S} &= k\int_0^\infty P_\mathrm{S}(t)e^{-kt}\mathrm{d}t \\
&= \frac{k}{Z}\sum_{n,m=1}^{4Z}\left|\left(\hat{P}_\mathrm{S}\right)_{nm}\right|^2\int_0^\infty \exp\left(-\mathrm{i}\omega_{nm}t - kt\right)\mathrm{d}t \\
&= \frac{k}{Z}\sum_{n,m=1}^{4Z}\left|\left(\hat{P}_\mathrm{S}\right)_{nm}\right|^2\frac{1}{k+\mathrm{i}\omega_{nm}} \\
&= \frac{1}{Z}\sum_{n,m=1}^{4Z}\left|\left(\hat{P}_\mathrm{S}\right)_{nm}\right|^2\frac{k^2}{k^2+\omega_{nm}^2},
\end{aligned} \tag{2.12}$$

where $\omega_{nm} = E_n - E_m$ and the final step relies on the antisymmetry of the energy differences, i.e. $\omega_{nm} = -\omega_{mn}$ means the imaginary $\{n, m\}$ term cancels with the imaginary $\{m, n\}$ term. This ensures the singlet yield is a real quantity, as required for a physical observable.

We therefore have a closed form expression for the singlet yield in terms of the singlet projection operator, recombination rate and eigenstates and eigenvalues of the Hamiltonian. The bottleneck for this algorithm is the diagonalisation of the Hamiltonian matrix, which is $\mathcal{O}(Z^3)$ operations.[163] For the general case, this scaling is no better than the method for asymmetric recombination (see below), though algorithms for diagonalising a Hermitian matrix are more efficient than for a general matrix.

However, symmetric recombination affords a significant improvement if there are no radical-radical interaction terms in the RP Hamiltonian. If the exchange and dipolar interactions are set to zero, there are no terms which couple the two radicals, and therefore the RP Hamiltonian can be separated into a direct sum of

Hamiltonians describing the interactions in each radical separately ($\hat{H}_i$)[178]

$$\hat{H} = \hat{H}_1 \oplus \hat{H}_2. \tag{2.13}$$

The non-interacting subspaces are also not coupled by the recombination operator as $\hat{K}$ is also separable: $\hat{K} = k\mathbb{I} = k(\mathbb{I}_1 \otimes \mathbb{I}_2)$.

If we write $\hat{P}_\mathrm{S}$ in terms of Cartesian spin operators (Eq. 1.17), and separate the operator exponentials (as they commute), we can find an alternative form for the singlet probability[178]

$$\begin{aligned} P_\mathrm{S}(t) &= \frac{1}{Z}\mathrm{tr}\left[\exp\left(-\mathrm{i}\hat{H}t\right)\hat{P}_\mathrm{S}\exp\left(+\mathrm{i}\hat{H}t\right)\hat{P}_\mathrm{S}\right] \\ &= \frac{1}{Z}\mathrm{tr}\left[e^{-\mathrm{i}\hat{H}_1 t}e^{-\mathrm{i}\hat{H}_2 t}\left(\frac{1}{4}\mathbb{I} - \hat{\mathbf{S}}_1\cdot\hat{\mathbf{S}}_2\right)e^{+\mathrm{i}\hat{H}_1 t}e^{+\mathrm{i}\hat{H}_2 t}\left(\frac{1}{4}\mathbb{I} - \hat{\mathbf{S}}_1\cdot\hat{\mathbf{S}}_2\right)\right] \\ &= \frac{1}{4} + \sum_{\alpha,\beta=x,y,z}\mathrm{tr}\left[e^{-\mathrm{i}\hat{H}_1 t}\ \hat{S}_{1\alpha}\ e^{+\mathrm{i}\hat{H}_1 t}\hat{S}_{1\beta}\ e^{-\mathrm{i}\hat{H}_2 t}\ \hat{S}_{2\alpha}\ e^{+\mathrm{i}\hat{H}_2 t}\hat{S}_{2\beta}\right] \\ &= \frac{1}{4} + \sum_{\alpha,\beta=x,y,z} R^{(1)}_{\alpha\beta}(t)R^{(2)}_{\alpha\beta}(t). \end{aligned} \tag{2.14}$$

We have rewritten the singlet probability in terms of the 9 spin correlation tensors

$$R^{(i)}_{\alpha\beta}(t) = \frac{1}{Z_i}\mathrm{tr}_i\left[e^{-\mathrm{i}\hat{H}_i t}\ \hat{S}_{i\alpha}\ e^{+\mathrm{i}\hat{H}_i t}\hat{S}_{i\beta}\right], \tag{2.15}$$

where the trace is to be taken over the subspace of radical i, $\hat{S}_{ix}$ is the Cartesian x spin operator for radical i, and Z_i is the relevant nuclear spin multiplicity ($Z = Z_1 \times Z_2$).

Now we can diagonalise each Hamiltonian individually to obtain separate eigendecompositions for the two radicals ($E_{n_i}, |n_i\rangle$), and use these to calculate the spin

correlation tensors

$$\begin{aligned} R^{(i)}_{\alpha\beta}(t) &= \frac{1}{Z_i}\mathrm{tr}_i\left[e^{-\mathrm{i}\hat{H}_i t}\sum_{n_i=1}^{2Z_i}|n_i\rangle\langle n_i|\hat{S}_{i\alpha}\; e^{+\mathrm{i}\hat{H}_i t}\sum_{m_i=1}^{2Z_i}|m_i\rangle\langle m_i|\hat{S}_{i\beta}\right] \\ &= \frac{1}{Z_i}\sum_{n_i,m_i=1}^{2Z_i} S^{i\alpha}_{n_i m_i} S^{i\beta}_{m_i n_i} e^{-\mathrm{i}\omega^{(i)}_{n_i m_i} t}, \end{aligned} \tag{2.16}$$

where $S^{i\alpha}_{n_i m_i} = \langle n_i|\hat{S}_{i\alpha}|m_i\rangle$ and $\omega^{(i)}_{n_i m_i} = E_{n_i} - E_{m_i}$. This can now be used to find an alternative expression for the singlet yield[197]

$$\begin{aligned} \Phi_{\mathrm{S}} &= k\int_0^\infty \left(\frac{1}{4} + \sum_{\alpha,\beta=x,y,z} R^{(1)}_{\alpha\beta}(t) R^{(2)}_{\alpha\beta}(t)\right) e^{-kt}\mathrm{d}t \\ &= \frac{1}{4} + k\int_0^\infty \sum_{\alpha,\beta=x,y,z}\left(\frac{1}{Z_1}\sum_{n_1,m_1=1}^{2Z_1} S^{1\alpha}_{n_1 m_1} S^{1\beta}_{m_1 n_1} e^{-\mathrm{i}\omega^{(1)}_{n_1 m_1} t}\right)\times \\ &\qquad\qquad \left(\frac{1}{Z_2}\sum_{n_2,m_2=1}^{2Z_2} S^{2\alpha}_{n_2 m_2} S^{2\beta}_{m_2 n_2} e^{-\mathrm{i}\omega^{(2)}_{n_2 m_2} t}\right) e^{-kt}\mathrm{d}t \\ &= \frac{1}{4} + \frac{1}{Z}\sum_{\alpha,\beta=x,y,z}\sum_{n_1,m_1=1}^{2Z_1}\sum_{n_2,m_2=1}^{2Z_2} S^{1\alpha}_{n_1 m_1} S^{1\beta}_{m_1 n_1} S^{2\alpha}_{n_2 m_2} S^{2\beta}_{m_2 n_2} \frac{k^2}{k^2 + \left(\omega^{(1)}_{n_1 m_1} + \omega^{(2)}_{n_2 m_2}\right)^2}. \end{aligned} \tag{2.17}$$

Using Eq. 2.17 allows us to diagonalise the radical Hamiltonian matrices separately. This means that the bottleneck of the calculation is now instead the double sum over the combined Hilbert space. Therefore, for separable radical pairs – symmetric recombination and zero dipolar and exchange coupling – the computational effort can in general be reduced from $\mathcal{O}(Z^3)$ to $\mathcal{O}(Z^2)$, not to mention that the storage requirements have been vastly reduced as the largest dense matrix that needs to be stored is of dimension $Z_1 \times Z_1$ rather than $Z \times Z$. For the 16 spin calculations presented in Chapter 4, $Z = (3^3 \times 2^{13}) = 221184$, meaning a computational improvement of 5 orders of magnitude (a factor of Z).

B. Discretising in frequency space

Despite the improvement offered by this method, the calculation still becomes quickly impossible for large, multinuclear RPs as a result of the scaling of the double sum over the combined Hilbert space. Building on work from Refs. 169 and 172, we have developed an approximate method to circumvent this difficulty, based on forming histograms of energy differences over a discrete number of bins.

Returning to the expression (Eq. 2.16) for the spin correlation tensors

$$R_{\alpha\beta}^{(i)}(t) = \frac{1}{Z_i} \sum_{n_i,m_i=1}^{2Z_i} S_{n_i m_i}^{i\alpha} S_{m_i n_i}^{i\beta} e^{-\mathrm{i}\omega_{n_i m_i}^{(i)} t} = \sum_{j}^{4Z_i^2} a_{j,\alpha\beta}^{(i)} e^{\mathrm{i}\omega_j^{(i)} t} \tag{2.18}$$

we see that $R_{\alpha\beta}^{(i)}(t)$ can be written in terms of $4Z_i^2$ Fourier components. Rather than include all $4Z_i^2$ frequencies in this sum, we choose to approximate the spin correlation tensor by carefully (see below) discretising frequency space into $N_{\max}$ bins[172]

$$R_{\alpha\beta}^{(i)}(t) \approx \sum_{j}^{N_{\max}} \tilde{a}_{j,\alpha\beta}^{(i)} e^{\mathrm{i}\tilde{\omega}_j^{(i)} t}, \tag{2.19}$$

where $\tilde{\omega}_j^{(i)}$ is the central bin frequency and the terms falling within bin j, i.e. in the interval $\{\tilde{\omega}_j^{(i)} \pm \delta\omega\}$, are summed

$$\tilde{a}_{j,\alpha\beta}^{(i)} = \frac{1}{Z_i} \sum_{\substack{\omega_{n_i m_i}^{(i)} \\ \in \{\tilde{\omega}_j^{(i)} \pm \delta\omega\}}} S_{n_i m_i}^{i\alpha} S_{m_i n_i}^{i\beta}. \tag{2.20}$$

Using this expression for the spin correlation tensors, the singlet yield can be approximated using[172]

$$\begin{aligned} \Phi_{\mathrm{S}} &\approx \frac{1}{4} + k \int_0^\infty \sum_{\alpha,\beta=x,y,z} \sum_{j,l}^{N_{\max}} \tilde{a}_{j,\alpha\beta}^{(1)} \tilde{a}_{l,\alpha\beta}^{(2)} \exp\left(t\left[\mathrm{i}(\tilde{\omega}_j^{(1)} + \tilde{\omega}_l^{(2)}) - k\right]\right) \mathrm{d}t \\ &= \frac{1}{4} + k \sum_{\alpha,\beta=x,y,z} \sum_{j,l}^{N_{\max}} \frac{\tilde{a}_{j,\alpha\beta}^{(1)} \tilde{a}_{l,\alpha\beta}^{(2)}}{k - \mathrm{i}(\tilde{\omega}_j^{(1)} + \tilde{\omega}_l^{(2)})} = \frac{1}{4} + k^2 \sum_{\alpha,\beta=x,y,z} \sum_{j,l}^{N_{\max}} \frac{\tilde{a}_{j,\alpha\beta}^{(1)} \tilde{a}_{l,\alpha\beta}^{(2)}}{k^2 + (\tilde{\omega}_j^{(1)} + \tilde{\omega}_l^{(2)})^2}. \end{aligned} \tag{2.21}$$

Clearly, the number of terms in the inner summation has been changed from $4Z_i^2$ to $N_{\max}^2$.

In order for this method to offer a significant improvement, the histogram bins need to be chosen in such a way as to minimise $N_{\max}$, without sacrificing accuracy in Φ_{S}. An important consideration is that the Laplace transform[15] (the integral transform of $P_{\mathrm{S}}(t)$ with e^{-kt}) in the expression for the singlet yield means that terms which oscillate at frequencies much faster than the time scale of the RP recombination have a negligible contribution to Φ_{S}. Looking at Eq. 2.17, it is clear that terms in the sum for which $\omega_{n_1 m_1}^{(1)} + \omega_{n_2 m_2}^{(2)} \gg k$ are approximately zero, and correspond to Fourier components which average to zero over the RP lifetime.

Therefore, the grid of frequencies should be fine where $\omega_{n_i m_i}^{(i)} \leq k$ to include the slowly oscillating modes, and can be coarser above this. Clearly, this procedure does not guarantee to accurately include contributions for which $\omega_{n_1 m_1}^{(1)} \approx -\omega_{n_2 m_2}^{(2)}$ if they fall in the coarse part of the histogram, which would have a large contribution. However, as the size of the spin system increases, because of the factor of $1/Z$, any single contribution to Φ_{S} becomes negligible and it is therefore possible to use a value of $N_{\max}$ of 5000 to achieve 6 digits of accuracy in Φ_{S}. Again comparing the algorithm efficiency for the 16-spin calculations given in Chapter 4, $Z^2 = 221,184^2$ compared to $N_{\max} = 5000^2$. In this instance, the calculation bottleneck becomes diagonalisation of the individual radical Hamiltonians.

III Asymmetric recombination

In order to test the validity of the assumption that using a symmetric reaction scheme does not obscure any aspects of the RP mechanism, we need a method for calculating the singlet yield when $k_{\mathrm{S}} \neq k_{\mathrm{T}}$.[178] As outlined above, the reactive coupling of the radicals means that we have to work in the combined Hilbert space of the RP,[197] meaning that the computational demands are severe even for a moderate number of spins. Below we outline first the exact, general method to compute Φ_{S},

and then move on to a novel approximate method applicable for slow RP recombination which avoids having to construct any matrices in the combined Hilbert space.

A. General method

Returning to our general expression for the density operator at time t (Eq. 2.4)

$$\hat{\rho}(t) = \exp\left(-\mathrm{i}\hat{H}t - \hat{K}t\right)\hat{\rho}(0)\exp\left(+\mathrm{i}\hat{H}t - \hat{K}t\right) \tag{2.22}$$

this can be re-written in terms of a single operator $\hat{C} = \hat{H} - \mathrm{i}\hat{K}$

$$\hat{\rho}(t) = \exp\left(-\mathrm{i}\hat{C}t\right)\hat{\rho}(0)\exp\left(+\mathrm{i}\hat{C}^{\dagger}t\right). \tag{2.23}$$

We are now working with the non-Hermitian operator $\hat{C}$, whose eigenvalues are in general complex and eigenstates non-orthogonal. Switching to matrix notation for clarity, we see that the eigendecompositions of C and $C^{\dagger}$ are related[5]

$$\left(A^{-1}CA\right)^{\dagger} = c^{*} = A^{\dagger}C^{\dagger}\left(A^{-1}\right)^{\dagger}, \tag{2.24}$$

where c is the diagonal matrix of eigenvalues of C generated on transforming to the eigenbasis, $A^{-1}CA = c$.

We can use identity relations to manipulate our expression for the singlet probability

$$\begin{aligned}
P_{\mathrm{S}}(t) &= \mathrm{tr}\left[\exp\left(-\mathrm{i}Ct\right)\rho(0)\exp\left(+\mathrm{i}C^{\dagger}t\right)P_{\mathrm{S}}\right] \\
&= \mathrm{tr}\left[AA^{-1}\exp\left(-\mathrm{i}Ct\right)AA^{-1}\rho(0)\left(A^{-1}\right)^{\dagger}A^{\dagger}\exp\left(+\mathrm{i}C^{\dagger}t\right)\left(A^{-1}\right)^{\dagger}A^{\dagger}P_{\mathrm{S}}\right] \\
&= \mathrm{tr}\left[\exp\left(-\mathrm{i}ct\right)A^{-1}\frac{1}{Z}P_{\mathrm{S}}\left(A^{-1}\right)^{\dagger}\exp\left(+\mathrm{i}c^{*}t\right)A^{\dagger}P_{\mathrm{S}}A\right] \\
&= \mathrm{tr}\left[\exp\left(-\mathrm{i}ct\right)X\exp\left(+\mathrm{i}c^{*}t\right)Y\right],
\end{aligned} \tag{2.25}$$

where $X = \frac{1}{Z} A^{-1} P_{\mathrm{S}} \left(A^{-1}\right)^{\dagger}$ and $Y = A^{\dagger} P_{\mathrm{S}} A$.

Now we can insert this into the expression for the singlet yield, and evaluate the trace, to find the following closed form expression[5]

$$\begin{aligned}
\Phi_{\mathrm{S}} &= k_{\mathrm{S}} \int_0^{\infty} P_{\mathrm{S}}(t) \mathrm{d}t \\
&= \frac{k_{\mathrm{S}}}{Z} \int_0^{\infty} \sum_{j,k=1}^{4Z} e^{-\mathrm{i}c_j t} X_{jk} e^{+\mathrm{i}c_k^* t} Y_{kj} \mathrm{d}t \\
&= \frac{\mathrm{i}k_{\mathrm{S}}}{Z} \sum_{j,k=1}^{4Z} \frac{X_{jk} Y_{kj}}{c_k^* - c_j}.
\end{aligned} \tag{2.26}$$

Despite the apparent simplicity of this method, the RAM and CPU time requirements for storage and diagonalisation of the C matrix are prohibitive for any system of more than ~ 8 nuclear spins.

B. Non-Hermitian Perturbation Theory

If we are interested primarily in the regime of slow RP recombination, this problem appears to be ideally suited to perturbation theory, as the operator $\mathrm{i}\hat{K}$ is a small, albeit non-Hermitian, perturbation to a solvable Hamiltonian (assuming there are no radical-radical interactions and $\hat{H}$ is therefore separable). Exotic as this may seem, this approach has already been used, for example, in dealing with decay in electronic resonances.[10,174] Obviously, weak dipolar and exchange coupling could be similarly treated using perturbation theory, though generally the magnitude of these terms is not sufficiently different from the interaction strengths in the radical Hamiltonians.[39]

For the recombination to be "slow" means that there is a separation of time scales between the majority of oscillatory modes in the spin dynamics, and the RP decay (e.g. Fig. 2.1). In the language of traditional perturbation theory, the magnitude of the off-diagonal terms of the recombination matrix should be small relative to the energy scale of the system.[111]

First, we must verify that traditional perturbation theory can equally well be applied to a non-Hermitian perturbation. Taking our operator $\hat{C}$ and introducing the dimensionless parameter λ

$$\hat{C}(\lambda) = \hat{H} - \mathrm{i}\lambda\hat{K} \tag{2.27}$$

we can expand the Schrödinger equation as power series in λ

$$\begin{aligned}\left(\hat{H} - \mathrm{i}\lambda\hat{K}\right)\left(|\psi^{(0)}\rangle + \lambda|\psi^{(1)}\rangle + \lambda^2|\psi^{(2)}\rangle + ...\right) = \\ \left(E^{(0)} + \lambda E^{(1)} + \lambda^2 E^{(2)} + ...\right)\left(|\psi^{(0)}\rangle + \lambda|\psi^{(1)}\rangle + \lambda^2|\psi^{(2)}\rangle + ...\right).\end{aligned} \tag{2.28}$$

For non-degnerate eigenstates, the derivation of the first order energy is straightforward. We match terms linear in λ

$$\left(\hat{H} - E^{(0)}\right)|\psi^{(1)}\rangle - \left(\mathrm{i}\hat{K} + E^{(1)}\right)|\psi^{(0)}\rangle = 0. \tag{2.29}$$

Left multiplying by $\langle\psi^{(0)}|$ gives the standard result[111]

$$E^{(1)} = -\langle\psi^{(0)}|\mathrm{i}\hat{K}|\psi^{(0)}\rangle \tag{2.30}$$

where we have not assumed anything about the operator $\mathrm{i}\hat{K}$.

We must also consider the case of (near-)degeneracies in the unperturbed system. Coherences between these states are of a similar time scale to recombination, and so couple to the $\mathrm{i}\hat{K}$ operator. Assuming we have a degenerate manifold of dimension n: $\{|\psi_i^{(0)}\rangle\}$ for $1 \leq i \leq n$, we multiply Eq. 2.29 by $\langle\psi_i^{(0)}|$

$$\langle\psi_i^{(0)}|\mathrm{i}\hat{K}|\psi^{(0)}\rangle + E^{(1)}\langle\psi_i^{(0)}|\psi^{(0)}\rangle = 0. \tag{2.31}$$

Writing the general unperturbed wavefunction as a linear combination of degenerate states

$$|\psi^{(0)}\rangle = \sum_{j=1}^{n} a_j |\psi_j^{(0)}\rangle \tag{2.32}$$

and inserting this into Eq. 2.31 (with $\mathrm{i}K_{ij} = \langle\psi_i^{(0)}|\mathrm{i}\hat{K}|\psi_j^{(0)}\rangle$) gives

$$\sum_{j=1}^{n} \left(\mathrm{i}\hat{K}_{ij} + E^{(1)}\delta_{ij}\right) a_j = 0. \tag{2.33}$$

As for a Hermitian perturbation,[111] this is equivalent to an eigenvalue problem in the $n \times n$ degenerate subspace, and so non-trivial solutions for $\{a_i\}$ are given by the solutions of the determinant equation

$$\det\left(\mathrm{i}\hat{K}_n + E^{(1)}\mathbb{I}_n\right) = 0 \tag{2.34}$$

where $\hat{K}_n$ is the recombination operator and $\mathbb{I}_n$ the identity operator in the degenerate subspace.

Again, this derivation is valid for a completely general $\mathrm{i}\hat{K}$ and the traditional perturbation theory results apply. Our criterion for near-degeneracy is that the energy level spacing is smaller than $10 \times \max(k_\mathrm{S}, k_\mathrm{T})$ so that we include all states with energy differences of a similar magnitude to the off-diagonal matrix elements of $\mathrm{i}\hat{K}$.

Therefore, to generate the first order "energies" we simply take the diagonal matrix elements of the perturbing term or, in the case of near-degeneracies, transform the basis within the subspace of interest such that $\mathrm{i}\hat{K}$ is diagonal. As $\hat{K}$ is Hermitian, it should be clear that these first order corrections will be purely imaginary and we choose to write them $\mathrm{i}\hat{K}_j^{(1)}$ to emphasise that this imaginary term represents the state decay due to recombination.

C. Evaluating the Singlet Yield

We have managed to avoid diagonalisation of the full Hamiltonian in the combined Hilbert space. However, without being able to use the spin correlation tensor formulation to compute Φ_{S}, we are still limited by the fact that memory requirements preclude us from building any dense matrix in the combined Hilbert space, as we require a matrix representation of $\hat{P}_{\mathrm{S}}$. To overcome this difficulty, we exploit the difference in time scales between fast coherent oscillations and the slow recombination rate, to compute contributions to Φ_{S} on the fly.

Returning to our expression for Φ_{S} (Eq. 2.26),[5]

$$\Phi_{\mathrm{S}} = \frac{\mathrm{i}k_{\mathrm{S}}}{Z} \sum_{j,k=1}^{4Z} \frac{X_{jk}Y_{kj}}{c_k^* - c_j}, \tag{2.35}$$

let us write the eigenvalues using the perturbation expansion $c_j = E_j^{(0)} - \mathrm{i}K_j^{(1)}$ where we have explicitly assigned the imaginary part to the RP recombination and the real part to the energy. Then the equation becomes

$$\Phi_{\mathrm{S}} = \frac{k_{\mathrm{S}}}{Z} \sum_{j,k=1}^{4Z} \frac{X_{jk}Y_{kj}}{\mathrm{i}\left(E_j^{(0)} - \mathrm{i}K_j^{(1)} - E_k^{(0)} - \mathrm{i}K_k^{(1)}\right)} \tag{2.36}$$

As a quick check, it should be obvious that if we use this equation with $k_{\mathrm{S}} = k_{\mathrm{T}}$, we recover Eq. 2.12 using this method as all $K_j^{(1)} = k/2$ and X and Y are proportional to P_{S}.

As we have noted previously, the coherences between states well separated in energy relative to the "recombination eigenvalues" have a negligible contribution to the singlet yield – the fast oscillations averaging to zero over the RP lifetime. Intuitively, the rate of recombination for any state cannot be faster than the larger of the two recombination rates. Equivalently, as the eigenvalues of $\hat{P}_{\mathrm{S}}$ and $\hat{P}_{\mathrm{T}}$ are zero and one, the upper bound on $K_j^{(1)}$ is clearly proportional to the maximum of the rate constants i.e. $\frac{1}{2}\max(k_{\mathrm{S}}, k_{\mathrm{T}})$. Therefore, energy gaps much larger than the

largest of the two recombination rates will lead to vanishingly small contributions to the sum in Eq. 2.36.

Using this fact, we choose to discard any terms arising from off-diagonal elements between states that are widely spaced in energy. The same requirement of "widely spaced" states relative to the magnitude of the recombination operator was used in the perturbative diagonalisation of C. The only off-diagonal contributions we will include are from within the nearly-degenerate subspaces used when computing the first order eigenvalues.

Therefore, if we can compute the eigenbasis of $\hat{H}$, we can approximately evaluate the singlet yield. After sorting the states into nearly-degenerate subspaces, we build the corresponding recombination matrix $\hat{K}_n$ and diagonal matrix of energies $E_n^{(0)}$ in each subspace, and diagonalise $\mathrm{i}\hat{K}_n + E_n^{(0)}$ and then sum the contributions to Φ_S in Eq. 2.36 from each subspace. We never have to explicitly build any matrix in the combined Hilbert space, only in these degenerate subspaces, whose dimension will be orders of magnitude smaller, and then only include off-diagonal contributions from within these subspaces to calculate Φ_S.

IV Conclusions

In this chapter we have outlined approximate algorithms for calculating Φ_S for both symmetric and asymmetric recombination reaction schemes in Fig. 1.1. Both methods greatly improve the computational efficiency of the calculations and allow us to present in Chapter 4 simulations of spin systems that are larger than otherwise possible. The perturbative algorithm for asymmetric recombination is only applicable in the regime of slow RP recombination, and so further work could include extending our ability to model such a reaction scheme over all values of k_S and k_T. These methods could also be extended to model a more general reaction scheme such as Fig. 1.4.

One general drawback of all of the presented methods is that inclusion of non-

zero inter-radical coupling remains hugely computationally demanding.[27] In general, when we want to include these interactions, their strength is too large for them to be treated as a perturbation, and therefore we cannot avoid working in the combined Hilbert space of the radicals. This still represents a significant failing in our ability to model RP reactions, and remains an important avenue of future work.

Acknowledgements

The approximate method presented in this chapter for symmetric recombination was first presented in Chris Rodgers's DPhil thesis[169] and published in Ref. 172, and was brought to my attention by Daniel Kattnig. The consideration of how the Laplace transform supresses off-diagonal terms from energy levels widely spaced in energy, thereby allowing us to have a coarse grid in frequency space above k, greatly reducing the number of bins required to accurately calculate Φ_S is a novel improvement on the method.

Chapter 3

Floquet Theory of radical pair reactions

As discussed in Chapter 1, the observed effect of weak radiofrequency (RF) magnetic fields on the ability of migratory birds to magnetically orient[43,98,167,168,179,193,210] remains one of the primary pieces of evidence for the involvement of a radical pair in the sensing mechanism. However, there are a number of contradictory results from behavioural experiments, largely distinguishing between magnetic fields oscillating at a single frequency[168] and broadband RF noise[43] (an overview of the literature is given in Chapter 5). Reservations about the interpretation of the experimental results have also been raised, related to the seemingly extraordinarily long coherence lifetimes the observed effects appear to suggest.[56,81,95,97]

There have been attempts to discuss these results in the theoretical framework of the RP mechanism,[56,203,220] in the hope that agreement between experimental and computational studies would provide proof that a RP compass sense could be sensitive to these weak perturbations, and therefore explain the observed behavioural results. However, these are severely limited by the computational challenges presented by this problem. The findings of previous computational studies are also summarised in Chapter 5.

In this chapter, a novel method will be outlined which allows for efficient calculation of the singlet yield of a RP reaction in the presence of a time-dependent external field.[72] Rather than having to treat vastly simplified RPs and/or being limited to a monochromatic field as in previous work, this algorithm can be readily used for large multinuclear RPs and extended to an approximation of broadband RF noise in a certain parameter range. This method has allowed us to discuss in detail the various experimental results in the literature,[73] presented in Chapter 5.

The algorithm relies on Floquet's Theorem,[51,183] which determines a form for the solutions of a differential equation that is periodic in time, and is derived below. We then use perturbation theory and some numerical considerations to derive our final method, applicable for a certain range of RP recombination rates and RF field strengths.

I Existing methods

Before presenting our novel method, here is a summary of methods that have been used in the past to perform spin dynamics calculations in the presence of time-dependent fields, and the limitations making them unsuitable for extension to more complex systems.

- Direct time propagation[61] – The most generally applicable method is to numerically propagate the system over time and explicitly evaluate the singlet probability at every time step to calculate the singlet yield. This method can incorporate any arbitrarily complicated time dependence of the external field, but suffers from having to propagate the system over very many time steps. As noted by Gauger *et al.*[56] and others, slow RP recombination is required for weak RF fields to have a significant effect on Φ_S. Fig. 3.1 demonstrates this for our simple toy RP (details in Section 3.IV), where the time step used should be small enough to capture the fast oscillations in the spin dynamics,

but the simulation must extend to long times to capture the RF field effect. The prohibitively large number of time steps required rules out this method for our purposes once the size of the spin system (and therefore the Hilbert space) exceeds that of the most simple of systems.

- Semi-classical approaches – There are a number of semi-classical approaches to simulating spin dynamics,[125,132,178] that draw parallels between the quantum system and a classical analogue in order to avoid the exponential scaling of the Hilbert space. Unfortunately, these methods also rely on a propagation over time, and therefore are again unsuitable for simulating long-lived RPs. Additionally, it remains to be seen whether these methods could capture quantum phenomena such as resonance effects; for instance, the semi-classical algorithm outlined in Ref. 132 does not capture the spike arising from an avoided crossing in Chapter 4.[123,124]

- γ-COMPUTE[38,121] and Average Hamiltonian[45] – These two methods are both based on calculating the eigendecomposition of the propagator for a whole period of a periodic interaction. This involves discretising in time such that the Hamiltonian is approximately static over the time interval and evaluating the propagator for each time interval. Even for a monochromatic field, this requires the calculation and storage of a significant number of matrix exponentials, which makes these methods prohibitively expensive when including many nuclear spins (due to the size of the Hilbert space), not to mention the extra complication of simulating broadband noise fields.

- Existing Floquet Theory-based methods[25,37,51,118,175] – There are many existing methods which make use of Floquet's Theorem, and they are used extensively in magic angle spinning (MAS) NMR. When coupled with van Vleck perturbation theory,[45] this can result in powerful algorithms. However, using van Vleck perturbation theory requires a separation of energy scales between

the energies of the system and the frequency of the slowest oscillating mode in the Hamiltonian, which is exactly the opposite of the resonant regime we wish to explore. Otherwise, the calculations require a time propagation or diagonalisation of truncated forms of the infinite matrices associated with Floquet Theory, truncation which is not feasible for our application.

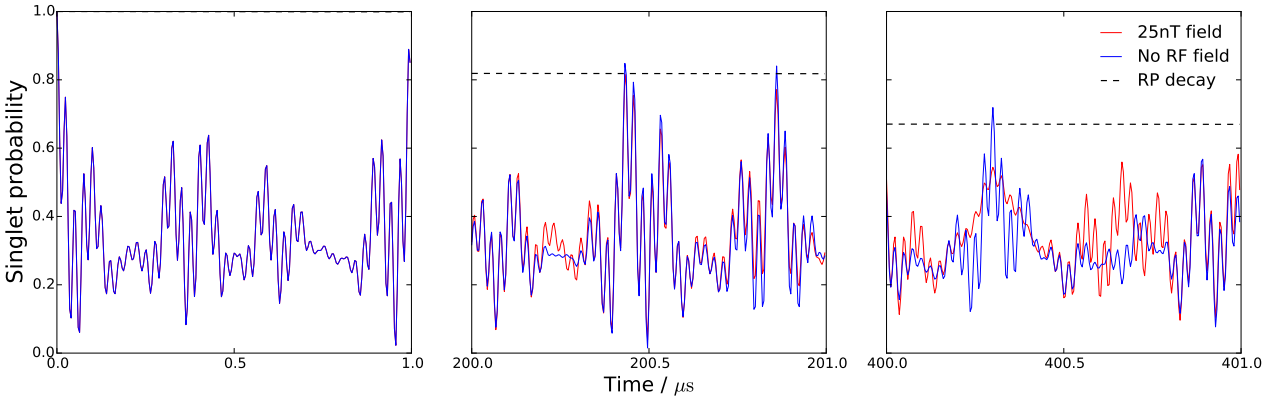


Figure 3.1: The singlet probability of the toy radical pair with and without a monochromatic RF field that is resonant with an energy level transition. Included is the decaying exponential representing loss of RP population for $k = 10^3$ s^{-1}

II Floquet Theory in Quantum Mechanics

The general results of Floquet Theory as applied to Quantum Mechanics by Shirley[182,183] are presented here. As a starting point we derive Floquet's Theorem, which is the time analogue of Bloch's Theorem for potentials periodic in space, wherein the solutions of the Schrödinger equation can be written as a periodic function multiplied by a complex exponential quasi-energy term.[51] Shirley extended this treatment to show that there is a mapping between the time-dependent problem and an infinite-dimensional time-*independent* eigenvalue problem.[182,183] We adopt this formalism to derive a novel expression for the propagator and use it to write a closed form expression for a general expectation value in a system with interactions that are periodic in time.

The differential equation that underlies this problem is the time-dependent Schrödinger equation

$$\mathrm{i}\frac{\mathrm{d}}{\mathrm{d}t}\Psi(t) = H(t)\Psi(t) \tag{3.1}$$

where the Hamiltonian, $H(t)$ is periodic in time with period $T = 2\pi/\omega$. In applying this theory to broadband noise, we will later choose to model the noise as a grid of equally spaced frequencies, where the frequency spacing defines ω and therefore the periodicity of $H(t)$.

A. Floquet's Theorem in matrix notation

Let $X(t)$ be a fundamental matrix solution to Eq. 3.1 i.e. $X(t)$ satisfies $\det[X(t)] \neq 0$ and is a solution of the matrix equation

$$\mathrm{i}\frac{\mathrm{d}}{\mathrm{d}t}X(t) = H(t)X(t). \tag{3.2}$$

If we consider time $t + T$, we find that the periodicity of $H(t)$ means $X(t + T)$ and $X(t)$ satisfy the same differential equation. They must therefore be equal up to multiplication by a constant matrix, A. On diagonalising A using the unitary transformation matrix R, we choose to write the eigenvalues of A as $e^{-\mathrm{i}q_\alpha T}$. If Q is the diagonal matrix with elements q_α,

$$X(t+T) = X(t)A = X(t)Re^{-\mathrm{i}QT}R^{-1}. \tag{3.3}$$

Multiplying on the right by $Re^{\mathrm{i}Q(t+T)}$

$$X(t+T)Re^{\mathrm{i}Q(t+T)} = X(t)Re^{\mathrm{i}Qt}. \tag{3.4}$$

If the right hand side is denoted $\Theta(t)$, it is clear from Eq. 3.4 that $\Theta(t+T) = \Theta(t)$ i.e. that $\Theta(t)$ is a matrix of periodic functions in time with period T. As $X(t)R$ is a solution of Eq. 3.1, it follows that the solutions can be written in the form:

$\Theta(t)e^{-\mathrm{i}Qt}$. This is Floquet's Theorem in matrix notation.[182] The q_αs are known as the characteristic exponentials, sometimes called the quasi-energies by analogy with time-independent quantum mechanics although it is yet to be shown that the q_αs are real; it will turn out that they are the eigenvalues of the Hermitian "Floquet Hamiltonian".[183]

B. An infinite-dimensional eigenvalue problem

We have shown that the solution of the time-dependent Schrödinger equation (Eq. 3.1) with a periodic Hamiltonian is the product of a periodic matrix and an exponentiated diagonal matrix[182]

$$\Psi(t) = \Theta(t)e^{-\mathrm{i}Qt}. \tag{3.5}$$

Since $H(t)$ is Hermitian, $\Psi(t)$ is unitary and so we can write the time-evolution operator as

$$U(t;t_0) = \Psi(t)\Psi^{-1}(t_0). \tag{3.6}$$

Expanding $\Theta(t)$ and $H(t)$ as Fourier series with Greek letters to denote Hilbert space basis states and Roman letters to label Fourier components,

$$\Psi_{\alpha\beta}(t) = \sum_n \Theta^n_{\alpha\beta} e^{-\mathrm{i}q_\beta t} e^{+\mathrm{i}n\omega t}, \tag{3.7}$$

$$H_{\alpha\beta}(t) = \sum_n H^n_{\alpha\beta} e^{+\mathrm{i}n\omega t}, \tag{3.8}$$

substituting these into Eq. 3.1,

$$\sum_n (q_\beta - n\omega)\, \Theta^n_{\alpha\beta} e^{+\mathrm{i}n\omega t} e^{-\mathrm{i}q_\beta t} = \sum_{mk} H^m_{\alpha\gamma} \Theta^k_{\gamma\beta} e^{+\mathrm{i}(m+k)\omega t} e^{-\mathrm{i}q_\beta t} \tag{3.9}$$

and matching coefficients of $e^{+\mathrm{i}n\omega t}e^{-\mathrm{i}q_\beta t}$ gives

$$(q_\beta - n\omega)\Theta^n_{\alpha\beta} = \sum_k H^{n-k}_{\alpha\gamma} \Theta^k_{\gamma\beta}. \tag{3.10}$$

Introducing Kronecker deltas allows us to write the infinite eigenvalue equation associated with Floquet Theory[182]

$$\sum_k \left(H^{n-k}_{\alpha\gamma} + n\omega\delta_{\alpha\gamma}\delta_{kn}\right)\Theta^k_{\gamma\beta} = q_\beta\Theta^n_{\alpha\beta}. \tag{3.11}$$

The operator in parentheses is called the "Floquet Hamiltonian" and is written $\hat{H}_{\mathrm{F}}$. Now it is apparent that the q_βs are real and can therefore be thought of as quasi-energies, as $\hat{H}_{\mathrm{F}}$ is Hermitian. Approximate diagonalisation of this infinite matrix in order to determine the characteristic exponentials is the major challenge of solving systems involving periodically varying interactions using this formalism.

At this point, it is useful to introduce a basis of the infinite dimensional "Floquet" space as[120] $\{|\alpha\rangle, |\beta\rangle, ...\} \otimes \mathbb{Z} = \{..., |\alpha n\rangle, |\alpha n+1\rangle, ..., |\beta m\rangle, |\beta m+1\rangle, ...\}$. This basis allows us to more formally define $\hat{H}_{\mathrm{F}}$

$$\langle \alpha n|\hat{H}_{\mathrm{F}}|\beta m\rangle = H^{n-m}_{\alpha\beta} + n\omega\delta_{\alpha\beta}\delta_{nm} \tag{3.12}$$

and construct it's matrix representation

$$H_{\mathrm{F}} = \left(\begin{array}{c|c|c|c|c} \ddots & & & & \ddots \\ \hline & H^{(0)} + \omega\mathbb{I} & H^{(1)} & H^{(2)} & \\ \hline & H^{(-1)} & H^{(0)} & H^{(1)} & \\ \hline & H^{(-2)} & H^{(-1)} & H^{(0)} - \omega\mathbb{I} & \\ \hline \ddots & & & & \ddots \end{array}\right). \tag{3.13}$$

C. The propagator and expectation values in Floquet space

Shirley showed that it is possible to derive a closed form expression for the time evolution operator in Floquet space by utilising properties of the eigenvalues and eigenvectors of H_{F}, which arise from the Floquet Hamiltonian's periodic structure.[182] This construction is presented below, before the derivation of an alternative form of

the propagator more well suited to our application.

Periodicity properties

Let us write the eigenvalues and eigenvectors of $\hat{H}_{\mathrm{F}}$ as $\lambda_{\beta m}$ and $|\lambda_{\beta m}\rangle$ respectively:

$$\hat{H}_{\mathrm{F}}|\lambda_{\beta m}\rangle = \lambda_{\beta m}|\lambda_{\beta m}\rangle. \tag{3.14}$$

If we left-multiply by $\langle \alpha n|$ and insert the unit operator over the Floquet basis ($\mathbb{I}_{\mathrm{F}} = \sum_{\gamma k} |\gamma k\rangle\langle \gamma k|$), this eigenvalue equation becomes analogous to that including $\Theta(t)$ and the quasi-energy q_β (substituting the matrix element in Eq. 3.12 into Eq. 3.11)

$$\sum_{\gamma k}\langle \alpha n|\hat{H}_{\mathrm{F}}|\gamma k\rangle\langle \gamma k|\lambda_{\beta m}\rangle = \lambda_{\beta m}\langle \alpha n|\lambda_{\beta m}\rangle. \tag{3.15}$$

If we consider the structure of $\hat{H}_{\mathrm{F}}$, it should be evident that adding an arbitrary multiple of $\omega\mathbb{I}$ is equivalent to redefining the Fourier components corresponding to each diagonal block, i.e. $n \to n'$. In other words, in evaluating $\det(H_{\mathrm{F}} - \lambda\mathbb{I}) = 0$ the determinant is unchanged if we replace λ by $\lambda + p\omega$. This defines the first periodicity condition, that if λ is an eigenvalue of $\hat{H}_{\mathrm{F}}$ then so is $\lambda + p\omega$ for any integer p.

In the notation adopted above, we define

$$\lambda_{\beta m} = q_\beta + m\omega. \tag{3.16}$$

This being the case, $\Theta^n_{\alpha\beta}$ and $\langle \alpha n|\lambda_{\beta 0}\rangle$ satisfy the same eigenvalue equation of $\hat{H}_{\mathrm{F}}$ (as $q_\beta = \lambda_{\beta 0}$) and are therefore proportional. Since $H(t)$ is Hermitian and $\Theta(t)$ is unitary, this proportionality can be chosen to be equality

$$\Theta^n_{\alpha\beta} = \langle \alpha n|\lambda_{\beta 0}\rangle. \tag{3.17}$$

Another important periodicity property exists between eigenvector components. The analogous expression to Eq. 3.15 for $\langle \alpha n + p|\lambda_{\beta m+p}\rangle$ can be written using a

carefully chosen form of the Floquet space unit operator, $\mathbb{I}_{\mathrm{F}} = \sum_{\gamma k} |\gamma k + p\rangle\langle\gamma k + p|$

$$\sum_{\gamma k} \langle \alpha n + p | \hat{H}_{\mathrm{F}} | \gamma k + p \rangle \langle \gamma k + p | \lambda_{\beta m+p} \rangle = \lambda_{\beta m+p} \langle \alpha n + p | \lambda_{\beta m+p} \rangle. \tag{3.18}$$

This relation holds for any integer q. Using the definition of $\hat{H}_{\mathrm{F}}$ and the periodicity of $\lambda_{\beta m+p}$

$$\sum_{\gamma k} \Big(\langle \alpha n | \hat{H}_{\mathrm{F}} | \gamma k \rangle + p\omega \delta_{\alpha\gamma} \delta_{nk} \Big) \langle \gamma k + p | \lambda_{\beta m+p} \rangle = \Big(\lambda_{\beta m} + p\omega \Big) \langle \alpha n + p | \lambda_{\beta m+p} \rangle. \tag{3.19}$$

The $p\omega$ terms on either side cancel to leave

$$\sum_{\gamma k} \langle \alpha n | \hat{H}_{\mathrm{F}} | \gamma k \rangle \langle \gamma k + p | \lambda_{\beta m+p} \rangle = \lambda_{\beta m} \langle \alpha n + p | \lambda_{\beta m+p} \rangle. \tag{3.20}$$

This is the same equation as is satisfied by $\langle \alpha n | \lambda_{\beta m} \rangle$, with all Fourier indices shifted by $+p$. Again, as both $\langle \alpha n | \lambda_{\beta m} \rangle$ and $\langle \alpha n + p | \lambda_{\beta m+p} \rangle$ satisfy the same homogeneous equations, they are equal up to an arbitrary phase which is set to unity,

$$\langle \alpha n | \lambda_{\beta m} \rangle = \langle \alpha n + p | \lambda_{\beta m+p} \rangle. \tag{3.21}$$

The propagator

Using these periodicity properties, we can finally derive an expression for the time-evolution operator in Floquet space as first presented by Shirley. Combining Eqs. 3.7 and 3.17, we can write

$$\Psi_{\alpha\beta}(t) = \sum_{n} \langle \alpha n | \lambda_{\beta 0} \rangle e^{+\mathrm{i}n\omega t} e^{-\mathrm{i}q_\beta t}. \tag{3.22}$$

Substituting this into Eq. 3.6 gives

$$\begin{aligned} U_{\beta\alpha}(t;t_0) &= \sum_{\gamma} \Psi_{\beta\gamma}(t)\Psi^{-1}_{\gamma\alpha}(t_0) \\ &= \sum_{\gamma} \left(\sum_{n} \langle \beta n | \lambda_{\gamma 0} \rangle e^{+\mathrm{i}n\omega t} e^{-\mathrm{i}q_\gamma t} \right) \left(\sum_{m} \langle \lambda_{\gamma 0} | \alpha m \rangle e^{-\mathrm{i}m\omega t_0} e^{+\mathrm{i}q_\gamma t_0} \right). \end{aligned} \tag{3.23}$$

Simplification of this expression requires three steps: shift eigenvectors by $l = -m$ and rewrite $q_\gamma = \lambda_{\gamma 0}$; shift eigenvalues using $\lambda_{\gamma l} = \lambda_{\gamma 0} + l\omega$; replace $\lambda_{\gamma l}$ with $\hat{H}_{\mathrm{F}}$ in the exponential, use the completeness of the set of eigenvectors $|\lambda_{\gamma l}\rangle$ to extract the unit operator and relabel $n + l$ as n[120,183]

$$\begin{aligned} U_{\beta\alpha}(t;t_0) &= \sum_{nl} \sum_{\gamma} \langle \beta n + l | \lambda_{\gamma l} \rangle e^{+\mathrm{i}n\omega t} e^{-\mathrm{i}\lambda_{\gamma 0} t} \langle \lambda_{\gamma l} | \alpha 0 \rangle e^{+\mathrm{i}l\omega t_0} e^{+\mathrm{i}\lambda_{\gamma 0} t_0} \\ &= \sum_{nl} \sum_{\gamma} \langle \beta n + l | \lambda_{\gamma l} \rangle e^{-\mathrm{i}\lambda_{\gamma l}(t-t_0)} \langle \lambda_{\gamma l} | \alpha 0 \rangle e^{+\mathrm{i}(n+l)\omega t} \\ &= \sum_{n} \langle \beta n | e^{-\mathrm{i}H_{\mathrm{F}}(t-t_0)} | \alpha 0 \rangle e^{+\mathrm{i}n\omega t}. \end{aligned} \tag{3.24}$$

The matrix element $U_{\beta\alpha}(t;t_0)$ gives the amplitude of scattering from state α at time t_0 to state β at time t under the influence of the time-dependent Hamiltonian $H(t)$. The above expression offers another interpretation, that the initial state $|\alpha 0\rangle$ evolves under a time-independent Hamiltonian to states $|\beta n\rangle$. The amplitude must include the sum over all Fourier components and we have this weighting factor $e^{+\mathrm{i}n\omega t}$. This time-dependent term proves cumbersome when computing expectation values. Below is a derivation of an alternative form of the propagator, which does not include this time-dependency.

An alternative propagator

If instead of shifting the Floquet eigenstates in Eq. 3.24 such that the zero Fourier component appears on the right as $|\alpha 0\rangle$, we shift by $l = -n$ resulting in a $\langle \beta 0|$ on

the left we find

$$\begin{aligned} U_{\beta\alpha}(t;t_0) &= \sum_{ml}\sum_{\gamma}\langle\beta 0|\lambda_{\gamma l}\rangle e^{-\mathrm{i}l\omega t}e^{-\mathrm{i}\lambda_{\gamma 0}t}\langle\lambda_{\gamma l}|\alpha m+l\rangle e^{-\mathrm{i}m\omega t_0}e^{+\mathrm{i}\lambda_{\gamma 0}t_0} \\ &= \sum_{ml}\sum_{\gamma}\langle\beta 0|\lambda_{\gamma l}\rangle e^{-\mathrm{i}\lambda_{\gamma l}(t-t_0)}\langle\lambda_{\gamma l}|\alpha m\rangle e^{-\mathrm{i}m\omega t_0} \\ &= \sum_{m}\langle\beta 0|e^{-\mathrm{i}H_{\mathrm{F}}(t-t_0)}|\alpha m\rangle e^{-\mathrm{i}m\omega t_0}. \end{aligned} \tag{3.25}$$

While the physical interpretation of this form of the propagator is not obvious, the advantage is immediately apparent; the time-dependence of the weighting factors of each Fourier component is replaced by constant complex exponentials. This result has been presented before in the literature[23] as an "unusual representation", the significance seemingly missed. We will use it to derive an expression for expectation values and contrast this with that found using the standard formulation.

Expectation values

Working in the density operator formalism, we are interested in calculating expectation values using $\rho(t)$, the density operator at time t

$$\langle A(t;t_0)\rangle = \mathrm{tr}\left[\hat{A}\hat{\rho}(t)\right] = \mathrm{tr}\left[\hat{A}\ U(t;t_0)\hat{\rho}(t_0)U(t;t_0)^{\dagger}\right]. \tag{3.26}$$

Inserting resolutions of the identity using the Hilbert space basis gives

$$\langle A(t;t_0)\rangle = \sum_{\alpha\beta\gamma\delta}(A)_{\delta\alpha}\,U_{\alpha\beta}(t;t_0)\,(\rho(t_0))_{\beta\gamma}\,U_{\gamma\delta}(t,t_0)^{\dagger}. \tag{3.27}$$

We now use our alternative form of the time evolution operator (Eq. 3.25) to write this in the Floquet space basis

$$\begin{aligned} \langle A(t;t_0)\rangle = \sum_{\alpha\beta\gamma\delta}\sum_{nm}(A)_{\delta\alpha}\,\langle\alpha,0|e^{-\mathrm{i}\hat{H}_{\mathrm{F}}(t-t_0)}|\beta,m\rangle e^{-\mathrm{i}m\omega t_0}\,(\rho(t_0))_{\beta\gamma} \\ \times e^{+\mathrm{i}n\omega t_0}\langle\gamma,n|e^{+\mathrm{i}\hat{H}_{\mathrm{F}}(t-t_0)}|\delta,0\rangle. \end{aligned} \tag{3.28}$$

We introduce a trace over Floquet space so as to write this expression in the same form as Eq. 3.26 and to find Floquet space analogues of the initial density operator and detection operator

$$\begin{aligned}\langle A(t;t_0)\rangle &= \mathrm{tr}_{\mathrm{F}}\left[\hat{A}_{\mathrm{F}}e^{-\mathrm{i}\hat{H}_{\mathrm{F}}(t-t_0)}\hat{\rho}_{\mathrm{F}}(t_0)e^{+\mathrm{i}\hat{H}_{\mathrm{F}}(t-t_0)}\right] \\ &= \sum_{\alpha\beta\gamma\delta}\sum_{nm}\mathrm{tr}_{\mathrm{F}}\Big[|\delta,0\rangle\,(A)_{\delta\alpha}\,\langle\alpha,0|e^{-\mathrm{i}\hat{H}_{\mathrm{F}}(t-t_0)}|\beta,m\rangle \\ &\qquad\qquad e^{-\mathrm{i}m\omega t_0}\,(\rho(t_0))_{\beta\gamma}\,e^{+\mathrm{i}n\omega t_0}\langle\gamma,n|e^{+\mathrm{i}\hat{H}_{\mathrm{F}}(t-t_0)}\Big].\end{aligned} \tag{3.29}$$

We can immediately identify the form of the Floquet-space density and detection operators[72]

$$\hat{A}_{\mathrm{F}} = \sum_{\alpha\beta}|\alpha,0\rangle\langle\alpha|\hat{A}|\beta\rangle\langle\beta,0|, \tag{3.30}$$

$$\hat{\rho}_{\mathrm{F}}(t_0) = \sum_{\alpha\beta}\sum_{nm}|\alpha,m\rangle\langle\alpha|\hat{\rho}(t_0)|\beta\rangle\langle\beta,n|e^{+\mathrm{i}(n-m)\omega t_0}, \tag{3.31}$$

with matrix representations

$$A_{\mathrm{F}} = \left(\begin{array}{c|ccc|c} \ldots & & & & \ldots \\ \hline & 0 & 0 & 0 & \\ \hline & 0 & A & 0 & \\ \hline & 0 & 0 & 0 & \\ \hline \ldots & & & & \ldots \end{array}\right), \tag{3.32}$$

$$\rho_{\mathrm{F}}(t_0) = \left(\begin{array}{c|ccc|c} \ldots & & & & \ldots \\ \hline & \rho(t_0) & \rho(t_0)e^{+\mathrm{i}\omega t_0} & \rho(t_0)e^{+2\mathrm{i}\omega t_0} & \\ \hline & \rho(t_0)e^{-\mathrm{i}\omega t_0} & \rho(t_0) & \rho(t_0)e^{+\mathrm{i}\omega t_0} & \\ \hline & \rho(t_0)e^{-2\mathrm{i}\omega t_0} & \rho(t_0)e^{-\mathrm{i}\omega t_0} & \rho(t_0) & \\ \hline \ldots & & & & \ldots \end{array}\right). \tag{3.33}$$

The advantage of using our alternative form of the propagator over the traditional one is made apparent when these Floquet space operators are compared with those

derived using the usual formulation[120]

$$\hat{A}_{\mathcal{F}}(t) = \sum_{\alpha\beta}\sum_{nm} |\alpha, m\rangle\langle\alpha|\hat{A}|\beta\rangle\langle\beta, n|e^{-\mathrm{i}(n-m)\omega t}, \tag{3.34}$$

$$\hat{\rho}_{\mathcal{F}}(t_0) = \sum_{\alpha\beta} |\alpha, 0\rangle\langle\alpha|\hat{\rho}(t_0)|\beta\rangle\langle\beta, 0|. \tag{3.35}$$

The cumbersome time-dependence that appears in the detection operator is removed in our formulation, replaced by constant complex exponentials in $\hat{\rho}_{\mathrm{F}}(t_0)$ that are simply equal to unity if t_0 is taken to be 0 as is often the natural choice.

An alternative detection operator

Looking at the matrix representations of the various Floquet space operators (Eqs. 3.32 and 3.33), it is clear that while H_{F} and $\rho_{\mathrm{F}}(t_0)$ exhibit some symmetry with respect to the Fourier index, A_{F} has only one non-zero block and so one value of n is distinct from the rest. In order to evaluate the singlet yield, it will be necessary to exploit the symmetry in the Floquet space operators and therefore we choose an alternative form of the detection operator – as we have combined the reference Hilbert space basis with a Fourier basis, we have introduced a degree of freedom in the definition of A_{F} and there is not a unique form of this operator.

Again using the periodicity properties of $\lambda_{\gamma l}$ and $|\lambda_{\gamma l}\rangle$, we revisit our expression for the propagator, Eq. 3.25, and shift eigenstates by an arbitrary integer q (relabelling $m + q$ as m in the final line)

$$\begin{aligned} U_{\beta\alpha}(t; t_0) &= \sum_{ml}\sum_{\gamma} \langle\beta 0|\lambda_{\gamma l}\rangle e^{-\mathrm{i}\lambda_{\gamma l}(t-t_0)}\langle\lambda_{\gamma l}|\alpha m\rangle e^{-\mathrm{i}m\omega t_0} \\ &= \sum_{ml}\sum_{\gamma} \langle\beta q|\lambda_{\gamma l+q}\rangle e^{-\mathrm{i}(\lambda_{\gamma l+q}-q\omega)(t-t_0)}\langle\lambda_{\gamma l+q}|\alpha m+q\rangle e^{-\mathrm{i}m\omega t_0} \\ &= \sum_{m} \langle\beta q|e^{-\mathrm{i}H_{\mathrm{F}}(t-t_0)}|\alpha m\rangle e^{-\mathrm{i}m\omega t_0} e^{+\mathrm{i}q\omega t}. \end{aligned} \tag{3.36}$$

Inserting this into the expression for the expectation value will yield

$$\begin{aligned}\langle A(t;t_0)\rangle = \sum_{\alpha\beta\gamma\delta}\sum_{nm}(A)_{\delta\alpha}\,\langle\alpha,q|e^{-\mathrm{i}\hat{H}_\mathrm{F}(t-t_0)}|\beta,m\rangle e^{-\mathrm{i}m\omega t_0}\,(\rho(t_0))_{\beta\gamma} \\ \times e^{+\mathrm{i}n\omega t_0}\langle\gamma,n|e^{+\mathrm{i}\hat{H}_\mathrm{F}(t-t_0)}|\delta,q\rangle\end{aligned} \tag{3.37}$$

where the $e^{+\mathrm{i}q\omega t}$ from $U_{\beta\alpha}(t,t_0)$ has cancelled with a $e^{-\mathrm{i}q\omega t}$ term from the Hermitian conjugate propagator, $U_{\gamma\delta}(t,t_0)^\dagger$. This result should not be surprising, as on going from the Hilbert space basis to the Floquet basis, we have a free choice of zero for the Fourier index, and a shift by any integer q is equivalent to redefining this zero.

Averaging over q between $-Q$ and Q and taking the limit as $Q\to\infty$, we can write the Floquet space detection operator as[72]

$$\hat{A}_\mathrm{F} = \lim_{Q\to\infty}\frac{1}{2Q+1}\sum_{q=-Q}^{Q}\sum_{\alpha\beta}|\alpha,q\rangle\langle\alpha|\hat{A}|\beta\rangle\langle\beta,q|. \tag{3.38}$$

The matrix representation shows explicitly that the detection operator now exhibits the symmetry with respect to Fourier index we were after, with the same Hilbert space-sized matrix A in *all* diagonal blocks

$$A_\mathrm{F} = \lim_{Q\to\infty}\frac{1}{2Q+1}\begin{pmatrix} \cdots & & & & \cdots \\ & A & 0 & 0 & \\ & 0 & A & 0 & \\ & 0 & 0 & A & \\ \cdots & & & & \cdots \end{pmatrix}. \tag{3.39}$$

D. Diagonalising the Floquet Hamiltonian

With this set of Floquet space matrices, we now need to perform an approximate eigendecomposition of H_F. The approach taken by several studies[118,120] is to truncate the Floquet Hamiltonian, including only a certain range of Fourier indices and

diagonalising this enlarged matrix numerically[1]. We will be unable to use this approach, as we wish to be able to perform the diagonalisation with thousands of Fourier components in $H(t)$ and a high-dimensional Hilbert space. Instead, we will use perturbative methods as, for our application, the time-dependent interactions are significantly weaker than the static Hamiltonian $H^{(0)}$.

A single resonance

As an illustrative starting point, let us consider a single applied Fourier component

$$\hat{H}(t) = \hat{H}^{(0)} + \hat{H}' \cos(\omega t + \delta) \tag{3.40}$$

for which H_{F} is tri-block-diagonal with $\frac{1}{2}H'e^{\pm \mathrm{i}\delta}$ on the super- and sub-diagonal blocks. Physical intuition would tell us that, for weak fields, the most significant effect occurs when the field is oscillating at a frequency resonant with an energy level transition in the reference system i.e. $E_\beta - E_\alpha \simeq \omega$. We assume any non-resonant effects are negligible, and simply aim to capture these resonances.

If we are using the eigenbasis of $H^{(0)}$, it is clear that a resonance corresponds to a degeneracy between the β state in the n^{th} block and α state in the $(n+1)^{\mathrm{th}}$ block. Shirley discussed how the periodicity of H_{F} means that there is a 2-dimensional degenerate subspace for each pair of $|\beta n\rangle$ and $|\alpha n+1\rangle$ states,[183] each with the same 2×2 sub-matrix shifted by a multiple of the identity

$$\tilde{H}_{\mathrm{F}} = \begin{pmatrix} E_\alpha + \omega & \frac{1}{2}H'_{\alpha\beta}e^{+\mathrm{i}\delta} \\ \frac{1}{2}H'_{\beta\alpha}e^{-\mathrm{i}\delta} & E_\beta \end{pmatrix} + n\omega\mathbb{I}_2. \tag{3.41}$$

Using the general result from degenerate perturbation theory, we diagonalise this sub-matrix to find the first order corrected energies $\tilde{E}_\alpha + \omega$ and $\tilde{E}_\beta$. Then the

[1] Clearly this approach would use the form of the detection operator in Eq. 3.30 as it relies on this matrix being largely zero.

approximate eigenvalues and eigenstates of H_{F} are

$$\begin{aligned} \lambda_{\alpha n} &= \tilde{E}_\alpha + n\omega, \quad |\lambda_{\alpha n}\rangle = |\alpha n\rangle U_{\alpha\alpha} + |\beta n - 1\rangle U_{\beta\alpha}, \\ \lambda_{\beta n} &= \tilde{E}_\beta + n\omega, \quad |\lambda_{\beta n}\rangle = |\beta n\rangle U_{\beta\beta} + |\alpha n - 1\rangle U_{\alpha\beta}, \end{aligned} \tag{3.42}$$

where we have defined the unitary matrix U to transform to the eigenbasis of $\tilde{H}_{\mathrm{F}}$

$$U = \begin{pmatrix} U_{\alpha\alpha} & U_{\alpha\beta} \\ U_{\beta\alpha} & U_{\beta\beta} \end{pmatrix}. \tag{3.43}$$

The non-resonant energies and states are unaltered and we have approximately diagonalised H_{F} to first order in H' for this simple example. As a check, we can confirm that the eigenvalues and eigenstates satisfy the periodicity conditions central to Floquet theory.

General procedure

Moving away from the contrived example given above, the same method can be extended to more complicated situations.[72] The general procedure is to build and diagonalise the Floquet Hamiltonian in subspaces of arbitrary dimension corresponding to sets of nearly-degenerate states. The degenerate subspaces can include overlapping/simultaneous resonances (states from different diagonal blocks) or degeneracies in the unperturbed system (multiple states from the same diagonal block), and allow us also to include a large number of Fourier components.

There are restrictions on the applicability of this method. Firstly, in order for each degenerate subspace to be well separated from other copies $\omega \gg |H'|$. Second, it is possible that a degenerate subspace can exceed the size of the Hilbert space for many states and many Fourier components in $H(t)$. As this could lead to diagonalisation of a very large matrix, we opt to build a Hilbert space-sized matrix containing at least the $N - 1$ *closest* resonances. Clearly, discarding some of the more distant near resonances is an approximation, but we assume that the off-diagonal coupling

terms in H_{F} are of similar size and so the closest resonances have the largest effect on the system.

Therefore, diagonalisation of the infinite Floquet Hamiltonian can be approximated using a single diagonalisation of a Hilbert space-sized sub-matrix, $\tilde{H}_{\mathrm{F}}$ which is carefully constructed to include the $N-1$ nearest resonances,[72] which is no more expensive than diagonalising $H^{(0)}$. An example set of matrices is given below.

III Application to Radical Pair reactions

Returning to calculating the singlet yield of RP reactions, we can use this Floquet machinery to find a Floquet space expression for Φ_{S}. We assume for simplicity that the recombination is symmetric, which allows us to employ simplifications which make possible the evaluation of the trace over the infinite Floquet basis.

First, forming the Floquet space operators $\hat{\rho}(0)$ and $\hat{A}_{\mathrm{F}}$ from our initial density and detection operators (Z is as defined in Eq. 2.2)

$$\hat{\rho}_{\mathrm{F}}(0) = \frac{1}{Z}\sum_{\alpha\beta}\sum_{nm}|\alpha,m\rangle\langle\alpha|\hat{P}_{\mathrm{S}}|\beta\rangle\langle\beta,n|, \tag{3.44}$$

$$\hat{A}_{\mathrm{F}} = \lim_{Q\to\infty}\frac{1}{2Q+1}\sum_{q=-Q}^{Q}\sum_{\alpha\beta}|\alpha,q\rangle\langle\alpha|\hat{P}_{\mathrm{S}}|\beta\rangle\langle\beta,q|, \tag{3.45}$$

we can write the singlet probability by analogy with the method used in the previous chapter, inserting resolutions of the identity in the Floquet eigenbasis

$$\begin{aligned} P_{\mathrm{S}}(t) &= \mathrm{tr}_{\mathrm{F}}\left[\hat{A}_{\mathrm{F}}e^{-\mathrm{i}\hat{H}_{\mathrm{F}}t}\hat{\rho}_{\mathrm{F}}(0)e^{+\mathrm{i}\hat{H}_{\mathrm{F}}t}\right] \\ &= \sum_{\alpha\beta}\sum_{nm}\langle\lambda_{\alpha m}|\hat{A}_{\mathrm{F}}|\lambda_{\beta n}\rangle\langle\lambda_{\beta n}|\hat{\rho}_{\mathrm{F}}(0)|\lambda_{\alpha m}\rangle e^{+\mathrm{i}(\lambda_{\alpha m}-\lambda_{\beta n})t}. \end{aligned} \tag{3.46}$$

Inserting this into the expression for the singlet yield[197] (Eq. 2.10) gives our expression for Φ_{S} in terms of Floquet operators[72] in Eqs. 3.44 and 3.45

$$\begin{aligned}\Phi_{\mathrm{S}} &= k\int_0^\infty P_{\mathrm{S}}(t)e^{-kt}\mathrm{d}t \\ &= \sum_{\alpha\beta}\sum_{nm}\langle\lambda_{\alpha m}|\hat{A}_{\mathrm{F}}|\lambda_{\beta n}\rangle\langle\lambda_{\beta n}|\hat{\rho}_{\mathrm{F}}(0)|\lambda_{\alpha m}\rangle\frac{k^2}{k^2+\left(\lambda_{\alpha m}-\lambda_{\beta n}\right)^2}.\end{aligned} \tag{3.47}$$

A. Simplifying the infinite sum

Eq. 3.47 reveals a crucial detail of the contributions to Φ_{S}. The Lorentzian factor $k^2/k^2+\left(\lambda_{\alpha m}-\lambda_{\beta n}\right)^2$ suppresses terms in the double sum if the quasi-energy difference $|\lambda_{\alpha m}-\lambda_{\beta n}|$ is much larger than the recombination rate constant k. Looking again at Fig. 3.1, it is clear that, similar to Section 2.III, there is a separation of time scales between the RP decay and the fast oscillations of the spin dynamics. For long-lived RPs, the majority of terms in the double sum average to zero over the RP lifetime, leaving only terms coming from nearly degenerate subspaces in Floquet space to contribute; exactly the same subspaces formed when diagonalising H_{F} earlier.[72]

Now the advantage of our alternative form of the detection operator becomes clear. Provided $k \ll \omega$, we only need to consider off-diagonal terms from the near-degeneracies captured in each copy of $\tilde{H}_{\mathrm{F}}$. Thanks to the symmetry of our detection and initial density operators, the matrices corresponding to each copy of $\tilde{H}_{\mathrm{F}}$, $\tilde{A}_{\mathrm{F}}$ and $\tilde{\rho}_{\mathrm{F}}(0)$, are identical. To build these matrices, we simply insert the matrix elements from A_{F} and $\rho_{\mathrm{F}}(0)$ that correspond to the elements in $\tilde{H}_{\mathrm{F}}$.

Since the copies of $\tilde{H}_{\mathrm{F}}$ are all shifted by multiples of the identity, transforming a single copy of $\tilde{A}_{\mathrm{F}}$ and $\tilde{\rho}_{\mathrm{F}}(0)$ into the eigenbasis of $\tilde{H}_{\mathrm{F}}$ generates all the required matrices (the factor of $n\omega\mathbb{I}$ leaves the eigenvectors unchanged). Furthermore, because the expression for Φ_{S} only contains energy *differences*, and the sets of nearly-degnerate subspaces only differ by a shift in energy of $\tilde{H}_{\mathrm{F}}$, the contribution to Φ_{S} from each subspace is the same. There will be $2Q+1$ identical contributions to Φ_{S} from

the $2Q+1$ equivalent subspaces, cancelling with the normalisation in the detection operator, and all off-diagonal contributions to Φ_{S} between states in different subspaces are discarded. We can therefore reduce the infinite dimensional double sum in Eq. 3.47 to be over a single copy of the Hilbert space-sized nearly degenerate subspace constructed on perturbative diagonalisation of the Floquet Hamiltonian[72]

$$\Phi_{\mathrm{S}} \simeq \sum_{\alpha\beta=1}^{4Z} \left(\tilde{A}_{\mathrm{F}}\right)_{\alpha\beta} \left(\tilde{\rho}_{\mathrm{F}}(0)\right)_{\beta\alpha} \frac{k^2}{k^2 + \left(\tilde{E}_\alpha - \tilde{E}_\beta\right)^2}, \tag{3.48}$$

where $\tilde{A}_{\mathrm{F}}$ terms are without the factor of $1/(2Q+1)$ and the "energies" $\tilde{E}_\alpha$ are the eigenvalues of any copy of $\tilde{H}_{\mathrm{F}}$.

B. The algorithm

To summarise the results outlined above, the algorithm is implemented as follows[72]

1. Build the static Hamiltonian ($H^{(0)}$), Fourier components of the time-dependent Hamiltonian ($H^{(i)}$) and matrix respresentation of the singlet projection operator (P_{S}).

2. Diagonalise $H^{(0)}$ and transform all matrices to the eigenbasis.

3. Build $\tilde{H}_{\mathrm{F}}$ containing the $N-1$ nearest resonances/degeneracies based on the eigenvalues of $H^{(0)}$, the value of ω and the Fourier modes with non-zero $H^{(i)}$.

4. Build the corresponding detection ($\tilde{A}_{\mathrm{F}}$) and initial density ($\tilde{\rho}_{\mathrm{F}}(0)$) matrices by inserting the appropriate matrix elements from P_{S}.

5. Diagonalise $\tilde{H}_{\mathrm{F}}$ and transform $\tilde{A}_{\mathrm{F}}$ and $\tilde{\rho}_{\mathrm{F}}(0)$ in to the eigenbasis.

6. Evaluate the double sum in Eq. 3.48 to calculate the singlet yield.

As an illustrative example, consider a hypothetical 4-state system. Let us suppose that states 2 and 3 are approximately degenerate ($E_2 \simeq E_3$), in resonance with

state 1 when $n = 1$ ($E_{2/3} \simeq E_1 + \omega$) and state 4 when $n = 3$ ($E_{2/3} + 3\omega \simeq E_4$), meaning states 1 and 4 are in resonance when $n = 4$. The effective matrices built in steps 3 and 4 would be the following:

$$\tilde{H}_{\mathrm{F}} = \begin{pmatrix} E_1 + \omega & \left(H^{(1)}\right)_{12} & \left(H^{(1)}\right)_{13} & \left(H^{(4)}\right)_{14} \\ \left(H^{(-1)}\right)_{21} & E_2 & 0 & \left(H^{(3)}\right)_{24} \\ \left(H^{(-1)}\right)_{31} & 0 & E_3 & \left(H^{(3)}\right)_{34} \\ \left(H^{(-4)}\right)_{41} & \left(H^{(-3)}\right)_{42} & \left(H^{(-3)}\right)_{43} & E_4 - 3\omega \end{pmatrix}, \tag{3.49}$$

$$\tilde{A}_{\mathrm{F}} = \begin{pmatrix} (P_{\mathrm{S}})_{11} & 0 & 0 & 0 \\ 0 & (P_{\mathrm{S}})_{22} & (P_{\mathrm{S}})_{23} & 0 \\ 0 & (P_{\mathrm{S}})_{32} & (P_{\mathrm{S}})_{33} & 0 \\ 0 & 0 & 0 & (P_{\mathrm{S}})_{44} \end{pmatrix}, \tag{3.50}$$

$$\tilde{\rho}(0)_{\mathrm{F}} = \frac{1}{Z} \begin{pmatrix} (P_{\mathrm{S}})_{11} & (P_{\mathrm{S}})_{12} & (P_{\mathrm{S}})_{13} & (P_{\mathrm{S}})_{14} \\ (P_{\mathrm{S}})_{21} & (P_{\mathrm{S}})_{22} & (P_{\mathrm{S}})_{23} & (P_{\mathrm{S}})_{24} \\ (P_{\mathrm{S}})_{31} & (P_{\mathrm{S}})_{32} & (P_{\mathrm{S}})_{33} & (P_{\mathrm{S}})_{34} \\ (P_{\mathrm{S}})_{41} & (P_{\mathrm{S}})_{42} & (P_{\mathrm{S}})_{43} & (P_{\mathrm{S}})_{44} \end{pmatrix}. \tag{3.51}$$

These matrices are then transformed to the eigenbasis of $\tilde{H}_{\mathrm{F}}$, and the expression for Φ_{S} in Eq. 3.48 evaluated.

C. Approximations

Before testing and using this method to calculate Φ_{S}, it is useful to list the approximations made in the derivation of Eq. 3.48, so as to guide our application of the algorithm

- As diagonalisation of H_{F} relies on a perturbative approach, $\left|H^{(i)}\right| \ll \left|H^{(0)}\right|$ for all non-zero i.
- $\omega \gg \left|H^{(i)}\right|$ for non-zero i so that each copy of $\tilde{H}_{\mathrm{F}}$ (each degenerate subspace)

is energetically isolated from all others and can be treated separately.

- $k \ll \omega$ to ensure that only contributions to Φ_S from within our nearly-degenerate subspaces described by $\tilde{H}_F$ are non-negligible, and we do not need to include off-diagonal contributions between different subspaces.

- Given a Hilbert space dimension of N, only the closest $N-1$ resonances are guaranteed to be included in the perturbative diagonalisation of H_F. Therefore, particularly if there is a large number of Fourier components and a large number of states, we are potentially discarding important resonances caused by the time dependent field.

- Broadband noise magnetic fields are modelled as a "frequency comb" of equally spaced components, where ω is the frequency *spacing*. Multimode Floquet theory[75] could be used to expand the above method to include incommensurate base frequencies, which would be a better description of broadband noise. However, this generalisation would break down if $n'\omega_1 + m'\omega_2$ is close but not equal to zero, as the copy of $\tilde{H}_F$ for $\{n, m\} = \{n', m'\}$ will be close in energy to the $\{0, 0\}$ copy and so can no longer be treated as energetically isolated from one another. With very many frequencies and energy levels, this near degeneracy of blocks of the Floquet Hamiltonian becomes an unavoidable problem.

IV Testing the method

To validate the algorithm derived in this chapter, we compare calculations using this Floquet-based approximation with an exact time propagation method[61] for a small model RP for which time integration is not prohibitively expensive. The system has a single hydrogen nucleus in each radical with parallel axial hyperfine interaction tensors chosen to be representative of hyperfine interactions in organic radicals – they are based on the largest hyperfine tensors in the $FAD^{\bullet-}$ and $Trp^{\bullet+}$ radicals,[113] which

are also thought to be primarily responsible for the shape of the signal anisotropy in FAD-tryptophan RPs (see Chapter 4): $(A_{xx}, A_{yy}, A_{zz}) = (-0.0636, -0.0636, 1.0812)$ mT and $(-0.0989, -0.0989, 1.7569)$ mT. The central spike at $\theta = 90°$ is characteristic of RPs with hyperfine interactions of this form[74] and is discussed in detail in the next chapter.

As usual, we are interested in the variation of the singlet yield with direction of an external field.[177] We parameterise our static external field as

$$\mathbf{B}^{(0)} = 50\ \mu\text{T} \times (\hat{\mathbf{x}}\sin(\theta) + \hat{\mathbf{z}}\cos(\theta)), \tag{3.52}$$

where we vary θ (the axial hyperfine tensors mean Φ_{S} is independent of the azimuthal angle). We explore the regimes of recombination rate constant and perturbation strength for which our Floquet method is accurate.

A. Monochromatic field

First, we test the Floquet method in the presence of a single Fourier component. The time-dependent Hamiltonians are simple oscillating Zeeman terms for both electrons (Eq. 1.8)

$$\begin{aligned} \hat{H}_i^{(1)} e^{+\text{i}\omega t} &= -\gamma_i \hat{\mathbf{S}}_i \cdot \mathbf{B}^{(1)} e^{+\text{i}(\omega t+\delta)}, \\ \hat{H}_i^{(-1)} e^{+\text{i}\omega t} &= -\gamma_i \hat{\mathbf{S}}_i \cdot \mathbf{B}^{(1)} e^{-\text{i}(\omega t+\delta)}. \end{aligned} \tag{3.53}$$

We arbitrarily chose the frequency $\nu = \omega/2\pi = 2.0961$ MHz, which is resonant with an energy level transition near $\theta = 40°$ and $\theta = 140°$. The initial phase δ and direction $\hat{\mathbf{B}}^{(1)}$ of the RF field are chosen at random.

From the derivation above, we expect our method to become less accurate as the perturbation strength ($\left|\mathbf{B}^{(1)}\right|$) and/or recombination rate constant (k) are increased, and so we investigate the limit of applicability of this Floquet-based algorithm.

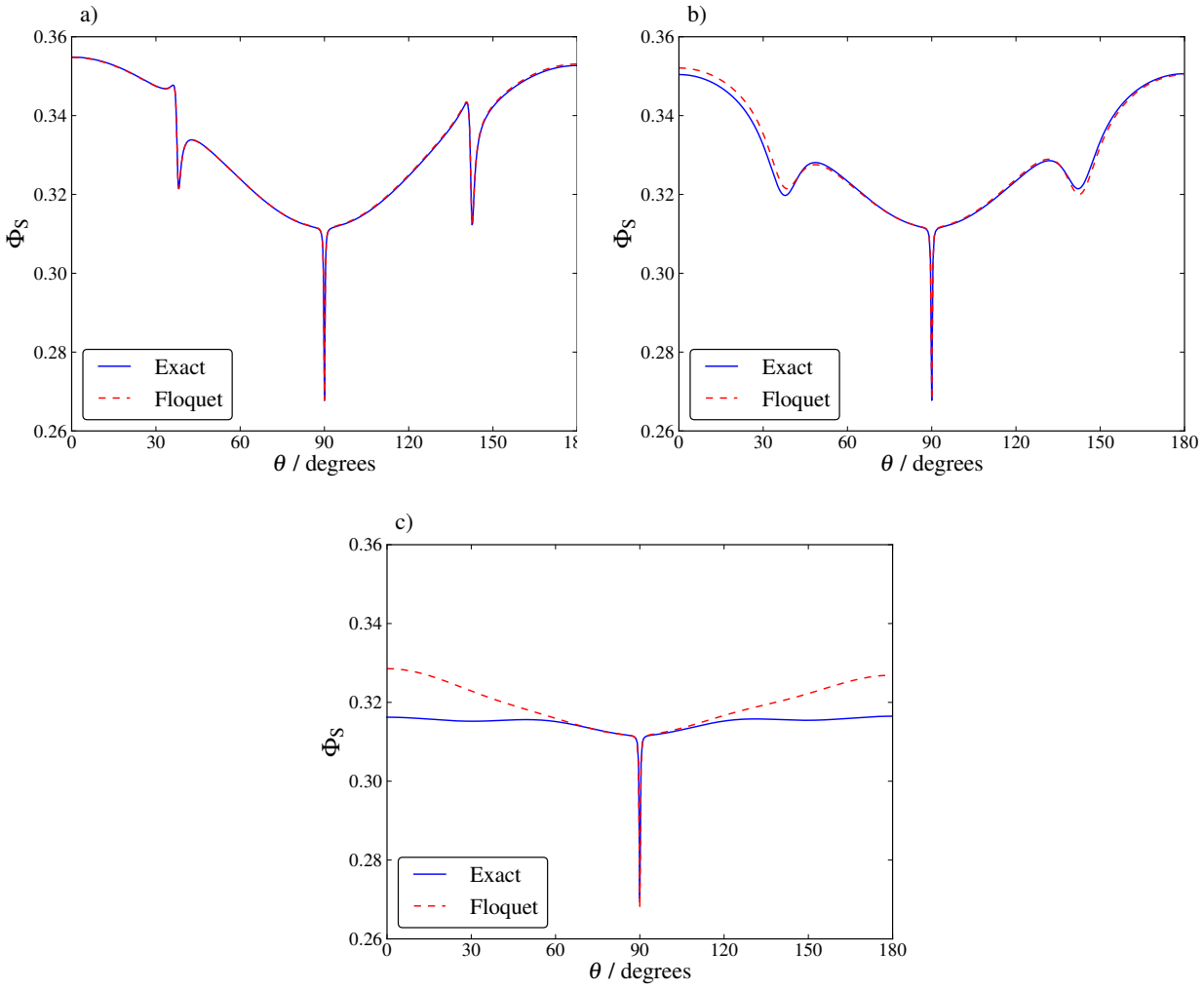


Figure 3.2: Comparing calculations of Φ_S using an exact time propagation method and our approximate Floquet-based algorithm for a RP in the presence of a monochromatic magnetic field ($\nu = \omega/2\pi = 2.0961$ MHz) with increasing RF field strength. a) $\left|\mathbf{B}^{(1)}\right| = 250$ nT, b) $\left|\mathbf{B}^{(1)}\right| = 2.5$ μT, c) $\left|\mathbf{B}^{(1)}\right| = 25$ μT. In all cases, the recombination rate constant $k = 10^4$ s^{-1}. Modified from Ref. 72.

Perturbation strength

Fig. 3.2 shows the effect of increasing $\left|\mathbf{B}^{(1)}\right|$ with a RP recombination rate constant $k = 10^4$ s^{-1}. Alongside the central sharp spike, there are additional features when the oscillating field comes into resonance with an energy level spacing. Unlike the spike at $\theta = 90°$, their shapes are not simply a negative Lorentzian, but are more complicated and depend on the initial phase and inclination of the RF magnetic field (the similarity of these features is discussed in Section 4.III).

First, when $\left|\mathbf{B}^{(1)}\right| = 250$ nT the Floquet method agrees to graphical accuracy with the exact result. As the strength of the perturbation increases first to 2.5 μT and then to 25 μT, the agreement is first less exact, and then breaks down entirely in the latter case. The resonant features in Φ_{S} broaden with increasing RF field strength, and this broadening is well captured for $\left|\mathbf{B}^{(1)}\right| = 2.5$ μT but not for $\left|\mathbf{B}^{(1)}\right| = 25$ μT. Perhaps this is not surprising as in the latter case the static field is only twice the strength of the RF magnetic field, meaning the time-dependent field can no longer be treated as a perturbation. Fortunately, we are not interested in the regime where the time-dependent and time-independent fields are of similar magnitude.

Radical Pair lifetime

Moving to a consideration of RP lifetime, Fig. 3.3 illustrates the accuracy of this method with decreasing RP lifetime, $\tau = 1/k$. Keeping $|\mathbf{B}^1| = 250$ nT, at which we know the approximations related to the magnitude of the perturbation are reasonable, we increase the RP recombination rate to $k = 10^5$ s^{-1} and $k = 10^6$ s^{-1}. This has the effect of decreasing the amplitudes of both the central spike and the resonant features until in the latter instance Φ_{S} is effectively featureless. The effect is almost quantitatively captured when $\tau = 10$ μs, but not for $\tau = 1$ μs. Again, we are fortunate that this parameter regime is not of interest, as there is in general no effect of the resonant RF field of this strength for $\tau < 10$ μs.

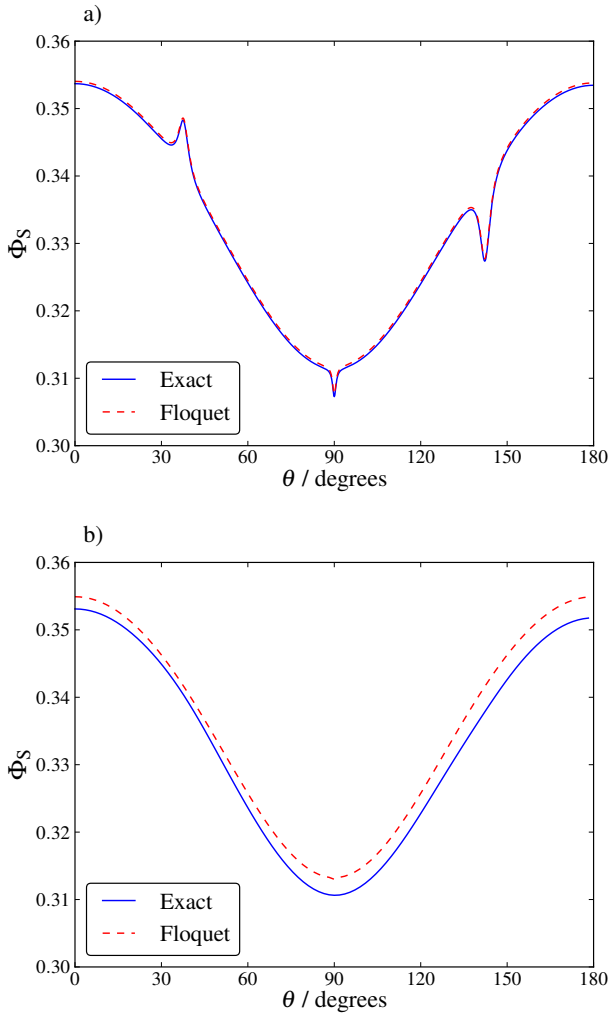


Figure 3.3: Comparing calculations of Φ_S using an exact time propagation method and our approximate Floquet-based algorithm for a RP in the presence of a monochromatic magnetic field ($\nu = \omega/2\pi = 2.0961$ MHz) with increasing recombination rate. a) $k = 10^5$ s^{-1}, b) $k = 10^6$ s^{-1}. In both cases, the perturbation strength $\left|\mathbf{B}^{(1)}\right| = 250$ nT. Modified from Ref. 72.

B. Broadband noise

Having validated this new method for monochromatic fields, we now move to a broadband RF magnetic field made up of equally spaced Fourier components. We use a base frequency of $\nu = \omega/2\pi = 15.9$ kHz and include all Fourier components with $|n|$ ranging from 100 and 2000, meaning band limits of 1.59 MHz and 31.8 MHz. For the 1901 components we randomly assigned the phase δ_n and inclination $\hat{\mathbf{B}}^{(n)}$ and the strength of each mode was set at $\left|\mathbf{B}^{(n)}\right| = 25$ nT. The RP lifetime was chosen as $\tau = 1$ ms.

Staying with our 2-nucleus RP, we see in Fig. 3.4(a) that again we have very good agreement between the Floquet and exact results, despite there being many more resonances, for this system (the Φ_{S} signal in the absence of an RF field is shown for reference).

We may be concerned that, for larger RPs and more energy levels, the prominence of multiple resonances and similar complications is not tested here. To test this, Fig. 3.4(b) shows the result of the same calculations for a RP containing an additional proton in each radical. In the first, the hyperfine tensor is

$$A_{12} = \begin{pmatrix} 0.9920 & 0.2091 & 0.2003 \\ 0.2091 & 0.2631 & +0.2803 \\ 0.2003 & +0.2803 & 0.5398 \end{pmatrix} \tag{3.54}$$

and in the second $(A_{xx}, A_{yy}, A_{zz}) = (-0.0190, -0.0190, 0.6046)$, both in mT. These are again based on nuclear hyperfine interactions in the FAD-tryptophan RP. Again the broadband RF superimposes a dense forest of resonant features on the reference signal. The Floquet method gives a good qualitative agreement with the exact calculation, though is no longer such a good agreement as for the 2-nucleus RP. However, given the random phases, inclinations and (in general) strengths of the various components of a broadband noise field, we consider a qualitative picture as perfectly acceptable. Therefore, we will proceed to use this new method in our discussion

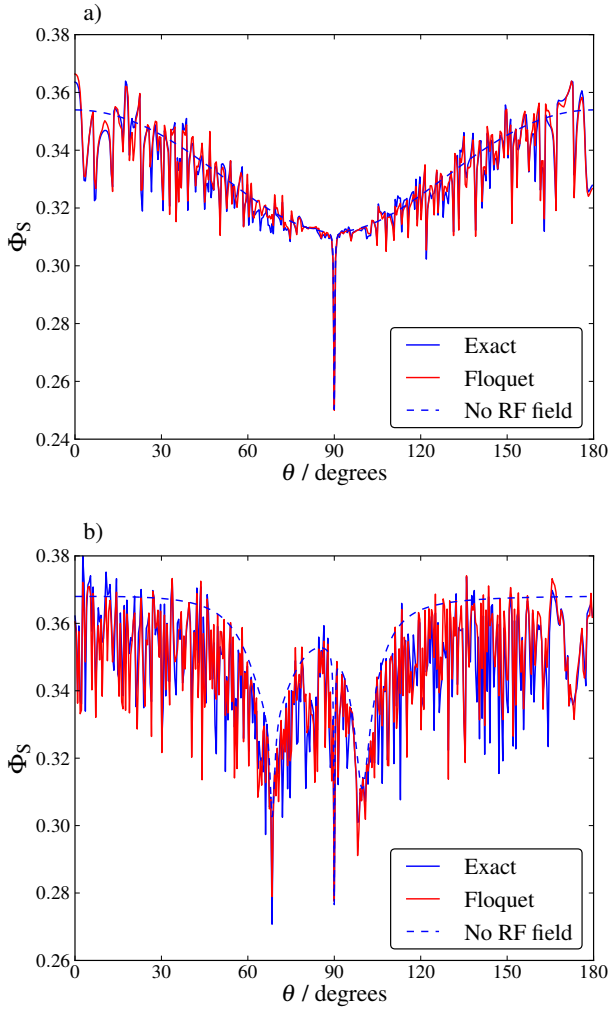


Figure 3.4: Comparing calculations of Φ_S using an exact time propagation method and our approximate Floquet-based algorithm for a RP in the presence of band-limited broadband RF magnetic noise. The band limits are 1.59 MHz and 31.8 MHz, and the frequency spacing is $\nu = \omega/2\pi = 15.9$ kHz. a) The 2-nucleus toy RP, b) the enlarged 4-nucleus RP. Modified from Ref. 72.

of the various experimental results in Chapter 5. To emphasise the advantage of this new method, the exact time propagation took five orders of magnitude more computer time than the Floquet algorithm.

V Phase average

As an aside, we have observed that there is one further advantage to using Eq. 3.25 as our propagator, one that is not utilised in this work. We have found that we can easily compute an expectation value with an average over t_0, or equivalently a phase average if the time-dependent field is monochromatic, a common feature in certain solid state NMR experiments.[54]

While we do not currently have a justification of the method below; a formal derivation requiring further work, we have noticed that simply altering the Floquet space operators can achieve this phase average. If we assume the initial density operator is independent of t_0 (denoted $\hat{\rho}(0)$ with t now being the time duration), we have found that using the following form of $\hat{\rho}_{\mathrm{F}}(0)$

$$\hat{\rho}_{\mathrm{F}}(0) = \sum_{\alpha\beta}\sum_{n} |\alpha, n\rangle\langle\alpha|\hat{\rho}(0)|\beta\rangle\langle\beta, n| \tag{3.55}$$

(with $\hat{A}_{\mathrm{F}}$ unchanged) allows us to compute the phase-averaged singlet yield directly by using this altered Floquet space operator in Eq. 3.48. The corresponding matrix representation is

$$\rho_{\mathrm{F}}(0) = \left(\begin{array}{c|c|c|c|c} \ldots & & & & \ldots \\ \hline & \rho(0) & 0 & 0 & \\ \hline & 0 & \rho(0) & 0 & \\ \hline & 0 & 0 & \rho(0) & \\ \hline \ldots & & & & \ldots \end{array}\right). \tag{3.56}$$

We calculated the singlet yield of the toy system with a single RF field using this form of the Floquet space density operator in the trace expression, and compared

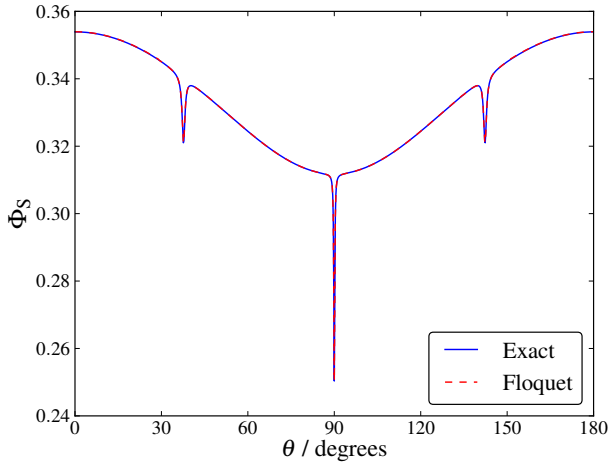


Figure 3.5: Comparing calculations of Φ_S using γ-COMPUTE and an altered Floquet-based algorithm for a RP in the presence of a monochromatic magnetic field ($\nu = \omega/2\pi = 2.0961$ MHz). $k = 10^3$ s^{-1} and $\left|\mathbf{B}^{(1)}\right| = 250$ nT.

this with the result calculated using the γ-COMPUTE algorithm.[38,121] The results are presented in Fig. 3.5 and verify that we have accurately computed the phase-averaged singlet yield. The apparent ease of averaging over t_0 means that this novel formulation of Floquet theory could have a broader application in NMR, where this averaging over t_0 is common.

VI Conclusions

In this chapter we have presented a powerful tool for exploring potentially important experimental results.[72] Our novel Floquet method allows us for the first time to simulate realistic, multinuclear radical pair spin systems under the influence of both monochromatic and broadband noise perturbations. Within our desired parameter range, we can accurately replicate exact results.

Unfortunately, there are a few limitations of this method. First, broadband noise is modelled as a comb of equally spaced frequency components, and therefore does not fully represent true noise. However, as we suppose that the primary effect of the

RF fields is through resonance effects, we hypothesise that inclusion of a range of frequencies demonstrates qualitatively the effect of multiple simultaneous resonant frequencies. Second, our method cannot be applied for very low frequency oscillating fields, which is both of interest given some previous experimental observations and, as we discuss in Chapter 5, potentially a method for probing the lifetime of the *in vivo* radical pair.

Acknoledgements

The important literature regarding the use of Floquet's Theorem in NMR[120,183] was suggested to me by Daniel Kattnig as a possible approach to the problem of simulating RPs in oscillatory magnetic fields. The extension of the method to modelling a broadband noise magnetic field as a comb of equally spaced frequencies, and the approximate diagonalisation of the Floquet Hamiltonian were both done in collaboration with David Manolopoulos.

Chapter 4

A Quantum Compass Needle?

While the principle of a directional magnetic sense being based on a RP reaction is well established in the literature[27,116,130,165,171,178,187] (see Chapter 1), there are a number of features of the *in vivo* mecahnism to be explored. One of the primary open questions in magnetoreception is the identity of the sensing RP. From a spin chemistry point of view, evidence for different RPs is often concerned with the absolute size of the anisotropy (or signal) found in computational studies of the RP.[4,19,21,32,56,114,159,224] Here, we explore instead something which has thus far received very little attention: the precision of the directional information available from a RP compass.[185]

I An accurate compass

There is significant evidence from the behavioural literature that the magnetic compass sense in migratory birds is highly accurate. For instance the bar-tailed godwit (*Limosa lapponica baueri*) is often given as an example of highly accurate navigation in the wild, as members of this species have been satellite-tracked migrating across the Pacific Ocean from Alaska to New Zealand in a single nonstop 11,000-km flight.[59] An error in bearing of just a few degrees would be fatal to these migrants. Cochran *et al.* found that free flying birds exposed to a rotated magnetic field prior

to release would maintain a rotated heading until their magnetic compass could be recalibrated at sunset the next day.[28] This suggests that the magnetic sense is the dominant orientation mechanism and that the accuracy of the bar-tailed godwit's migratory journey is in large part down to their magnetic compass sense.

While assigning the accuracy of navigation in free flight to a particular compass sense (magnetic, Sun or star) is impossible, Emlen funnel experiments[41] (discussed in Chapter 1) aim to remove other sources of directional information and can therefore test the acuity of the magnetic compass directly. Lefeldt *et al.* tested the limit of orientation of Eurasian blackcaps (*Sylvia atricapilla*) with the inclination angle of the magnetic field. If the inclination angle is 90°, the field is vertical and there is therefore no transverse directional information and so the birds are unable to orient. The authors found that their test birds were able to orient with an inclination angle of 85° but not 88°, meaning that the birds can detect the axis of the magnetic field lines with an accuracy better than 5°.[117]

This detection limit is corroborated by related studies which have tested the orientation of various species with horizontal and nearly horizontal external fields. Since the RP compass is an inclination and not a polarity compass (Chapter 1) an inclination angle of 0° means that north and south cannot be distinguished, and birds were found to be unable to orient in a horizontal field. However, with a 5° inclination angle, the birds were again able to orient in their appropriate migratory direction.[2]

It is perhaps surprising then that theoretical studies of a RP compass have previously found only slowly varying directional profiles[19,27,56,165,187] (similar to those in Fig. 4.1), from which deriving a highly accurate bearing seems unlikely. This can in large part be put down to the use of highly idealised radicals,[165,196] generally including only one or two nuclear spins, which fail to capture some features of larger spin systems. Of those studies which do model more realistic, multinuclear radical pairs,[19,27,116,187] none has explored the effect of varying the spin coherence lifetime

of the RP beyond about a microsecond; this being the approximate minimum lifetime required to capture an MFE in a 50 μT field[115,165] (as discussed in Chapter 1).

In this chapter, we examine cryptochrome-based RPs, including many nuclear hyperfine interactions and a broad range of recombination rates to explore the possibility of a more accurate RP compass.

II CRY-based compass needle

As introduced in Chapter 1, there are two well established hypotheses for the *in vivo* sensing RP: FAD-Z[77,186] and FAD-Trp.[130] Following Lee *et al.*,[116] we calculate the direction dependence of the fractional singlet yield, Φ_S, for multinuclear models of these two RPs and examine how this signal varies with different recombination rates. In these calculations we neglect spin relaxation mechanisms, meaning there is an implicit assumption that the spin coherence lifetime of the RP exceeds the reactive lifetime, τ. This simplification is discussed in Section 4.IV.

Initially, again after Lee *et al.*,[116] we include the 7 largest hyperfine interactions in $FAD^{\bullet-}$ and, where appropriate, the 7 largest in $Trp^{\bullet+}$ (and obviously none in the $Z^{\bullet}$ radical). The hyperfine interactions were calculated using density functional theory (DFT) and are given in Appendix A.

A. FAD-Z radical pair

Observing first the behaviour of the FAD-Z radical pair, Fig. 4.1 shows singlet yield profiles assuming a simple symmetric reaction scheme ($k_S = k_T = k$ in Fig. 1.1), for which we define the (reactive) lifetime $\tau = 1/k$. As the $Z^{\bullet}$ radical is hypothesised as being "magnetically isolated",[77] the model includes no exchange or dipolar interactions between the radicals. As in the previous chapter, θ defines the direction of the 50 μT external field relative to the z-axis of the flavin (Eq. 3.53).

The two curves show Φ_S for a short lifetime ($\tau = 1$ μs) and a long lifetime

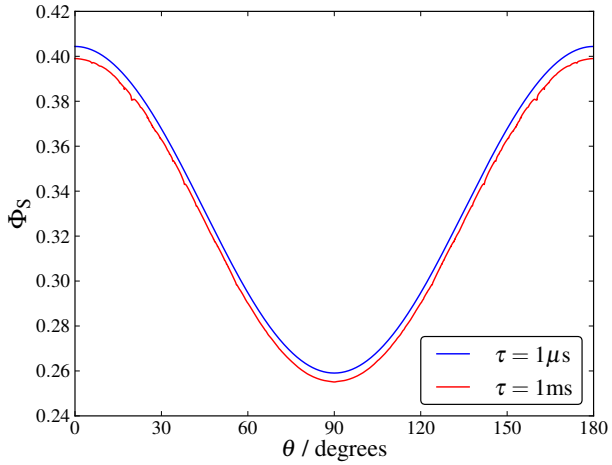


Figure 4.1: The fractional yield of singlet product (Φ_S) as a function of external field direction θ for the FAD-Z radical pair. The results are for a simple symmetric reaction scheme with two different values of rate constant $k = 10^3, 10^6$ s^{-1} ($= \tau^{-1}$).

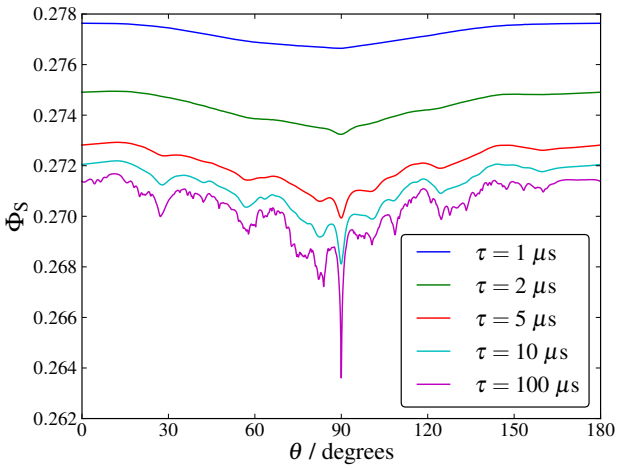
($\tau = 1$ ms). In both cases, we observe a slowly varying, approximately sinusoidal signal, similar to those pervading the existing literature.[56,77,168,186] This is a common feature of RPs with one of the radicals containing no spin-active nuclei. The singlet yield exhibits only a weak dependence on the recombination rate constant (when $k \leq 10^6$ s^{-1}) and it appears that, while offering a large overall signal, this RP is poorly suited to providing a highly accurate compass bearing.

B. FAD-Trp radical pair

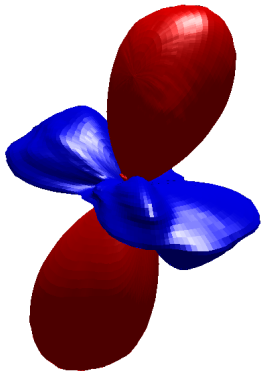
Moving to the FAD-Trp radical pair, we assume the same symmetric reaction scheme and the relative orientation of the two radicals is that of FAD and Trp-342 in *Drosophila melanogaster* cryptochrome[122,225] (Protein Data Bank ID code 4GU5). With the aim of simulating as large a spin system as possible, we neglect the dipolar and exchange couplings between the radicals. This simplification is discussed below. Singlet yield profiles for a range of values of τ are shown in Fig. 4.2(a).[74]

As expected, when the RP recombination is fast ($k = 10^6$ s^{-1}), we again observe a smoothly varying directional dependence, with a shallow minimum at $\theta = 90°$.[116]

(a)



(b)



(c)

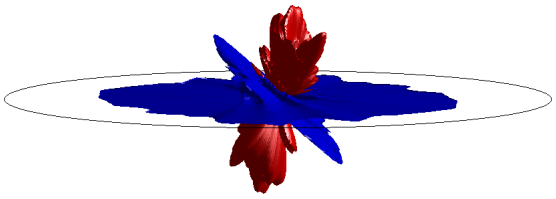


Figure 4.2: The fractional yield of singlet product (Φ_S) as a function of external field direction (a) θ and (b), (c) θ, ϕ for the FAD-Trp radical pair assuming a simple symmetric reaction scheme. In a) $\phi = 0°$ and the rate constant is varied: $k = 10^4, 10^5, 2 \times 10^5, 5 \times 10^5, 10^6$ s^{-1} $(= \tau^{-1})$. In (b) and (c) the average value $\langle \Phi_S \rangle$ has been subtracted with red and blue areas representing positive and negative values respectively. In (b), $\tau = 1$ μs. In (c) $\tau = 10$ μs and the black circle has been added as a guide to the eye. The data in (b) and (c) are plotted on different scales. Modified from Ref. 74

However, as the lifetime is increased, we see that Φ_S has increasingly many features and a prominent spike appears, which strengthens and narrows with decreasing k.[74] This feature is centered accurately at $\theta = 90°$ which corresponds to the external field lying in the plane of the flavin ring system.

Fig. 4.2(b) and Fig. 4.2(c) show the anisotropy in $\Phi_S(\theta, \phi)$ in terms of both the polar (θ) and azimuthal (ϕ) angles. By the anisotropy, we mean Φ_S minus the average singlet yield, $\langle\Phi_S\rangle$, over all values of θ and ϕ

$$\Delta\Phi_S(\theta, \phi) = \Phi_S(\theta, \phi) - \langle\Phi_S\rangle. \tag{4.1}$$

Red and blue in the figure denote positive and negative values of $\Delta\Phi_S(\theta, \phi)$ respectively. In Fig. 4.2(b) ($\tau = 1$ μs) we see that the slow variation in the singlet yield is mirrored in the low curvature of the lobes in $\Delta\Phi_S$. By contrast, for $\tau = 10$ μs (Fig. 4.2(c)) there is a thin equatorial disk, of which the spike is a cross section, which is prominent even for this moderate recombination rate.[74]

C. Larger spin systems

Utilising the methods presented in Chapter 2, it is possible to explore this spike feature further, and to test whether it is an artifact of the reduced 16-spin system we use or the symmetric reaction scheme we assume.

Fig. 4.3(a) shows how Φ_S varies with increasing the number of nuclear spins (N) included in the calculation.[74] In each case, the number of nuclei in the two radicals is equal, and the recombination rate constant $k = 10^3$ s^{-1}: we use such a slow recombination rate to maximise the efficiency of the algorithm[172] (by minimising the required number of frequency bins) outlined in Section 2.II. The spike survives in even significantly larger systems, though the absolute size of the anisotropy ($\max(\Phi_S) - \min(\Phi_S)$) decreases by approximately a factor of three from 1.16×10^{-2} for $N = 14$ to 4.01×10^{-3} for $N = 22$. However, the background variation flattens out with increasing N until the spike is more or less the only feature in the signal

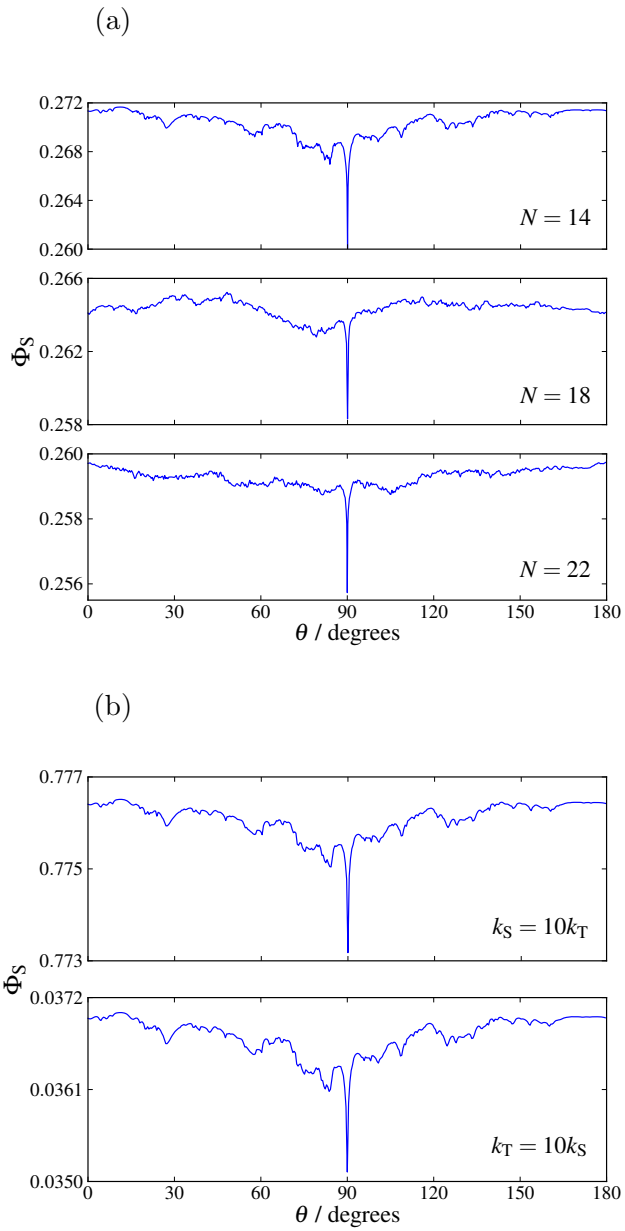


Figure 4.3: The fractional yield of singlet product (Φ_S) as a function of external field direction θ for the FAD-Trp radical pair. In (a) the number of nuclear spins included in the calculation (N) is varied and $\tau = 1$ ms. In b) $N = 14$ and the recombination is asymmetric with rate constants $k_S = 10^4$ s^{-1}, $k_T = 10^3$ s^{-1} ($k_S = 10k_T$) and $k_S = 10^3$ s^{-1}, $k_T = 10^4$ s^{-1} ($k_T = 10k_S$). Note the different scales on each of the axes.

for $N = 22$.

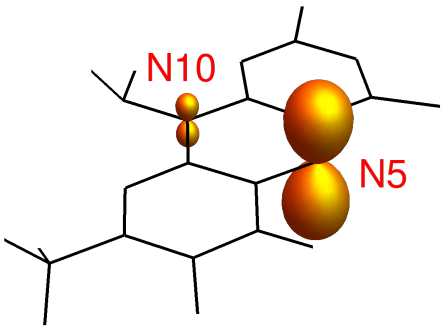
In Fig. 4.3(b) are the results of calculations in which k_S and k_T differ by an order of magnitude (details in figure caption) for $N = 14$. Here we again model very slow recombination to ensure that the recombination operator can be treated as a perturbation as required by our approximate algorithm outlined in Section 2.III. These results are used merely as a proof of principle. Clearly the spike is robust to this moderate asymmetry in the reaction scheme. As mentioned previously, it is reasoned that a large asymmetry in rate constants removes the direction dependence of the product yield,[94] as one recombination pathway dominates regardless of field direction, and so would be incompatible with a RP compass.

We therefore have this desirable, sharp, compass needle-like feature in our product yields for the FAD-Trp radical pair[74] that is seemingly robust to both asymmetry in the reaction scheme and increasing system size. While it may be intuitively apparent that this spike would give a better heading accuracy than the smooth profile available from FAD-Z, this idea is discussed in detail in Chapter 6. In the remainder of this chapter we discuss the origin of this feature and its potential relevance to the *in vivo* sensor.

III Origin of the spike in Φ_S

Looking at the hyperfine interactions in the flavin,[116] those for the nitrogens in the $FAD^{\bullet -}$ central ring (Fig. 4.4(a)) are approximately axially symmetric, aligned with the ring system, and therefore mirror to some extent the 3D anisotropy in Φ_S.[27] Since the spike feature occurs when the external field lies in the plane of the flavin ring system, these interactions are the primary candidates for the origin of this phenomenon. Looking at the principal values of their hyperfine tensors[116] – $(A_{xx}, A_{yy}, A_{zz}) = (0.087, 0.100, 1.757)$ mT for N5 and (0.014, 0.024, 0.605) mT for N10 – they share a large z component and small but non-zero transverse (x and y) components.

a)



b)

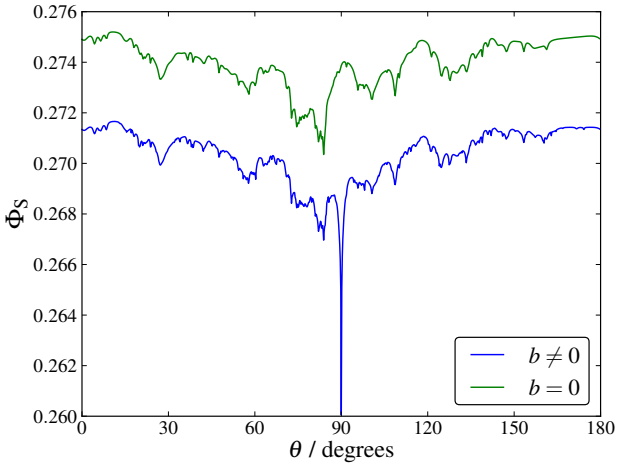


Figure 4.4: (a) Pictorial representations of the hyperfine interactions of the N5 and N10 nuclei in the $FAD^{\bullet-}$ radical. (b) The fractional yield of singlet product (Φ_S) as a function of external field direction θ for the FAD-Trp radical pair (blue) and the altered FAD′-Trp radical pair (green). $\tau = 100$ μs.

To test the dependence of the spike on these interactions, Fig. 4.4(b) compares the singlet yield results for the $N = 14$ FAD-Trp radical pair with an artificially altered FAD′-Trp radical pair, wherein the transverse components of N5 and N10 hyperfine tensors have been set to zero.[74] The labels denote the presence ($b \neq 0$) or absence ($b = 0$) of the coupling caused by these transverse hyperfine components as discussed below. In the latter signal, the strong feature at 90° has disappeared while the rest of the profile is approximately unchanged. Therefore we can conclude that the spike arises because of the special form of these hyperfine tensors. Below we analyse the the causal relation between these tensors and the shape of the singlet yield profile.

A. An avoided crossing

To explore this phenomenon, we return to the toy system we used in the previous chapter (Section 3.IV) which was based on hyperfine interactions which follow the special form of N5 and N10. We see in Fig. 3.4(a) that there is a spike feature in Φ_S even for this simple system, confirming that it is indeed these hyperfine interactions which give rise to the feature.

With this toy 2-proton RP, it is feasible to examine all 16 eigenstates. In doing so, we observe that there are avoided energy level crossings that coincide with the spike at 90° (Fig. 4.5). If the hyperfine tensors are altered as above (the transverse components set to zero), these become ordinary crossings and represent a symmetry of the system. With no transverse hyperfine components, the nuclear spin states are not mixed by the RP Hamiltonian, meaning we have non-interacting subspaces within the energy levels of the RP. When $\theta = 90°$, these subspaces become identical up to an inversion of all spins, meaning all states are doubly degenerate for this field direction. As the only remaining hyperfine term is the A_{zz} component, the nuclear spin states are not mixed by the Hamiltonian, and we therefore have two non-interacting subspaces which are degenerate at $\theta = 90°$ (Eq. 4.16) as the system

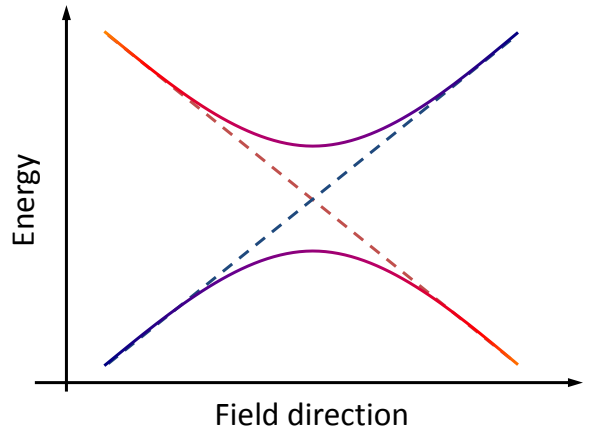


Figure 4.5: A schematic repressentation of an avoided crossing in the energy levels of the RP. If a hyperfine tensor has only $A_{zz} \neq 0$ ($b = 0$ in Eq. 4.3, dotted lines), when the external field is perpendicular to the unique axis, the energy levels of the RP will be in degenerate pairs because the system is symmetric with respect to inversion of all spins, and these two states are in separate non-interacting subspaces. With small transverse hyperfine components ($A_{xx}, A_{yy} \neq 0$, $b \neq 0$, solid lines), these states are mixed around the degeneracy, leading to an avoided crossing around $\theta = 90°$.

is symmetric with respect to inversion of all spins.

To explore the effect of an avoided crossing on the singlet yield, we want to describe how two states coupling near a degeneracy affects the contributions to Φ_S, and so we return to our expression[197] for Φ_S (Eq. 2.12)

$$\Phi_S = \frac{1}{Z} \sum_{nm}^{4Z} \left| \left(\hat{P}_S \right)_{nm} \right|^2 \frac{k^2}{k^2 + \omega_{nm}^2}. \tag{4.2}$$

Just considering contributions from the 2×2 sub-space of a pair of crossing states, we take the reference system to have $A_{xx} = A_{yy} = 0$ (the transverse hyperfine components are then included as a perturbation). We write the usual 2×2 matrix associated with avoided crossings[111]

$$\tilde{H} = \begin{pmatrix} aq & b \\ b & -aq \end{pmatrix}. \tag{4.3}$$

The energies of the reference states ($b = 0$) vary linearly with some variable q with gradient given by a, which is related to A_{zz}. When q goes through zero these states are degenerate, corresponding to $\theta = 90°$. The coupling interaction b corresponds to the $A_{xx} + A_{yy}$ matrix element which couples this pair of degenerate states and causes the avoided crossing. Diagonalising this effective Hamiltonian gives eigenvalues and eigenstates:

$$\epsilon_{\pm} = \pm\sqrt{a^2q^2 + b^2}, \tag{4.4}$$

$$\begin{aligned} |+\rangle &= \cos(\xi)|1\rangle + \sin(\xi)|2\rangle, \\ |-\rangle &= \sin(\xi)|1\rangle - \cos(\xi)|2\rangle, \end{aligned} \tag{4.5}$$

where

$$\tan(2\xi) = \frac{b}{aq}. \tag{4.6}$$

Assuming for simplicity that the off-diagonal matrix elements (in the reference eigenbasis) of the singlet projection operator are negligible, and that the primary effect comes from mixing two states with different "singlet character" p_1 and p_2, the corresponding projection operator is

$$P_{\mathrm{S}} = \begin{pmatrix} p_1 & 0 \\ 0 & p_2 \end{pmatrix}. \tag{4.7}$$

In the new eigenbasis, Eq. 4.5 (using transformation matrix U), this becomes

$$\begin{aligned} U^{\dagger}P_{\mathrm{S}}U &= \begin{pmatrix} \frac{1}{2}(p_1+p_2) + \frac{1}{2}(p_1-p_2)\cos(2\xi) & \frac{1}{2}(p_1-p_2)\sin(2\xi) \\ \frac{1}{2}(p_1-p_2)\sin(2\xi) & \frac{1}{2}(p_1+p_2) - \frac{1}{2}(p_1-p_2)\cos(2\xi) \end{pmatrix} \\ &= \begin{pmatrix} P^{\mathrm{S}}_{++} & P^{\mathrm{S}}_{+-} \\ P^{\mathrm{S}}_{-+} & P^{\mathrm{S}}_{--} \end{pmatrix}, \end{aligned} \tag{4.8}$$

where $P^S_{+-} = P^S_{-+}$. Substituting into our equation for Φ_S (Eq. 4.2) gives the contribution to the singlet yield from this pair of states.

$$\Phi_S(b) = \frac{1}{Z}\left[\left(P^S_{++}\right)^2 + \left(P^S_{--}\right)^2 + 2\left(P^S_{+-}\right)^2 \frac{k^2}{k^2 + 4(a^2q^2 + b^2)}\right]. \tag{4.9}$$

In order to compute the effect of the avoided crossing, we compare contributions to Φ_S with and without the coupling term b[74]

$$\Phi_S(b) - \Phi_S(0) = -\frac{2b^2(p_1 - p_2)^2}{Z\left(k^2 + 4(a^2q^2 + b^2)\right)}. \tag{4.10}$$

Now we can see that introducing the coupling b, or equivalently the small A_{xx} and A_{xy} hyperfine terms, leads to a negative Lorentzian (Eq. 4.10) centred at $q = 0$ with amplitude

$$\frac{2b^2(p_1 - p_2)^2}{Z\left(k^2 + 4b^2\right)} \tag{4.11}$$

and full width at half maximum height

$$\sqrt{\frac{4b^2 + k^2}{a^2}}. \tag{4.12}$$

We have therefore found the causal origin of the spike feature in the singlet yield for RPs which contain a special type of hyperfine interactions. Large A_{zz} and small (but importantly non-zero) A_{xx} and A_{yy} components lead to avoided crossings in the energy levels of the RP, which in turn leads to a spike in Φ_S. We can see from Eqs. 4.11 and 4.12 that the longer the RP lifetime (the smaller k), the stronger and narrower the spike, as we observed in Fig. 4.2. The absolute size of the effect is related to the difference in "singlet character" ($p_i = (P_S)_{ii}$) between the states which are mixed by the avoided crossing.

An important note is that there is no strict requirement on the absolute values of the hyperfine parameters. Therefore the spike should be robust to the inevitable inaccuracies involved in using DFT to calculate the hyperfine tensors,[205] assuming

that the *relative* axial and transverse components are qualitatively accurate. Indeed, measurements of the hyperfine components appear to support the conclusion from the DFT calculations that $A_{zz} \gg A_{xx}, A_{yy} \neq 0$ (see Table A.3 in Appendix A).

B. Requirements for the counter radical

One question this analysis raises is why the FAD-Z radical pair does not exhibit this behaviour (Fig. 4.1), given that it fulfills the criteria above (it also contains N5 and N10 in the flavin ring). There are indeed several instances where an avoided crossing in the energy levels of one radical does not give rise to a spike in Φ_{S} because of some special feature of the counter radical.

Looking at Eq. 4.10, this must mean that there is some symmetry in these systems which means that $p_1 = p_2$ when $b = 0$. As the radicals are non-interacting, a RP energy level is simply the product of a state from each radical. Assuming the crossing is in the energy levels of radical 1 (i.e. radical 1 has a hyperfine interaction of the special form described above), the combined states (ψ_i) will have the same state from radical 2 (ϕ_2) and the crossing states from radical 1 (ϕ_1 and ϕ_1'):

$$\begin{aligned} \psi_1 &= \phi_1(\text{electron 1})\phi_2(\text{electron 2}), \\ \psi_2 &= \phi_1'(\text{electron 1})\phi_2(\text{electron 2}). \end{aligned} \tag{4.13}$$

Setting $p_1 = p_2$ and some manipulation gives

$$\begin{aligned} 0 &= \langle\psi_1|\hat{P}^{\mathrm{S}}|\psi_1\rangle - \langle\psi_2|\hat{P}^{\mathrm{S}}|\psi_2\rangle \\ &= \left(\langle\phi_1|\hat{S}_{1x}|\phi_1\rangle - \langle\phi_1'|\hat{S}_{1x}|\phi_1'\rangle\right)\langle\phi_2|\hat{S}_{2x}|\phi_2\rangle \\ &+ \left(\langle\phi_1|\hat{S}_{1y}|\phi_1\rangle - \langle\phi_1'|\hat{S}_{1y}|\phi_1'\rangle\right)\langle\phi_2|\hat{S}_{2y}|\phi_2\rangle \\ &+ \left(\langle\phi_1|\hat{S}_{1z}|\phi_1\rangle - \langle\phi_1'|\hat{S}_{1z}|\phi_1'\rangle\right)\langle\phi_2|\hat{S}_{2z}|\phi_2\rangle. \end{aligned} \tag{4.14}$$

For the simplest one-nucleus model of radical 1, the Hamiltonian at $\theta = 90°$ is

$$\hat{H}_1 = \omega \hat{S}_{1x} + A_{zz} \hat{I}_z \hat{S}_{1z}. \tag{4.15}$$

The Hilbert space of radical 1 is reducible into (non-interacting) α_n and β_n subspaces as the nuclear spin states are not mixed by $\hat{H}_1$ – $\{|\alpha_e\alpha_n\rangle, |\beta_e\alpha_n\rangle\}$ and $\{|\alpha_e\beta_n\rangle, |\beta_e\beta_n\rangle\}$. In matrix form, the Hamiltonian is

$$\begin{pmatrix} \frac{1}{4}a & \frac{1}{2}\omega \\ \frac{1}{2}\omega & -\frac{1}{4}a \end{pmatrix} \oplus \begin{pmatrix} -\frac{1}{4}a & \frac{1}{2}\omega \\ \frac{1}{2}\omega & \frac{1}{4}a \end{pmatrix}. \tag{4.16}$$

The 2-dimensional eigendecompositions can be done analytically, and we can write the degenerate eigenstates

$$\begin{aligned} \phi_1 &= \cos(\xi)|\uparrow\uparrow\rangle + \sin(\xi)|\downarrow\uparrow\rangle, \\ \phi_1' &= \sin(\xi)|\uparrow\downarrow\rangle - \cos(\xi)|\downarrow\downarrow\rangle, \end{aligned} \tag{4.17}$$

where $\tan(2\xi) = 2\omega/a$. Evaluating the various spin operator matrix elements in Eq. 4.14 gives

$$\begin{aligned} \langle\phi_1|\hat{S}_{1x}|\phi_1\rangle &= \langle\phi_1'|\hat{S}_{1x}|\phi_1'\rangle = \frac{1}{2}\sin(2\xi), \\ \langle\phi_1|\hat{S}_{1y}|\phi_1\rangle &= \langle\phi_1'|\hat{S}_{1y}|\phi_1'\rangle = 0, \\ \langle\phi_1|\hat{S}_{1z}|\phi_1\rangle &= -\langle\phi_1'|\hat{S}_{1z}|\phi_1'\rangle = \frac{1}{2}\cos(2\xi), \end{aligned} \tag{4.18}$$

from which we can derive

$$\cos(2\xi)\langle\phi_2|\hat{S}_{2z}|\phi_2\rangle = 0. \tag{4.19}$$

Therefore, we require a non-zero expectation value of the z component of the electron spin in the eigenstates of the counter radical for a spike in Φ_S to arise from an avoided crossing in radical 1.[74] The matrix element in Eq. 4.19 will only be zero for special cases in which the interactions in the counter radical are symmetric w.r.t. inversion of the z axis. For instance, $\hat{H}_2 = \omega\hat{S}_{2x}$ (i.e. the $Z^\bullet$ radical) is a prime example,

hence why there is no spike in Φ_S for the FAD-Z radical pair.

C. Relation to resonances in Floquet space

As an interesting conceptual aside, we note the similarity between these avoided crossings and a resonance with an oscillating external field. As discussed in the previous chapter, an external time-dependent field being resonant with an energy gap is equivalent to a degeneracy in Floquet space.[72,182,183] The states are then mixed by the perturbation (taking the role of b above), leading to an avoided crossing in Floquet space and therefore a feature in Φ_S which is similar to the spike presented in this chapter. The shape of the resonant features is not purely Lorentzian because of the different off-diagonal elements in the Floquet space matrices $\rho_F(0)$ and A_F, and is also related to the initial phase of the oscillatory field.[72]

Importantly, we can use this insight to confirm our intuition that the magnitude of the effect of a resonance on Φ_S is related to the size of the coupling matrix element and the difference in "singlet character" (b and $(p_1 - p_2)$ respectively in Eq. 4.10) between the states involved. In the following chapter, we use this insight to contruct action-spectrum histograms[73] which give some qualitative measure of the effect of an external field oscillating at a given frequency.

IV Relevance to magnetoreception

While a RP compass could in theory result in a highly precise directional signal derived from a singlet yield profile which exhibits this spike feature, there are several considerations that should be taken into account when discussing its likely involvement in biological magnetic sensing.

First, the absolute size of the anisotropy is very small, even for the largest spikes we have observed. This has obvious implications[94] for the signal to noise ratio if there is a noisy signal due to low light levels (discussed in Chapter 6) or if there is

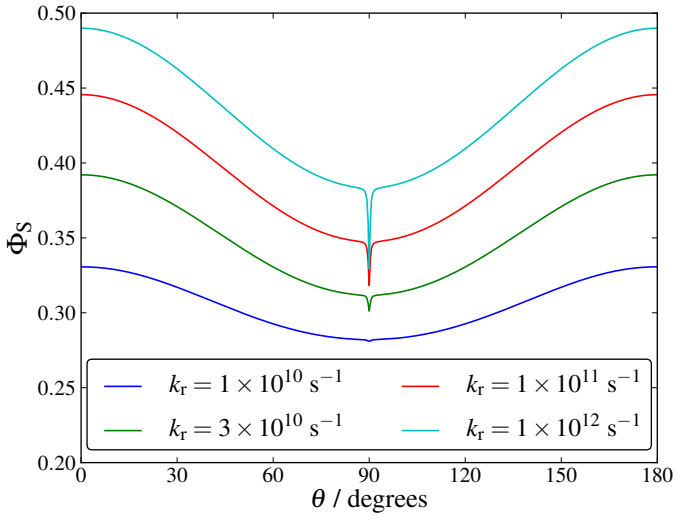


Figure 4.6: The fractional yield of singlet product (Φ_S) as a function of external field direction θ for a toy radical pair in the presence of 10° rotational jumps of one of the radicals. The rate constant of the rotational jumps k_r was varied. The recombination lifetime was chosen to be $\tau = 100$ μs. Data was calculated by Susannah Worster and is modified from Ref. 74.

noise in the signal transduction. Clearly, the FAD-Z radical pair, while not appearing to offer such angular precision, would offer a better signal to noise ratio given its large absolute anisotropy.[77]

Additionally, there is a question over whether the coherence lifetimes required for us to observe the spike are longer than feasible in the environment of the RPs *in vivo*. The primary reason for previous work being limited to lifetimes $\tau \leq 1$ μs is that it is generally accepted that this is roughly the limit of the spin coherence of a protein-based RP, given the efficiency of spin relaxation expected in such systems.[110,191,218] While it is beyond the scope of this work to calculate the effect of spin relaxation mechanisms on these systems, calculations involving librations of the radicals within their binding pockets found that if these motions are low amplitude and high frequency, the spin coherence times could indeed exceed 1μs and spikey singlet yield profiles could be observed (see Fig. 4.6, which is modified from the work of Susannah Worster presented in Ref. 74). However, further work based on

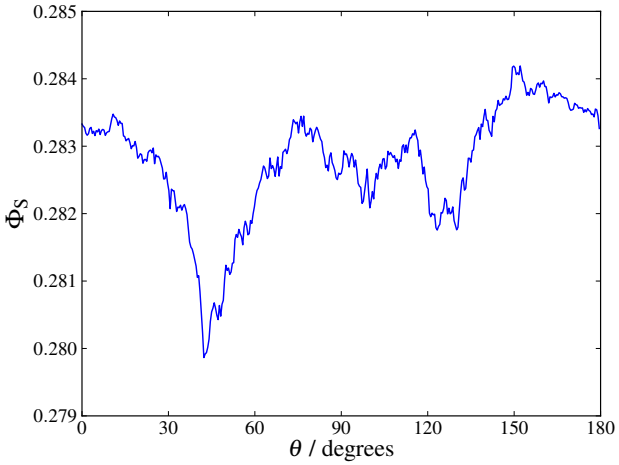


Figure 4.7: The fractional yield of singlet product (Φ_S) as a function of external field direction θ for the $N = 8$ FAD-Trp radical pair. $\tau = 1$ ms.

molecular dynamics (MD) simulations of the cryptochrome protein suggested that relaxation mechanisms in the CRY protein would rule out this spikey behaviour.[95] Additionally, another study found that electron spin relaxation could actually *amplify* the anisotropy of the singlet yield for a small model RP system,[96] meaning that the effect of spin decoherence could be difficult to predict.

Another important reservation is that these calculations have been performed neglecting exchange and dipolar couplings. With the aim of modelling the largest possible spin system, we have neglected interactions which are predicted to be an order of magnitude larger than the external field[39] for the FAD-Trp radical pair. While we cannot include these interactions in simulations of the $N \geq 14$ systems, we can model a simplified ($N = 8$) FAD-Trp radical pair including a dipolar coupling of $D = -407\mu$T as an illustration. D is estimated from the separation and relative orientation of the FAD-Trp radical pair in *Dm*CRY[39] (see Chapter 1), and the results are shown in Fig. 4.7. Evidently, including this extra interaction has broken the symmetry of the system and removed the central spike from the Φ_S signal.[73] Though we cannot verify that the spike does not reappear for larger spin systems, since the symmetry breaking would presumably still apply for larger N, it appears

that this is the major obstacle to this sort of behaviour in a biologically feasible RP.

V Conclusions and further work

We have seen that it is possible in principle for a RP compass sense to offer highly sensitive directional information. For the FAD-Trp radical pair, the signal profile can exhibit a sharp needle-like feature accurately centred at 90° that arises from an avoided crossing in the energy levels of the flavin spin system, due to the special form of the hyperfine interactions between the unpaired electron on the $FAD^{\bullet -}$ radical and the N5 and N10 nuclei in the central flavin ring system.[74]

This spike in the singlet yield has its origins in a fundamentally quantum mechanical effect, avoided crossings, and perhaps strengthens the case for biological magnetic sensing to be classed as true "quantum biology".[184] Indeed, the slow oscillations associated with these narrowly avoided crossings are something that is not captured using semiclassical methods.[123]

On the face of it, FAD-Trp seems well suited to exhibiting this behaviour. However, there are unfortunately a number of reservations that make it seem unlikely to be realised *in vivo*. Principally, this behaviour is not expected for systems in which there is significant radical-radical coupling, as is the case for FAD-Trp. Perhaps then, this system offers a proof of principle and there are other CRY-based RPs that could fulfill this requirement. However, if we suppose that the dipolar and exchange interactions have to at the very least be smaller than the external field to recover the spike in Φ_S, this would require a radical-radical separation of > 5 nm. On the normal length scale of RPs, this is exceptionally large (in *Dm*CRY, the flavin-tryptophan distance is 1.9 nm[122,225]). Importantly, for such well separated radicals the back electron transfer would be exceedingly slow (the rate decreasing approximately exponentially with radical-radical distance), and it has been argued that a RP compass could not be realised if one of the recombination pathways is too slow.[94]

Additionally, there is the problematic requirement that to observe a spike in Φ_S, the coherence lifetime of the RP be longer than otherwise thought feasible. This is a contentious issue (and is discussed in the next chapter), and remains one of the main unsolved features of this hypothesis. In Chapter 5, we present some possible experimental tests that would attempt to provide a bound on the lifetime *in vivo*.[73]

Acknowledgements

The discussion of results presented in this chapter was done in collaboration with Peter Hore as well as David Manolopoulos and Henrik Mouritsen. The analysis of the relationship between the spike feature and avoided crossings in the RP energy levels was developed together with Peter Hore and Daniel Kattnig. The calculations of Φ_S in the presence of radical librations were performed by Susannah Worster.

Chapter 5

Disrupting the avian compass

The concluding paragraph in the seminal work of Ritz *et al.* from 2004 begins[167] "Our study establishes the use of oscillating magnetic fields as a diagnostic tool that can indicate the involvement of a magneto-sensitive radical-pair reaction in birds." The claim is that their work offers a "killer experiment" for the RP mechansim of magnetoreception. Indeed, the authors suggest that experiments of this kind would provide proof for or against the involvement of a RP in the magnetic sense of the test animal.

One of the primary remaining challenges in the field of magnetoreception is to conclusively discriminate between a RP or magnetite[105] based magnetic sense. The majority of existing behavioural evidence and computational studies provides largely circumstantial evidence for the RP compass, but the disruption of the magnetic orientation behaviour of migratory birds by time-dependent magnetic fields[43,167,168,179] is thought to provide irrefutable evidence that the magnetic sense in these animals is based on a RP reaction.

The original study from Ritz *et al.*[167] used oscillatory magnetic fields in the 0.1-10 MHz (radio frequency, RF) range which were orders of magnitude weaker than the geomagnetic field (in the nT range). For comparison, one previous study suggested that, for a 7 MHz oscillating field (used in this study), a field strength of 285 μT would be required to produce a noticeable change in the alignment of a

magnetite particle.[100] Additionally, these RF fields are far from the expected ferromagnetic resonance frequencies which are in the GHz range,[102] and so it appears that the observed disorientation is not compatible with a magnetite magnetosensor. Conversely, the disruption of a RP-based compass by RF magnetic fields can be rationalised as a perturbation on the RP spin dynamics by resonance effects directly driving singlet-triplet interconversion. Indeed, the original work was designed using the "principles of magnetic resonance".[167] Importantly, in typical organic molecules, hyperfine interactions are generally in the 0.1-10 MHz range,[27] meaning we can expect energy level splittings, and therefore resonances, at these frequencies.

Despite the purported importance of these experimental findings, there remains some controversy around the results. In particular, the fact that such exceedingly weak RF magnetic fields could have a significant effect on a RP magnetic sensor implies an exceptionally long spin coherence lifetime of the RP, which is thought to be unattainable *in vivo*.[81,95,97,218] Additionally, there have been many behavioural studies following the initial work (see Table 5.1) testing different aspects of this RF effect, and there is a significant amount of conflicting data, casting doubt on the reproducibility of the original results.

One compounding obstacle to the importance of these studies is the fact that computational studies complementing the behavioural findings are severely hampered by the difficulty of the calculations, as discussed in Chapter 3. The exponential scaling of the spin Hilbert space, and lack of an algorithm capable of dealing with such large systems, means that previous studies had been limited to highly simplified RPs and generally a simple single-frequency oscillating field.[56,203,220] As has been observed previously, calculations of simplified RPs often cannot be extrapolated to larger RPs,[171] and so any conclusions made on the basis of such calculations can only be tentative. Using the approach outlined in Chapter 3,[72] we can perform spin dynamics calculations including a significant number of nuclei in the RP system in the presence of a single frequency or broadband noise RF magnetic field. In this

chapter we present the results of simulations of the two biologically relevant RPs: FAD-Trp and FAD-Z, proposed as being the magnetic sensing species *in vivo*.[73] We investigate the compatibility of the contrasting behavioural evidence with these two RPs, and discuss the feasibility of the parameter range necessitated by the sensitivity of a RP reaction to such weak time-dependent fields.

I Existing results

A. Behavioural studies

The original study by Ritz *et al.* found that both a single frequency 7 MHz oscillating field and a 0.1-10 MHz band limited noise magnetic field caused disorientation in their test animal, the European Robin.[167] Of the following studies, perhaps the most important is that of Ritz *et al.* from 2009, which found a special resonance at the electron "Larmor frequency" (ν_{L}), which corresponds to the frequency of precession of a free electron in the geomagnetic field.[168] Oscillating fields at this frequency (1.315 MHz in Frankfurt where the experiments were carried out) were found to cause disorientation at exceptionally low amplitudes, far lower than those required for single frequency fields at other, nearby frequencies ($0.5\nu_{\mathrm{L}}$ and $2\nu_{\mathrm{L}}$) to have a disorienting effect.

This observation has been interpreted[68,168] to mean that one of the radicals in the RP contains a "magnetically isolated" electron, i.e. an electron which is not hyperfine-coupled to any nuclei. When exposed to an external (static) magnetic field, the degenerate "up" and "down" electronic spin states in this radical split with an energy gap equal to the Larmor frequency (Eq. 1.9, Fig. 5.1A)

$$\nu_{\mathrm{L}} = \frac{\gamma_{\mathrm{e}} |\mathbf{B}_0|}{2\pi}, \tag{5.1}$$

Study	Test animal	Larmor frequency (ν_L)	Oriented RF condition	Disoriented RF condition
Ritz *et al.* 2004	European robin	1.315 MHz	7 MHz (B_1 = 470 nT) parallel to static field	7 MHz (B_1 = 470 nT) oriented 24° and 48° to static field, 0.1–10 MHz (B_1 = 85 nT)
Thalau *et al.* 2005	European robin	1.315 MHz	ν_L (B_1 = 485 nT) parallel to static field	ν_L (B_1 = 485 nT) oriented 24° to static field
Thalau *et al.* 2006	Ansell's mole rat	1.315 MHz	0.1-10 MHz (B_1 = 85 nT) and ν_L (B_1 = 4800 nT)	
Ritz *et al.* 2009	European robin	1.315 MHz and 2.63 MHz	$\nu = 0.5\nu_L$ and $2\nu_L$ (B_1 = 15 nT)	ν_L (B_1 = 15 nT) for static field strengths 47 µT, 94 µT
Keary *et al.* 2009	Zebra finch	1.204 MHz		1.156 MHz (B_1 = 470 nT) in 43 µT field
Vácha *et al.* 2009	American cockroach	1.2 MHz	7 MHz (B_1 = 44 nT)	ν_L (12 nT < B_1 < 18 nT); $2\nu_L$ (18 nT < B_1 < 44 nT)
Winklhofer *et al.* 2013	European robin	0.112 MHz		1.315 MHz (B_1 = 480 nT) in 4 µT field
Engels *et al.* 2014	European robin	1.363 MHz	Weak noise field control	20-450 kHz, 0.6-3 MHz, 2-9 MHz and background "electrosmog"
Kavokin *et al.* 2014	Garden warbler	1.4 MHz		ν_L (B_1 = 190 nT)
Wiltschko *et al.* 2015	European robin	1.315 MHz	No RF after pre-exposure to ν_L (B_1 = 15 nT)	7 MHz (B_1 = 480 nT) and ν_L (B_1 = 15 nT) after pre-exposure
Landler *et al.* 2015	Snapping turtle	1.43 MHz	Control group, ν_L (B_1 = 30-52 nT) after pre-exposure shifted orientation by 180°	Pre-exposed to RF and tested in absence of RF and vice versa. ν_L (B_1 = 30-52 nT)
Malkemper *et al.* 2015	Wood mouse	1.33 MHz	ν_L (B_1 = 785-1260 nT) same as control, 0.9-5.0 MHz (B_1 = 25-100 nT) shifted orientation by 90°	
Schwarze *et al.* 2016	European robin	1.363 MHz	ν_L (B_1 = 48 nT)	2 kHz–9 MHz
Pakhomov *et al.* 2017	Garden warbler	1.403 MHz	Control and ν_L (B_1 = 0.4 nT)	ν_L (B_1 = 2.4, 7, 20 nT)

Table 5.1: Summary of behavioural experiments. The Larmor frequency ν_L is given for the static field strength quoted in the study. The experimental conditions under which the animal could and could not magnetically orient are also shown. B_1 is the strength of the RF field quoted in the study, where B_1 is not given, the study provides an intensity spectrum. References are respectively: 167, 193, 192, 168, 99, 199, 217, 43, 98, 210, 112, 131, 179, 158. Modified from Ref. 73.

where $\gamma_e/2\pi = 0.028$ MHz/μT is the gyromagnetic ratio of an electron and $|\mathbf{B}_0|$ is the external field strength in μT. An RF field that drives the transition between these states would cause electron spin-flips in that radical, and hence have a very significant effect on singlet-triplet interconversion.

Further evidence from this study supports the hypothesis that the RP contains an isolated electron. Doubling the strength of the external field, which in turn doubles the energy gap between the electronic spin states, doubles the frequency of this special resonance.[168] Futhermore, there is no effect observed if the oscillatory field is parallel to the static field, which is commensurate with the fact that the coupling matrix element between states of an isolated electron would be zero by symmetry if the perturbation is parallel to the quantization axis.[68,193] A number of further studies have corroborated the disorienting effect of a Larmor frequency oscillating magnetic field,[98,199,210] though often these studies have not compared the effect of different magnetic conditions. In particular, many studies do not compare RF field conditions which do and do not impair the birds' ability to orient, which would in large part rule out experimental artifacts being the basis of the observed effect.

However, more recent experiments have cast doubt on these Larmor frequency findings. Engels *et al.* found that background electromagnetic noise was responsible for disrupting the orientation of birds in their experiments.[43] Importantly, an artifically introduced band-limited noise field caused disorientation regardless of whether the Larmor frequency was included in the frequency band. Yet another study, aimed at comparing the effects of broadband noise with single frequency fields, found that band-limited noise had a far more disorienting effect on the birds than the Larmor frequency field,[179] in direct contradiction with the majority of existing data. Indeed, the main contention of different behavioural findings is this distinction between single frequency and broadband noise effects (see Table 5.1 for a summary of the behavioural studies involving RF magnetic field conditions).

The disorienting effect of broadband noise magnetic fields points away from the

idea of a magnetically isolated electron, and towards a more general RP, in which both radicals contain many hyperfine-coupled nuclei. A hyperfine interaction splits the electron spin states, and the presence of many hyperfine interactions leads to a dense forest of energy levels in the RP (Fig. 5.1C). In this instance, no single frequency is expected to exhibit an especially strong resonance effect, as a resonance between any single pair of states will cause only a negligible perturbation. Instead, the simultaneous excitation of many resonances by a band-limited noise field would be expected to have a significantly greater effect on the RP spin dynamics.

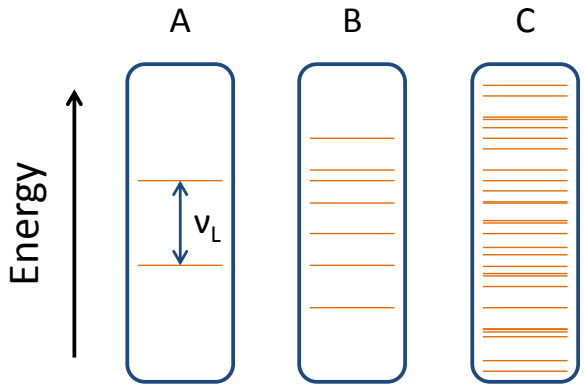


Figure 5.1: A pictorial representation of the energy levels in a radical containing different number of hyperfine interactions in a static Zeeman field. A, a radical with no hyperfine interactions, meaning the electron only experiences the external magnetic field, resulting in a Zeeman splitting with an energy difference equal to the Larmor frequency (Eq. 5.1). B, including a small number of hyperfine interactions, which splits the two electronic spin states into several energy levels with a variety of spacings. C, with a large number of hyperfine interactions, giving rise to many energy levels, which is representative of the majority of organic radicals. Modified from Ref. 73

B. Computational studies

A number of computational studies have explored the effect of a Larmor frequency perturbation on RPs containing a magnetically isolated electron,[56,167,203,220] and the consensus of these studies is that the anisotropy of the singlet yield signal is considerably reduced provided a sufficiently long spin-coherence. Here, "sufficiently

long" is defined by the approximate requirement[97] (similar to the reasoning used in Section 1.V)

$$\frac{\gamma_e B_1 \tau}{2\pi} \geq 1, \tag{5.2}$$

where B_1 is the intensity of the perturbation and τ is the lifetime (encompassing both reactive and coherence lifetimes). Similar to the Larmor frequency expression (Eq. 5.1), this relation states that, the time scale over which a field of strength B_1 has a significant effect on the spin dynamics of the RP is approximately the period of precession of an electron spin in that field. For example, for a 50 nT single frequency magnetic field, Eq. 5.2 suggests that a spin coherence lifetime of around 1 ms would be required to observe a significant perturbation to the singlet yield. A small number of studies[56] have also examined the effect of noise on various RPs, though in-depth study of these effects is severely limited by the computational challenge of the problem.

While the existing studies can offer useful conceptual insight, we now have the machinery to hand[72] to provide a more detailed investigation of these RF magnetic field effects on realistic RPs. In particular, previously only a small number (often 1) of hyperfine interactions have typically been included in calculations. Using simplified systems could lead to observation of effects which are merely artifacts of using a truncated spin system, as there would only be a small number of energy levels in these systems, for which a single resonance could have a significant effect. By contrast, in a realistic RP with many hyperfine-coupled nuclei and therefore a large number of energy levels, we would expect individual resonances to be of lesser importance.

As discussed in Chapter 1, the hypothesis that one of the radicals contains no spin-active nuclei ($Z^\bullet$) is still contentious.[77] The existence of such a radical is commonly questioned, as the requirement of a magnetically isolated electron is a stringent one, and severely limits the list of possible candidates to a small class of ideal molecules.[129,168] While a superoxide radical ($O_2^{\bullet -}$) does fulfill the requirements and

is commonly observed in biological systems, since the radical is expected to have strong spin-orbit coupling, a rapidly tumbling superoxide radical would undergo very efficient spin relaxation on the nanosecond timescale, ruling out even a static magnetic field effect.[77,89,90] If we suppose that the superoxide is therefore tightly complexed to an interaction partner so as to quench its orbital angular momentum and reduce its mobility, we might imagine this could introduce magnetic interactions with the surrounding nuclei.[77] Additionally, we require the radical-radical coupling terms to be vanishingly small, as otherwise these terms split the energy levels and break the symmetry of the system which gives rise to the special resonance. The superoxide would therefore have to be $>\sim$5 nm from the FAD radical anion for the dipolar and exchange interactions to be sufficiently small,[39] which is very large if the back electron transfer step is to occur on a reasonable timescale.[94]

II Results

A. Modelling the RF conditions

Before investigating these experimental findings, we need to define the various parameters we will use in our simulations, which will of course be influenced by the applicability of the Floquet algorithm[72] presented in Chapter 3. The RP reaction scheme will have symmetric recombination to distinct singlet and triplet products, with rate constant $k = 10^3$ s^{-1}. The static field strength used is 50 μT meaning the Larmor frequency (from Eq. 5.1) is 1.4 MHz. We use an amplitude of the single frequency magnetic fields of $B_1 = 5.0$ μT in all cases. To compare with broadband noise, we model the noise field as a "comb" of frequency components[72] spaced by 1 kHz with randomly assigned phases and directions of the different components, and amplitudes chosen to match the root-mean-square (RMS) amplitude of the single frequency fields. These were chosen at random in the range $-B_{1,\max}$ to $+B_{1,\max}$ where for example, with 10^4 components in a 10 MHz band, $B_{1,\max} = 86.6$ nT so

that the RMS amplitude of a component is 50 nT, and hence the total RMS intensity matches that of a single frequency component at 5 μT. These field strengths are stronger than were used in the experiments (see Table 5.1), but were chosen so that qualitative effects could easily be seen. Because of the relationship between the lifetime required for a field to cause a significant change in Φ_S and the RF field strength (Eq. 5.2), the lifetime we would require if we used the experimental field strengths would be even longer than the 1 ms used here, and as we neglect spin relaxation in these calculations, this is a serious drawback of the analysis presented in this chapter (and is discussed in detail below).

As a rough conceptual tool, we also introduce "action spectrum" histograms[73] to complement our singlet yield calculations. These are constructed by computing the eigendecomposition of the static Hamiltonian, and then finding all energy gaps which fall in given a frequency bin and summing their "resonance effects". This is defined by analogy with Fermi's Golden Rule from time-dependent perturbation theory, and is the product of the square modulus of the mixing matrix element and the difference in singlet character of the two states. The physical interpretation of these quantities is, respectively, the rate of the energy level transition, and an approximate measure of the effect of the resonance on driving singlet-triplet interconversion. The height of the n^{th} histogram bin, with bin width ω_0, energy gaps defined as $\omega_{ij} = E_i - E_j$ and a normalisation N so that the bin heights sum to unity, is

$$n^{\text{th}} \text{ bin height} = N \sum_{\substack{\omega_{ij} \in \\ \{n\omega_0 \pm \omega_0/2\}}} \left| \langle i | \hat{H}_\perp | j \rangle \right|^2 \left| \langle i | \hat{P}_S | i \rangle - \langle j | \hat{P}_S | j \rangle \right|. \tag{5.3}$$

$|i\rangle$ and $|j\rangle$ are eigenstates of the static Hamiltonian and $H_\perp$ is a Zeeman Hamiltonian perpendicular to the geomagnetic field. This expression was averaged over 100 orientations of the geomagnetic field so as to sample different static field orientations. The advantage of having this pictorial representation in frequency space is that we can easily identify special frequencies which would be expected to exhibit

particularly large effects on the singlet yield.

B. FAD-Z radical pair

The Larmor resonance

We first investigate the singlet yield of the FAD-Z radical pair,[116] including the 7 largest hyperfine interactions in the FAD radical, none in the Z radical, and in the absence of dipolar or exchange coupling (as in Section 4.II). As predicted, the action spectrum histogram (Fig. 5.2A) is dominated by the bin containing the Larmor frequency, arising from the unique resonance in the Z radical.[73] The resonances attributable to $FAD^{\bullet -}$ are spread over the whole 0-100 MHz, and are negligible compared to this Larmor frequency resonance.

These qualitative observations are borne out in the singlet yield calculations of this RP under different RF magnetic field conditions[73] (Fig. 5.2B). As presented in Fig. 4.1, the unperturbed signal is approximately sinusoidal[168] with a minimum at $\theta = 90°$. This relatively strong signal is completely abolished by a Larmor frequency RF field, whereas a field oscillating at double the Larmor frequency has a negligible effect on Φ_S. We choose the Larmor frequency field to be perpendicular to the static field; the size of the effect decreases to zero as the angle between the static and oscillating fields is decreased to zero, at which point the coupling matrix element vanishes[68,168] as stated above. Similarly, a broadband magnetic noise field causes a significant perturbation in Φ_S if the Larmor frequency component is within the band limits, whereas if it lies outside the band limits, the RF magnetic field has again a negligible effect. Indeed, with a broadband noise condition, the size of the effect on Φ_S is related to the parameters of the Larmor frequency component, and only very weakly dependent on the other frequency components.[73] Fig. 5.2C shows the singlet yield with a number of different realisations of the magnetic noise, and therefore different directions, phases and intensities of the Larmor frequency component. Clearly, these simulations confirm the idea that a FAD-Z RP is particularly

sensitive to oscillating fields at the Larmor frequency,[168] but directly contradict the findings of Engels *et al.* that a noise field causes disorientation in their test animals regardless of whether or not the Larmor frequency is included.[43]

For a finite RP lifetime and perturbation strength, the linewidth of this special resonance will potentially be of interest. This could be an important consideration when designing behavioural experiments, as there will be an envelope of frequencies around ν_{L} which will also, to some extent, excite this special resonance. There will be two source of line broadening,[73] from the RP lifetime with contribution $\sim 1/\pi\tau$ and from the strength of the RF field with contribution $\sim \gamma_{\mathrm{e}}B_1/2\pi$. As outlined above, we assume the parameter regime where $\gamma_{\mathrm{e}}B_1\tau/2\pi \geq 1$, meaning the B_1 term dominates the linewidth of the resonance. Fig. 5.2D shows how the resonance effect varies for monochromatic magnetic fields which are multiples of $\gamma_{\mathrm{e}}B_1/2\pi$ away from the Larmor frequency, and confirms that the attenuation of the signal anisotropy quickly falls off when the offset is more than $\gamma_{\mathrm{e}}B_1/2\pi$. One of the implications of this is that the magnetic "intensity" quoted for a Larmor frequency magnetic field in an experimental study should be the integrated amplitude of the field strength in the envelope $\nu_{\mathrm{L}} \pm \gamma_{\mathrm{e}}B_1/2\pi$, as all of the components in this range will contribute to the resonance effect, and so to only measure the intensity at exactly ν_{L} would give a misleading result.

Breaking the symmetry

We argued above that the existence of a truly magnetically isolated electron in the Z radical is contentious. There are a number of possible magnetic interactions the electron could experience,[77] and so in order to test the effect of these interactions on the Larmor resonance we choose to include just one of these: a dipolar coupling between the electron spins in $\mathrm{FAD}^{\bullet-}$ and $\mathrm{Z}^{\bullet}$. With no idea of the realisation of an FAD-Z radical pair *in vivo*, we arbitrarily choose the dipolar coupling appropriate for the FAD and Trp radicals in CRY. As outlined in Chapter 1, the dipolar interaction

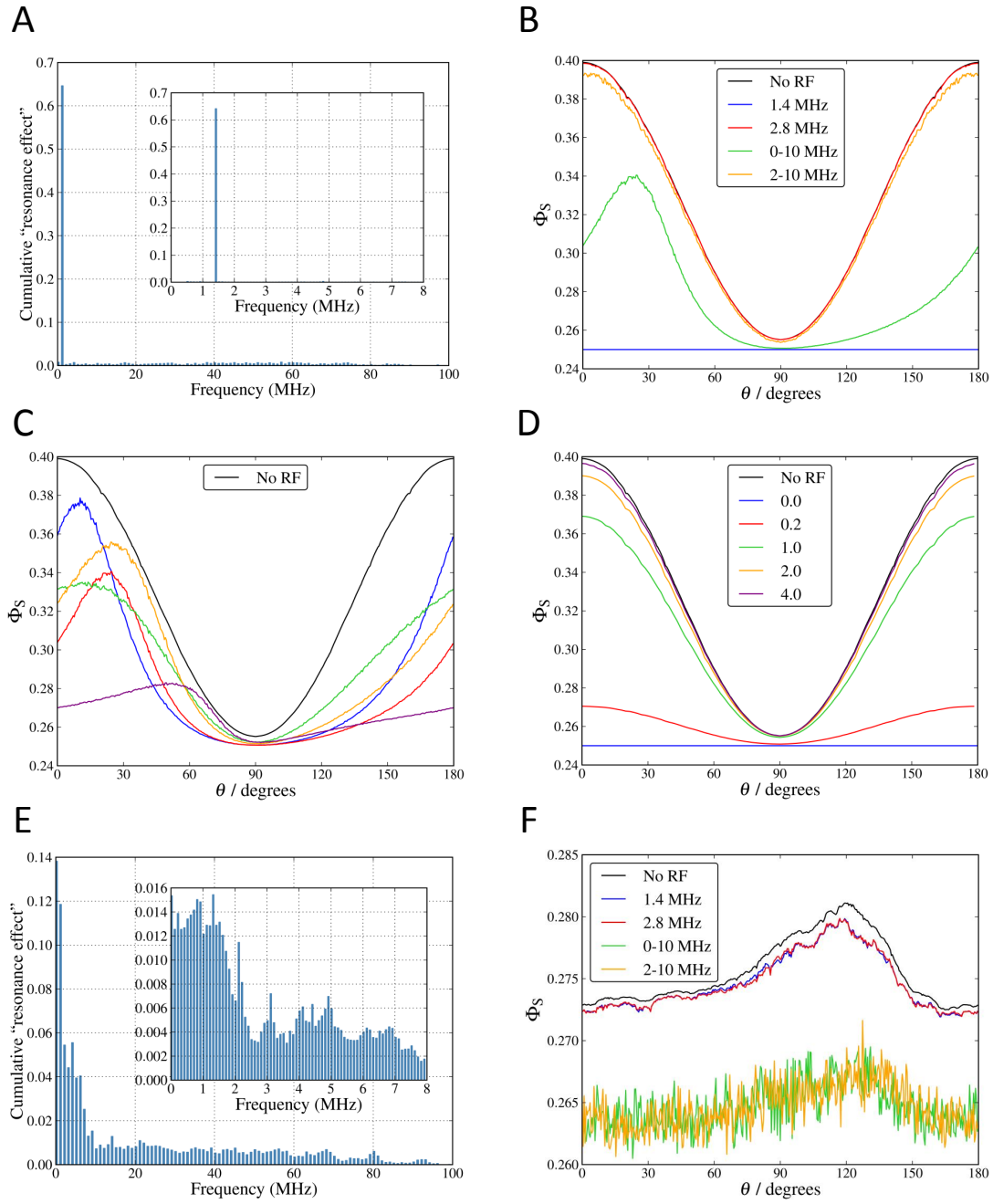


Figure 5.2: FAD-Z radical pair results. A-D, with no dipolar interaction. E-F, with a dipolar coupling, $D = -407$ μT. A, the action spectrum histogram in the range 0-100 MHz (bin width 1 MHz) with the 0-8 MHz expanded in the inset (bin width 0.1 MHz). B, the anisotropic singlet yield $\Phi_S(\theta)$ in the presence of different RF magnetic field conditions. C, testing the dependence of the perturbed signal on the randomly selected parameters defining a 0-10 MHz broadband noise field (see Section 5.II.A). The unperturbed signal is shown in black, and is compared with the singlet yield under five different realisations of the broadband noise field. D, the singlet yield with an applied single frequency field at an offset from the Larmor frequency (1.4 MHz) in multiples of $\gamma_e B_1/2\pi$. E, the action spectrum histogram as in A (including a dipolar interaction). F, the singlet yield for the dipolar coupled FAD-Z system with different magnetic field conditions as in B. Modified from Ref. 73.

takes the form[45]

$$D(r) = -\frac{3}{2}\frac{\mu_0}{4\pi}\frac{\gamma_e^2\hbar^2}{r^3} \tag{5.4}$$

for a radical-radical separation r. In *Dm*CRY, $r = 1.9$ nm[122,225] meaning the dipolar coupling parameter $D = -407$ μT.

When we include this interaction term, we can see that the Larmor frequency resonance in the action spectrum histogram (Fig. 5.2E) has now been spread out into the surrounding frequency bins. In breaking the symmetry of the system, we have broadened the Larmor resonance over the 0-10 MHz range. This is mirrored by the singlet yield calculations shown in Fig. 5.2F, where now the single frequency magnetic fields at ν_L and $2\nu_L$ have a similarly small qualitative effect on Φ_S, which is much less significant that the effect of both the 0-10 MHz and 2-10 MHz broadband noise fields.[73] Now that the special resonance has been removed, it appears that the simultaneous resonances arising from the 10^4 frequencies in the noise have a much greater effect on the spin dynamics than a single, albeit stronger, single frequency magnetic field. This directly contradicts the findings of Ritz *et al.* as well as a number of other studies,[98,168] but the fact that inclusion of ν_L in the broadband noise is not necessary to observe a significant effect is compatible with the study of Engels *et al.*[43]

One could argue that the size of the dipolar coupling we have used here is larger than would be expected *in vivo*. However, if we require the back electron transfer to occur on a reasonable time scale, the radicals should not be much more than 2 nm apart.[94] If we put this reservation aside for now, and consider a hypothetical RP with a small dipolar interaction, it would be possible to probe the size of the local magnetic interactions (including the dipolar coupling) with the linewidth of the Larmor resonance. As we have seen, the dipolar coupling broadens the Larmor resonance, and so if there are small but non-zero magnetic interactions experienced by the Z radical, they could be quantified by the width of the Larmor resonance if, for simplicity we assume that the linewidth is given by the size of the interaction

(which is greater than the broadening caused by B_1). For instance, Ritz *et al.* put an upper limit of $0.5\nu_L$ on this linewidth,[167] which would imply an interaction strength of 25 μT, and therefore a radical-radical separation of >4.8 nm if this were solely due to a dipolar coupling.

C. FAD-Trp radical pair

Disrupting the compass needle

We now move on to investigating the effect of these RF magnetic fields on the FAD-Trp RP. We include the seven largest hyperfine interactions in the tryptophan radical, as well as the seven in FAD,[116] as in the previous chapter. To begin with, we neglect any dipolar or exchange couplings so as to observe the effect of these RF fields on the "compass needle" introduced in Section 4.II.[74]

The action spectrum histogram (Fig. 5.3A) shows that, as expected, no single frequency stands out as giving a uniquely strong resonance effect. Instead, there is a roughly uniform distribution of bar heights from 0 to ∼80 MHz, where the bar heights tail off, presumably as there are fewer transitions at these higher frequencies.[73] As for the dipolar-coupled FAD-Z radical pair, we would expect this to mean that broadband noise anywhere from 0-80 MHz to have a roughly similar effect on the singlet yield signal, which would be more pronounced than the effect of any single frequency.

This is indeed the case, as shown in Fig. 5.3B, as both ν_L and $2\nu_L$ perturbations lead to negligible changes to Φ_S, whereas a 0-10 MHz noise field has a significantly greater effect on the signal. Not only this, but a 70-80 MHz field also has a qualitatively similar effect on Φ_S as the band at lower frequencies, which could be used to design new experiments (see below).[73] As noted previously, the unperturbed signal has this very sharp "needle" feature,[74] but it appears that for all of these RF conditions, this spike is simply shifted, and the anisotropy of the signal is not significantly reduced. Perhaps it is naïve to assume that perturbation of the magnetic compass

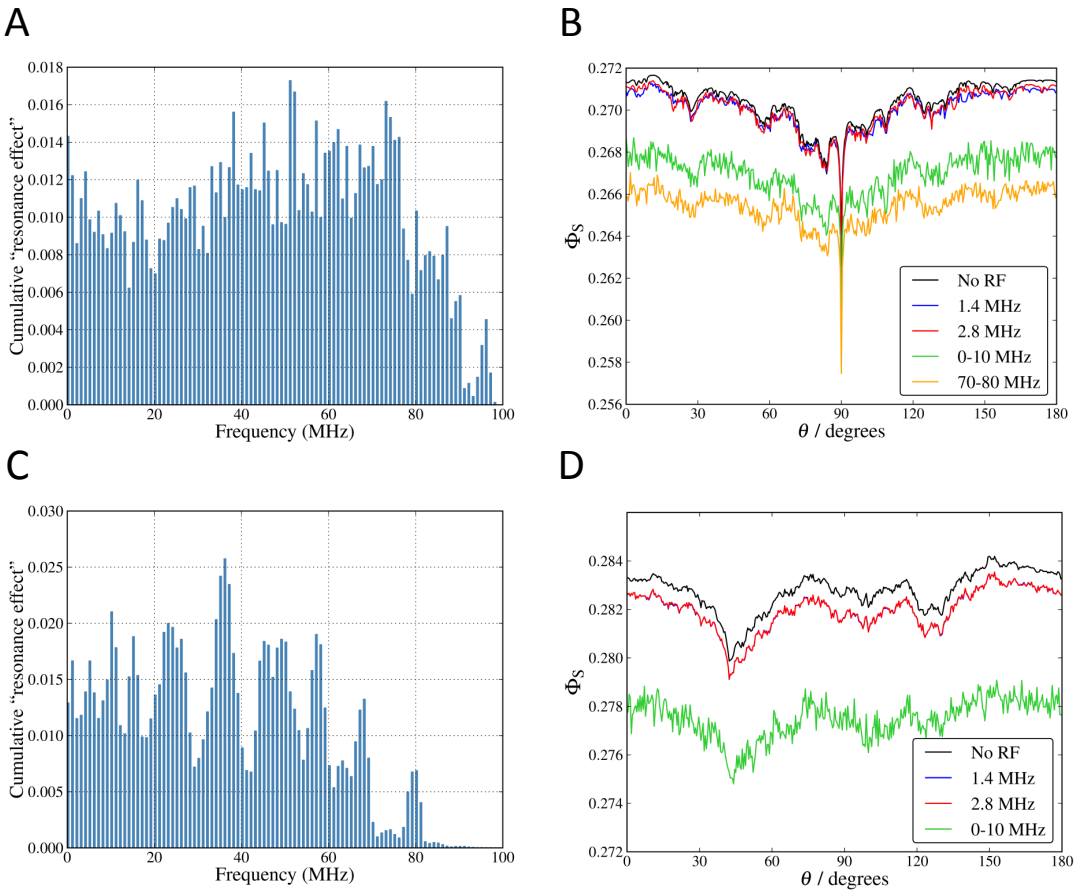


Figure 5.3: FAD-Trp radical pair results. A-B, with no dipolar interaction. C-D, with a dipolar coupling, $D = -407$ μT. A, the action spectrum histogram for the 16-spin FAD-Trp spin system in the range 0-100 MHz (bin widths 1 MHz). B, the anisotropic singlet yield $\Phi_S(\theta)$ in the presence of different RF magnetic field conditions. C, the action spectrum histogram as in A (including a dipolar interaction). D, the singlet yield for the dipolar coupled FAD-Trp system with different magnetic field conditions as in B. Modified from Ref. 73.

sense requires a significant change in the anisotropy, and effects of this type would be sufficient, though it is difficult to imagine how a sensor which is thought to use relative measurements would be disrupted by this effect.

A more general RP

As for the FAD-Z RP, there are serious reservations about the idea of the compass needle being realised *in vivo*, not least the fact that we have neglected dipolar coupling in these calculations. While we cannot include a dipolar interaction in a 16-spin

simulation, we can use a simplified RP with just 4 hyperfine interactions included in each radical, complete with the dipolar coupling used above, $D = -407$ μT. As is clear from Fig. 5.3D and was shown previously in Fig. 4.7, inclusion of this interaction abolishes the spike in Φ_S. We use this system as a model for any general RP with many nuclei in both radicals, as we expect any conclusions taken from this system to be more broadly applicable.

The action spectrum histogram is given in Fig. 5.3C shows again a broadly uniform distribution of bin heights, perhaps with more structure than the full FAD-Trp system in Fig. 5.3A, though we can confidently presume that this is an artifact of the reduced system, and assume that the bin heights would flatten out on the inclusion of more spins. Again, the singlet yield calculations (Fig. 5.3D) complement the histogram and we see that there is the same qualitative difference between the size of the effect of single frequency and broadband noise magnetic fields.[73]

III Relation to experiment

As discussed in detail in the next chapter, our analysis of singlet yield signals is severely hampered by the current level of ignorance about the signalling pathway involved in magnetoreception, and how $\Phi_S(\theta)$ is perceived by the bird. For example, as stated above, no RF condition significantly affects the anisotropy of the singlet yield for the FAD-Trp compass needle system and so it may appear that none of the RF condition shown would be expected to cause disorientation. However, we believe it to be somewhat naïve to assume that the anisotropy must be largely abolished for an experimental condition to disrupt the operation of a RP compass. Perhaps the variation over time of the parameters of a broadband noise magnetic field could introduce a degree of noise into the RP signal, thereby decreasing the accuracy of the RP compass as discussed in the next chapter. Indeed, there is evidence that both snapping turtles[112] and wood mice[131] change their orientation when subject to an RF field (see Table 5.1), rather than being simply disorientated, meaning perhaps there

is a more complex explanation of the effect than previously thought. Therefore, we consider only qualitative differences between single frequency and broadband noise perturbations, much as the various experimental studies do, in our comparison of our results to the behavioural findings.

A. Unrealistic parameters?

The first and most important point relates to the RP lifetime used in the calculations above. In choosing the strength of the monochromatic RF fields to be 5 μT, we have used field strengths that are significantly larger than those used in the experimental studies. In many studies, the Larmor frequency resonance has been observed for field strengths in the tens of nanotesla range.[98,168,199] Similarly, our RMS-matched broadband noise fields had a RMS noise density of

$$\frac{5\ \mu\mathrm{T}}{\sqrt{2}\sqrt{10\ \mathrm{MHZ}}} = 1.12\ \mathrm{nT\ Hz^{-1/2}}. \tag{5.5}$$

By constrast, Schwarze *et al.* reported disorientation by a $\sim$ 1 pT $\mathrm{Hz}^{-1/2}$ noise field.[179] Therefore, we have used field strengths that may be as much as three orders of magnitude larger than those used in the experiments.

This relates to the RP lifetime as we use $\gamma_\mathrm{e} B_1 \tau / 2\pi \geq 1$ (Eq. 5.2) as a rough guide for the RP recombination rate to use in order to observe appreciable effects of the RF fields on the spin dynamics. For the field strengths used above, this meant using a recombination lifetime of 1 ms. Since we neglect to include any spin relaxation in our calculations, this means that the effective spin coherence lifetime in these calculations is also $\gtrsim$ 1 ms. If we were to assume the same requirement (Eq. 5.2) on the lifetime for the experimental field strengths, this would appear to necessitate a spin coherence lifetime of orders of magnitude longer than this. As discussed in the previous chapter, molecular dynamics simulations suggest that the coherence lifetime is closer to 1 μs than to 1 ms.[95,97,218] If we were to assume realistic spin coherence and recombination lifetimes of the RP, we would find that

in the experimental conditions $\gamma_e B_1 \tau / 2\pi \ll 1$, meaning that we would expect there to be a vanishingly small effect of the RF magnetic fields on the RP yield (which is indeed found in simulations using more realistic parameters).

Therefore, the immediate conclusion is that the calculations of the sort in this chapter cannot explain any of the reported RF field effects. Instead, one of the following controversial conclusions must be true

- The birds are in fact exceptionally sensitive to tiny variations in the external magnetic field, meaning the requirement that $\gamma_e B_1 \tau / 2\pi \geq 1$ must be wrong. This seems unlikely given that the geomagnetic field naturally varies in intensity by 25-50 nT every day.[29]

- The spin coherence lifetime of the RP is much greater than previously thought. In molecular terms, it seems exceedingly unlikely that the spin coherence could be preserved for many milliseconds,[95,218] as this puts a severe constraint on the motions in the protein, which is implausible under normal biological conditions.

- The current model of RP magnetoreception is incomplete and we are missing some crucial piece of the mechanism which renders the sensor sensitive to these weak fields. Perhaps the external magnetic field is somehow amplified, meaning the fields experienced by the RP are much larger than those measured in the lab.

- The magnetic or electric components of the RF fields interacts with the magnetosensing mechanism (be it RP-based or otherwise) in some unknown way other than a direct effect on the RP to cause disorientation. We cannot provide any plausible mechanism for this.

- There is a systematic problem with the experimental paradigm which is introducing an artifact into all the behavioural studies, and this is the origin of the observed effect.

It is beyond the scope of this work to discuss any of these possibilities in detail, and so we instead discuss the above results with this knowledge that we are in a seemingly unphysical parameter regime as a strong caveat to our analysis, assuming that the disorientation of birds exposed to these weak RF fields really is a resonance effect on the singlet-triplet interconversion in the RP.

B. Discriminating between RPs

The primary conclusion we can make from our results is that, for all but the (uncoupled) FAD-Z radical pair, broadband noise magnetic fields have a qualitatively larger effect on the singlet yield than single frequency RF fields.[73] By contrast, the idealised FAD-Z radical pair exhibits the predicted special resonance at the Larmor frequency, and it is solely this RF component which has a significant effect on Φ_S i.e. other single frequency RF fields will have a negligible effect. It therefore appears that the conflicting experimental results are compatible with different RP systems. The Larmor resonance observed by Ritz *et al.* in 2009[168] seemingly gives strong evidence for the uncoupled FAD-Z radical pair. However, the more recent studies by Engels *et al.*[43] and Schwarze *et al.*[179] directly contradict these findings, and appear to rule out the uncoupled FAD-Z radical pair, instead pointing towards a more general RP such as the FAD-Trp radical pair or the dipolar coupled FAD-Z radical pair.

In terms of designing behavioural experiments to determine the identity of the RP *in vivo*, the obvious test is to compare the effects of single frequency magnetic fields at the Larmor frequency and some other arbitrary frequency with broadband noise effects, specifically with a noise field which does not contain ν_L. However, it seems that these tests have been carried out in the three studies discussed above, though have given contradictory results. Importantly, unlike the majority of others, these three studies have a negative condition, one in which an RF magnetic field does not disrupt the magnetic orientation of their test animal, which make them of

particular interest. There are a number of experimental protocols that we suggest below to try to improve the reproducibility of the behavioural results,[73] and independent corroboration of these studies could be very important to the field.

Aside from this, our calculations above suggest a further experimental condition that could provide significant information about the identity of the sensing RP. For the (uncoupled) FAD-Trp radical pair, it appears that a 70-80 MHz has a similar effect on the singlet yield as the 0-10 MHz field.[73] Before now, only frequency ranges < 10 MHz have been considered in experiments, and if a 70-80 MHz noise field caused magnetic disorientation as predicted by the results above (Fig. 5.3B), this would provide significant evidence for a RP-based sensor. We predict that for all but a small number of idealised RPs, such as FAD-Z (be it dipolar coupled or not), there would be a significant number of hyperfine interactions in each radical, as well as a non-zero radical-radical interaction term, meaning we would expect significant resonance effects in the 70-80 MHz range.

A positive result would be particularly convincing if combined with a control condition, in which we a predict an RF field condition in which a RP compass would not be disturbed. The obvious choice is to use a noise band which falls outside the range of energy level transitions of the RP. Unfortunately, estimating this upper limit is not straight forward, but as an initial guess, if we extend the FAD-Trp spin system to include all 15 and 12 nuclei in the radicals respectively, we find that the maximum resonance frequencies are ~ 120 and ~ 100 MHz respectively. This means that the largest expected (combination) excitation we would predict would be the sum of these frequencies i.e. 220 MHz. Therefore, we suggest a negative control condition using a 240-250 MHz magnetic noise band. We appreciate that there are significant technical challenges in realising a well-controlled magnetic field with such high frequency oscillating terms.[154]

C. Experimental protocols

One of the major problems in the interpretation of the behavioural results concerning RF magnetic field effects on compass orientation is the prevalence of conflicting reports. If the reproducibility of experimental studies could be improved, so too would the strength of the conclusions made on the basis of these studies. We propose a number of requirements for future work which we believe would greatly improve confidence in behavioural results.

Our suggestions can be concisely summarised as the requirement of having an accurate description of the magnetic field conditions in the experiment.[73] As discussed above, if we are observing a Larmor resonance, the "field strength" quoted should include all frequencies that would excite the transition, and not just some measure of the field strength at exactly ν_{L}. Similarly, a thorough measurement of a broadband noise condition is required, as all too often studies quote a number in nano Tesla with no reference to the frequency bins over which this intensity is integrated. Additionally, as we have seen, frequency components outside the range previously considered (> 10 MHz) could have significant effects on the RP reaction, and should also be controlled for.

To alleviate these problems, our suggestions are

- The spectrum of the magnetic and electric components of the RF field up to at least 100 MHz must be measured, giving an accurate picture of which RF components are present in the experiment.

- The envelope of frequencies used as a nominally single frequency field should be reported.

- The amplitude of RF noise in T $\mathrm{Hz}^{-1/2}$ should be presented, whether or not it is intentionally added.

- The spatial variation of the magnetic field condition should be measured, particularly as it can be difficult to achieve uniformity of high frequency fields in

large coil systems.

IV Conclusions

The primary conclusion from the work in this chapter is that the observed magnetic disorientation of migratory birds by RF magnetic fields is incompatible with the current model of RP magnetoreception. In order to observe effects of the size expected to disrupt the operation of a RP sensor under the conditions quoted in experimental studies, the spin coherence lifetime of the RP would have to be several orders of magnitude longer than predicted by even the most generous simulations including spin relaxation (see, for instance, Fig. 4.6). The immediate corollary of this observation must be that either our modelling of the system must be fundamentally flawed, or there is a serious artifact in all the behavioural studies.

If we are to suspend disbelief and investigate the resonance effects of RF fields on RPs, we see a clear distinction between the effect of broadband noise and single frequency magnetic fields. The idealised FAD-Z radical pair can exhibit high sensitivity to a Larmor frequency magnetic field, though this special resonance is abolished by even a relatively small dipolar coupling. For the other RP systems considered, including the dipolar-coupled FAD-Z, we found that broadband noise fields had a qualitatively more significant effect on the singlet yield than single frequency fields.

We have proposed a set of experimental conditions which could offer useful information for the identity of the RP *in vivo*. Unfortunately, as these predictions are based on this assumption of exceedingly slow spin relaxation, any evidence based on these predictions comes with a strong caveat. We have also suggested a number of experimental protocols which, if implemented, we believe could greatly improve the reproducibility and reliability of future behavioural studies, by having strict requirements on the characterisation of the experimental magnetic field conditions.

Acknowledgements

The discussion of results, use of action-spectrum histograms, considerations of the linewidth of the Larmor resonance and design of behavioural experiments were all done in collaboration with Peter Hore. Further discussion of results and relation to experimental design and protocol was provided by Henrik Mouritsen and David Manolopoulos.

Chapter 6

Quantum Noise in the Radical Pair Compass

In Chapter 4, we discussed how varying the recombination lifetime of the FAD-Trp radical pair could give rise to very sharp signals in the singlet yield[74] (Fig. 4.2). The advantage of this compass "needle" appears to be conceptually obvious, as a sharper signal could be expected to give a more accurate compass bearing than, for instance, the smoother FAD-Z signal (Fig. 4.1). Another study investigated how a needle-like feature could be generated by a modified (although highly contrived) RP mechanism, and presented simple model simulations to illustrate the improvement in navigation accuracy afforded by such sharp signals.[160] However, it should also be noted that the signal anisotropy for the FAD-Trp radical pair is exceedingly small,[74,116,124] particularly compared to that of the FAD-Z signal. It has been suggested that the anisotropy being so small could be problematic *in vivo* as there will be sources of noise in the mechanism and signalling cascade which could swamp such a small signal.[94] While we know next to nothing about the signal transduction pathway,[35] and therefore cannot make any meaningful assumptions about noise arising from this aspect of the mechanism, we can consider the effect of quantum noise[55] which is inherent in the RP model.

A further and related unresolved detail of the RP hypothesis is the seeming contradiction in having a light-dependent mechanism being responsible for the magnetic sense in night migratory birds,[81] who presumably use this sense under low light conditions. As each RP reaction is photo-activated, and the singlet yield is the fractional average over many RP reactions, having a finite number of photons (or reaction cycles) introduces some uncertainty into the compass signal available from a RP. In this chapter, we present an analysis of the effect of this quantum noise on the accuracy of a compass bearing available from different RPs under low light conditions.

I Origin of noise

The methods previously presented for calculating the singlet yield of RP reactions[27,195,197] (Chapters 2 and 3) have used a density matrix approach. As discussed in Section 2.I, this approach is used in order to model the statistical ensemble of possible initial states of the RP,[47] and represents an average over these initial states. Additionally, the reaction kinetics are treated using the Haberkorn operator which captures the average decrease in the population of different states over time.[64]

By contrast, a single RP reaction will have a well-defined initial state with a random configuration of the nuclear spins. The reaction "trajectory" will terminate at some particular time t_{R}, when the RP recombines to give one of the singlet or triplet products. In order to converge on the average Φ_{S}, it is necessary to average over very many reaction cycles. In order to capture the RP spin dynamics by discrete trajectories, the time-dependence of the singlet probability, $P_{\mathrm{S}}(t)$ (which gives the probability of forming the singlet product over time) for each initial state needs to be sampled. Fig. 6.1 offers an illustrative example of $P_{\mathrm{S}}(t)$ for just two of the initial states for a simple 3-spin RP which contains a single proton with principal hyperfine components: $(A_{xx}, A_{yy}, A_{zz}) = (-0.0989, -0.0989, 1.752)$ mT.

It is possible to model many individual RP reactions by propagating a random

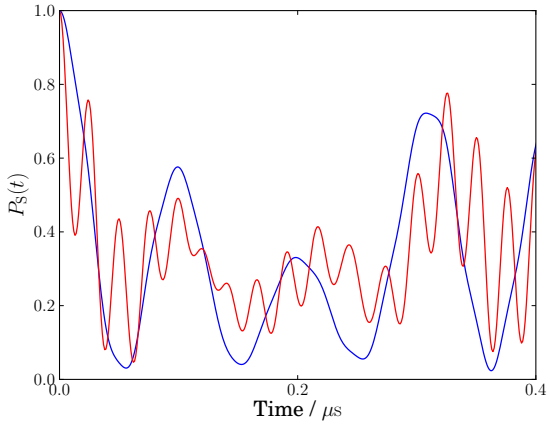


Figure 6.1: The time-dependence of the singlet probability of a toy RP containing one proton with hyperfine components: $(A_{xx}, A_{yy}, A_{zz}) = (-0.0989, -0.0989, 1.752)$ mT for two different initial nuclear spin configurations.

initial state over time before a reaction event, at which point either the singlet or triplet product is formed (see the Kinetic Monte Carlo algorithm[200] below). However, this is exceedingly computationally expensive for all but the most simple RPs, and so instead it would be preferable if we could derive the statistical distribution which would describe the fractional singlet yield given a finite number of photons/reaction cycles $\Phi_S(N)$, which would mean the calculation (given that we know the average $\Phi_S = \Phi_S(\infty)$) reduces to drawing random numbers from the appropriate distribution.

II Binomial distribution

To derive how the singlet yield is distributed for a finite number of reaction cycles, let us first consider the case where $N = 1$. The outcome of this reaction is dependent on the singlet probability of the radical pair (RP) when it reacts $P_S^{\alpha}(t_R)$. This in turn depends on the time at which the RP reacts t_R and the random initial nuclear spin configuration of the RP, labelled by α. The probability of this single RP reaction forming the singlet product is simply the singlet probability at time t_R given the α

initial state:

$$\mathrm{P}\big(\Phi_{\mathrm{S}}(1)=1|t_{\mathrm{R}},\alpha\big)=P_{\mathrm{S}}^{\alpha}(t_{\mathrm{R}}). \tag{6.1}$$

In order to compute the overall probability of forming the singlet product, we need to include the time dependence of the singlet probability, as well as the dependence on the random initial product state. This is done by combining this probability together with the probability of the RP recombining at time t_{R} and having initial state α, $\mathrm{P}(t_{\mathrm{R}})\times\mathrm{P}(\alpha)=\mathrm{P}(t_{\mathrm{R}},\alpha)$. $\mathrm{P}(\alpha)=1/Z$ is simply one over the number of nuclear spin configurations and, with a symmetric reaction scheme ($k_{\mathrm{S}}=k_{\mathrm{T}}=k$ in Fig. 1.1) $\mathrm{P}(t_{\mathrm{R}})=ke^{-kt_{\mathrm{R}}}$ (Eq. 2.10). For a more complex reaction scheme, this term is more complicated, but the final result in Eq. 6.2 remains valid.

Integrating this combined probability over all possible combinations of t_{R} and α[164] (i.e. using the law of total probability,[11] Eq. 6.23) gives the overall probability of a single RP reaction forming the singlet product

$$\begin{aligned}\mathrm{P}\big(\Phi_{\mathrm{S}}(1)=1\big)&=\sum_{\alpha}\int_{0}^{\infty}\mathrm{P}\big(\Phi_{\mathrm{S}}(1)=1|t_{\mathrm{R}},\alpha\big)\mathrm{P}\big(t_{\mathrm{R}},\alpha\big)\mathrm{d}t_{\mathrm{R}}\\&=\sum_{\alpha}\int_{0}^{\infty}P_{\mathrm{S}}^{\alpha}(t_{\mathrm{R}})\mathrm{P}\big(t_{\mathrm{R}},\alpha\big)\mathrm{d}t_{\mathrm{R}}\\&=\mathrm{E}\left[P_{\mathrm{S}}^{\alpha}(t_{\mathrm{R}})\right]=\Phi_{\mathrm{S}}.\end{aligned} \tag{6.2}$$

Therefore we find that the probability of a single reaction resulting in the singlet product is equal to the expectation value of the singlet probability of the RP, which is exactly the average singlet yield Φ_{S}.

Using this result, we can now derive the distribution describing the singlet yield for a finite number of reaction cycles, $\Phi_{\mathrm{S}}(N)$. For N reactions, as each reaction is an independent trial, we have N identical trials each with probability $p=\Phi_{\mathrm{S}}$. This describes the following Binomial distribution[18] (normalised by $1/N$)

$$\begin{aligned}&\Phi_{\mathrm{S}}(N)\sim\frac{1}{N}\mathcal{B}\left(N,\Phi_{\mathrm{S}}\right)\\&\Rightarrow\mathrm{P}\left(\Phi_{\mathrm{S}}(N)=\frac{X}{N}\right)=\binom{N}{X}\Phi_{\mathrm{S}}^{X}\left(1-\Phi_{\mathrm{S}}\right)^{N-X}.\end{aligned} \tag{6.3}$$

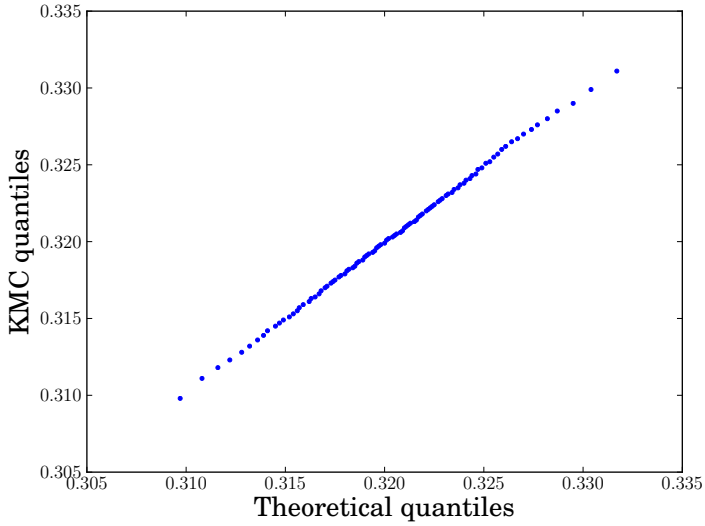


Figure 6.2: A quantile-quantile plot comparing the distribution of normalized singlet yield data calculated using the Kinetic Monte Carlo algorithm (KMC quantiles) against the quantiles expected from Eq. 6.3. The results shown are for $N = 10^5$ and 10^5 KMC calculations.

For large N, the central limit theorem states that this Binomial distribution is accurately approximated[14] by a normal distribution with mean Φ_S and variance $\Phi_S(1-\Phi_S)/N$:

$$\begin{aligned} &\Phi_S(N \to \infty) \sim \mathcal{N}\left(\Phi_S, \Phi_S(1-\Phi_S)/N\right) \\ &\Rightarrow \mathrm{P}\left(\Phi_S(N) = \frac{X}{N}\right) \simeq \frac{1}{\sqrt{2\pi\left(\Phi_S(1-\Phi_S)/N\right)}} e^{-\frac{(\Phi_S - X/N)^2}{2(\Phi_S(1-\Phi_S)/N)}}. \end{aligned} \tag{6.4}$$

It is worth considering the implications of this result. The width of the distribution of $\Phi_S(N)$ is given by $\sqrt{\Phi_S(1-\Phi_S)}/\sqrt{N}$. Unless Φ_S is close to 0 or 1, the Φ_S-dependent term is roughly constant, and the majority of the uncertainty in $\Phi_S(N)$ is determined by the value of N, the number of reaction cycles, and scales as $1/\sqrt{N}$.

We can numerically verify this result (Fig. 6.2) using a Kinetic Monte Carlo (KMC) algorithm[200] to model the 3-spin RP described above (Fig. 6.1). We calculate the fractional singlet yield of N reaction cycles by explicitly computing the outcome of N reaction trajectories, and then compare the distribution of many cal-

culated singlet yields against the expected Binomial distribution in Eq. 6.3. With a (symmetric) RP recombination rate k, the calculation takes the following steps:

1. Randomly select an initial nuclear spin configuration, α, and combine with a pure singlet state in the electron spins ($|\Psi^{\alpha}(0)\rangle$).

2. Propagate this initial state to $t_{\mathrm{R}} = k^{-1}\ln(1/u_1)$ where $u_1 \in (0,1]$ is a random number between 0 and 1 ($|\Psi^{\alpha}(t_{\mathrm{R}})\rangle = e^{-\mathrm{i}\hat{H}t_{\mathrm{R}}}|\Psi^{\alpha}(0)\rangle$).

3. Draw a second random number $u_2 \in (0,1]$. If $u_2 < P_{\mathrm{S}}^{\alpha}(t_{\mathrm{R}}) \equiv \langle\Psi^{\alpha}(t_{\mathrm{R}})|\hat{P}_{\mathrm{S}}|\Psi^{\alpha}(t_{\mathrm{R}})\rangle$ then the trajectory forms the singlet product, otherwise the triplet product is formed.

4. Repeat this procedure for the desired number of reaction cycles and compute the fractional singlet yield.

We use this KMC method to compute $\Phi_{\mathrm{S}}(10^5)$ i.e. the fractional singlet yield of 10^5 reaction cycles, many (10^5) times. We then compare the distribution of the calculated singlet yields against the expected Binomial distribution in Eq. 6.3 using a quantile-quantile (Q-Q) plot in Fig. 6.2. A Q-Q plot shows the positions of the quantiles (i.e. the i^{th} quantile is the value below which $i\%$ of the data falls) of one set of data against another, and is a graphical method of comparing the distributions of the two data sets, which are equivalent if the points fall on the line $y = x$.[206] Clearly this is the case in Fig. 6.2, verifying our derivation of Eq. 6.3.

III Information Theory

Now that we can describe the singlet yield for a finite number of reaction cycles, we would like to apply our findings to magnetoreception, in order to assess the effect of quantum noise under low light conditions on the functioning of a RP compass *in vivo*. As discussed in Chapter 1, it is proposed that the magneto-sensing cryptochrome proteins are housed in photoreceptor cells in the retina[81,152,185] (Fig. 6.3B), and there

is experimental evidence that the RP reactions indeed occur in the eye.[127,145,146,222] The proteins are thought to be immobilized in at least one angle so that each has a well-defined orientation.[70,115] For a given heading direction, "magnetoreceptor cells" from different parts of the retina will experience different relative magnetic field directions, and so have different average fractional yields of the RP reaction. For a single heading, there is therefore a potentially complex signal from magnetoreceptor cells across the whole retina[165,185] (Fig. 6.3C).

Unfortunately, as discussed above, the fact that we know so little about the processing and interpretation of the singlet yield in the signal transduction pathway[35] means that it is very difficult to form conclusions about the accuracy of different RP compasses without making a number of assumptions about the signalling cascade of unknown validity. To circumvent this difficulty, we use an information theory approach[69,119] in our analysis, which allows us to calculate a best case accuracy of a RP compass.

Information Theory[30,83,86] is generally applied to data communication in, for instance, computer buses. In these systems, there is generally a source of data, an encoding of the data in a channel, and a receiver which decodes the output of the channel to generate the signal. Depending on the capacity of the channel, the source can either be perfectly reconstructed from the output (noisy-channel coding theorem), or approximately reconstructed within a specified error range[30] (rate distortion theory). As applied to magnetoreception, we can think of the external field direction as the source of data, which is encoded in the singlet yield in the receptor cells in the retina,[165,185] which in turn is decoded to give an estimate of the field direction (a schematic representation is given in Fig. 6.3).

The key quantities in Information Theory are the Shannon entropy $h(X)$, which measures the uncertainty in the value of a random variable, X, based on its domain of possible values, and the conditional entropy $h(X|Y)$ which measures this uncertainty when the domain of X is restricted by knowledge of Y (see Eqs. 6.8 and 6.9

below). Together, these can be combined to compute the amount of "information" about variable X that is available from a stochastic source of data Y[180]

$$I(X;Y) \equiv h(X) - h(X|Y). \tag{6.5}$$

Interpreting this equation, we see that the more the uncertainty in X is reduced by knowledge of Y, the smaller $h(X|Y)$ and so the larger the mutual information.[30] If X is entirely determined by Y, the information is maximal, and is bounded by the entropy of X. If instead X and Y are independent, $h(X|Y) = h(X)$ and the mutual information is zero. This relation (Eq. 6.5) is the basis of our derivation of the lower bound heading error.[71]

Returning to our application, we are interested in the distribution of a bird's heading direction, Θ, which is the direction in which the bird is facing and determines the direction of the geomagnetic field relative to the magnetoreceptors in the bird's eye. We want to find how the uncertainty in Θ is reduced given the bird's estimate of its heading direction, $\hat{\Theta}$, as determined by the encoding of the relative magnetic field direction in the singlet yield signal from magnetoreceptors across the retina[165] ($\mathbf{\Phi}_{\mathrm{S}}(\Theta; N) = \{\Phi^i_{\mathrm{S}}(\Theta, N)\}$). This exactly describes the mutual information[180] $\mathrm{I}(\Theta; \hat{\Theta})$, which connects panels A and E in Fig. 6.3.

Relating this quantity to the number of reaction cycles, if $N = 0$ there is clearly no information available about the external magnetic field, and therefore Θ and $\hat{\Theta}$ are independent and the mutual information is zero. As N increases, the amount of the information available from the singlet yield signal increases as the signal to noise ratio improves (the noise scales as $1/\sqrt{N}$). In the limit $N \to \infty$ (assuming noiseless signal transduction), the magnetic field information is perfectly encoded in $\mathbf{\Phi}_{\mathrm{S}}(\Theta; N)$, and therefore the conditional entropy $h(\Theta|\hat{\Theta}) = 0$ and $\mathrm{I}(\Theta; \hat{\Theta})$ is maximal.

However, as we do not know how $\mathbf{\Phi}_{\mathrm{S}}(\Theta; N)$ is decoded by the signal transduction pathway, we cannot quantify $h(\Theta, \hat{\Theta})$ and therefore cannot calculate the mutual

information $\mathrm{I}(\Theta, \hat{\Theta})$. To sidestep this difficulty, we use the data processing inequality:[9,151]

$$\mathrm{I}(\Theta; \hat{\Theta}) \leq \mathrm{I}(\Theta; \mathbf{\Phi}_{\mathrm{S}}(\Theta; N)). \tag{6.6}$$

This states that, because the estimate of the heading direction is "downstream" from the singlet yield signal, i.e. $\hat{\Theta}$ is computed based on $\mathbf{\Phi}_{\mathrm{S}}(\Theta; N)$, the amount of information encoded in the singlet yield cannot increase on being decoded to give $\hat{\Theta}$. The significance of this is that, as we can compute the mutual information between Θ and $\mathbf{\Phi}_{\mathrm{S}}(\Theta; N)$, we can compute a strict upper bound on the information between Θ and $\hat{\Theta}$, for any arbitrary decoding of the singlet yield signal to compute $\hat{\Theta}$.[71]

We can use well known results from Information Theory[30,83,86] (see below) together with Eq. 6.6 to compute a lower bound estimate of the mean squared difference between Θ and $\hat{\Theta}$ (see derivation below) to evaluate the accuracy of the RP compass[71] for a given encoding of the magnetic field, which depends on the identity of the sensing RP and N

$$\mathrm{E}\left[(\Theta - \hat{\Theta})^2\right] = \epsilon^2 \geq \frac{2\pi}{e} \exp\Big(- 2\mathrm{I}(\Theta; \mathbf{\Phi}_{\mathrm{S}}(\Theta; N))\Big). \tag{6.7}$$

The real power of this method is that Eq. 6.7 gives the lower bound of ϵ for any arbitrarily sophisticated data processing algorithm used to interpret the singlet yield signal, and so successfully avoids having to make any guesses about the signal transduction *in vivo*, instead assuming the optimal case. Considering the complexity of data processing known in, for instance, the visual system,[82] the ability to account for a highly developed signalling cascade is an important one. Below we give the derivation of Eq. 6.7 as well as the method for its evaluation.[71]

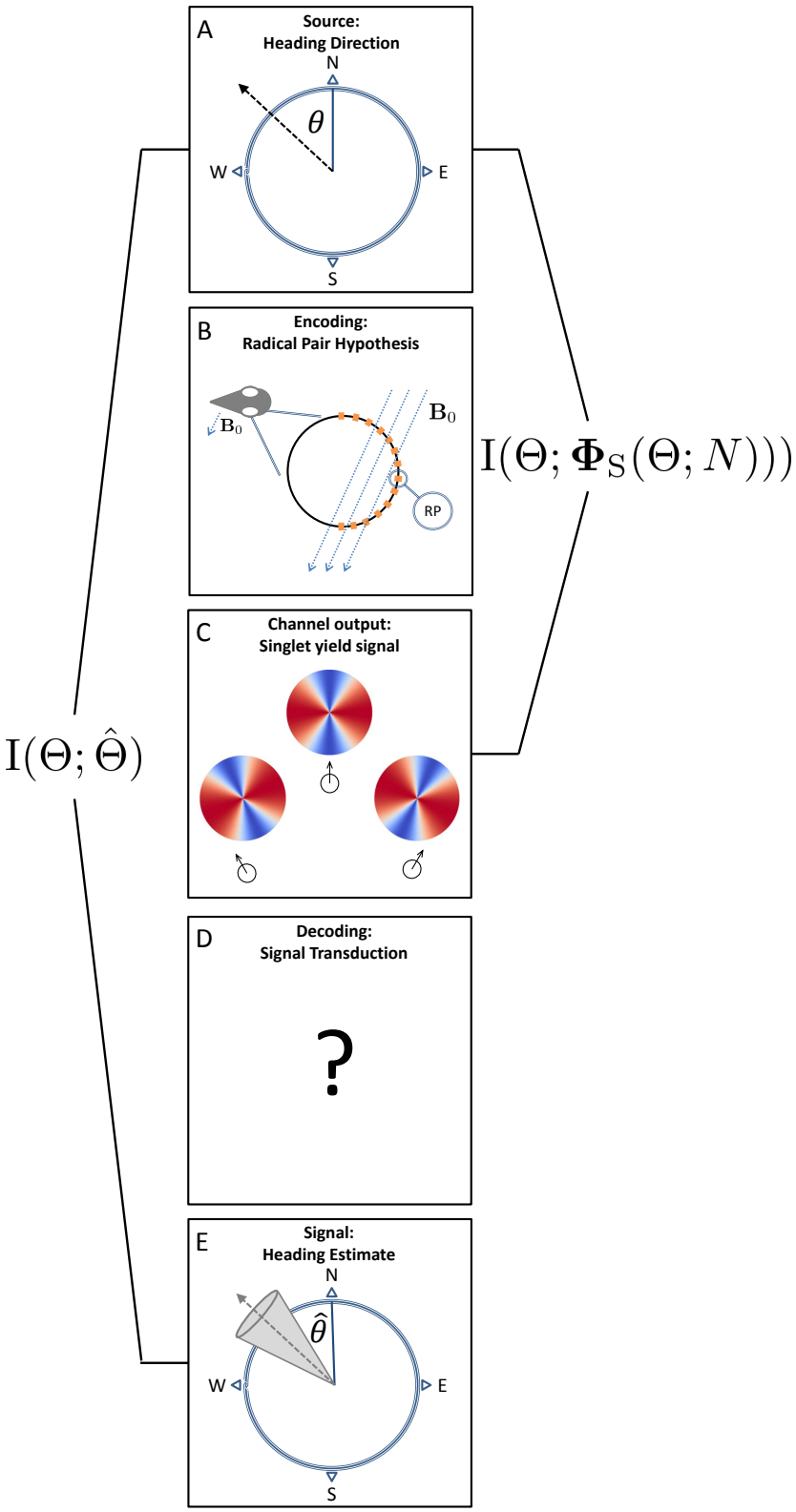


Figure 6.3: A schematic representation of our Information Theory approach. A, the signal input is the heading direction of the bird. B, the heading direction dictates the direction of the external magnetic field relative to the bird, which is encoded in the fractional yield of RPs which are in a fixed orientation within the magnetoreceptor cell in the retina. C, each receptor cell experiences a different relative field direction, and so has a different average singlet yield which is represented in these Visual Modulation Patterns. The signal varies as the heading direction varies. The results here are for the limit of large N. D, $\mathbf{\Phi}_{\mathrm{S}}(\Theta; N)$ is decoded by some unknown data processing algorithm. E, the heading direction is estimated. The mutual information between different steps in the process is indicated. Modified from Ref. 71

Notation

At this point it is useful to clarify the notation that will be used in this chapter. The important distinction to be made is between random variables and specific realisations of those random variables. For instance, we are interested in the distribution of the heading direction, but also the behaviour of the singlet yield signal for a specific heading direction. In this chapter, we will use upper case to denote random variables: Θ, $\hat{\Theta}$ and $\mathbf{\Phi}_{\mathrm{S}}(\Theta; N)$, and lower case to denote specific values of these variables: θ, $\hat{\theta}$ and $\boldsymbol{\phi}_{\mathrm{S}}(N)$. For the singlet yield signal, the dependence of $\mathbf{\Phi}_{\mathrm{S}}(\Theta; N)$ on the distribution of Θ is made explicit, but for a specific value this dependence is left implicit for neatness in the equations below. The other distinction is that an upper case Φ_{S} which does not have an N-dependence denotes an average singlet yield i.e. $\Phi_{\mathrm{S}} = \Phi_{\mathrm{S}}(\infty)$.

IV Deriving the lower bound heading error

A. Shannon entropy

The differential entropy (or Shannon entropy) $h(X)$ is the basic building block of Information Theory and Rate Distortion Theory.[30] For a continuous random variable with probability density function $p(x)$, it is defined as the expectation value of $\ln(1/p(x))$[180]

$$h(X) = -\int p(x) \ln\big(p(x)\big) \mathrm{d}x. \tag{6.8}$$

As a simple example, the random variable Θ is uniformly distributed between $-\pi$ and π (in radians), meaning the Shannon entropy of Θ is

$$h(\Theta) = -\int_{-\pi}^{\pi} \frac{1}{2\pi} \ln\left(\frac{1}{2\pi}\right) \mathrm{d}\theta = \ln(2\pi). \tag{6.9}$$

Another important quantity is the conditional entropy, which is a measure of the entropy of variable X given knowledge of variable Y. This is defined as[180]

$$h(X|Y) = -\int\int p(x,y)\ln\big(p(x|y)\big)\mathrm{d}x\mathrm{d}y. \tag{6.10}$$

One important result regarding the entropy is that, given the variance (σ^2) of the probability density of X, the entropy is maximal for the distribution of X being a Gaussian distribution[30] with variance σ^2 ($X \sim \mathcal{N}(\mu, \sigma^2)$)

$$h(X) \leq h\left(X \sim \mathcal{N}(\mu,\sigma^2)\right) = \frac{1}{2}\ln(2\pi e\sigma^2). \tag{6.11}$$

For an n-dimensional random variable $\mathbf{X}$, the analogous maximum is given by a multi-dimensional Gaussian distribution,[30] and the Shannon entropy depends on the $n \times n$ covariance matrix of the distribution, Σ

$$h(\mathbf{X}) \leq h\left(\mathbf{X} \sim \mathcal{N}(\boldsymbol{\mu},\Sigma)\right) = \frac{1}{2}\ln\left((2\pi e)^n \det(\Sigma)\right), \tag{6.12}$$

where the elements of the covariance matrix are defined as

$$\Sigma_{ij} = \mathrm{cov}[X_i, X_j] = \mathrm{E}\left[(X_i - \mathrm{E}[X_i])(X_j - \mathrm{E}[X_j])\right]. \tag{6.13}$$

B. Mutual Information

Starting from the mutual information between Θ and $\hat{\Theta}$

$$\mathrm{I}(\Theta;\hat{\Theta}) \equiv h(\Theta) - h(\Theta|\hat{\Theta}) \tag{6.14}$$

we manipulate the conditional entropy term in order to derive Eq. 6.7. As we are looking to evaluate the accuracy of the RP compass, we first relate this term to $h(\Theta - \hat{\Theta})$ as a measure of the variance of the distribution of the difference (or error)

between $\hat{\Theta}$ and Θ

$$h(\Theta|\hat{\Theta}) = h(\Theta - \hat{\Theta}|\hat{\Theta}) \leq h(\Theta - \hat{\Theta}). \tag{6.15}$$

The equality derives from the fact that we are in effect subtracting a constant in the conditional entropy, and Shannon entropy is invariant under translation.[30] The inequality is Shannon's lower bound, and comes from the well known concept that conditioning cannot increase entropy.[181]

We can evaluate a bound on this entropy using Eq. 6.11 in terms of the variance ϵ^2

$$h(\Theta - \hat{\Theta}) \leq \frac{1}{2}\ln(2\pi e\epsilon^2). \tag{6.16}$$

Assuming that the expectation value $\mathrm{E}[\Theta - \hat{\Theta}] = 0$ (by symmetry), we can equate the variance with the mean squared error in the heading estimate

$$\epsilon^2 = \mathrm{E}\left[\left(\Theta - \hat{\Theta}\right)^2\right] - \left(\mathrm{E}\left[\Theta - \hat{\Theta}\right]\right)^2 = \mathrm{E}\left[\left(\Theta - \hat{\Theta}\right)^2\right]. \tag{6.17}$$

Eq. 6.16 means that we can put a bound on the error of the estimator[71] $\hat{\Theta}$

$$\epsilon^2 \geq \frac{1}{2\pi e}\exp\left(2h(\Theta - \hat{\Theta})\right). \tag{6.18}$$

First replacing $h(\Theta - \hat{\Theta})$ by $h(\Theta) - \mathrm{I}(\Theta;\hat{\Theta})$ using Eqs. 6.14 and 6.15, we then apply the data processing inequality[9,151] (Eq. 6.6). This finally yields our expression for the lower bound of the mean-squared error in the heading estimate based on the encoding of the true heading in the singlet yield signal across the retina[71]

$$\epsilon^2 \geq \frac{1}{2\pi e}\exp\Big(2(h(\Theta) - \mathrm{I}(\Theta;\mathbf{\Phi}_{\mathrm{S}}(\Theta;N)))\Big). \tag{6.19}$$

V Computing the lower bound heading error

In order to compute the error bound (Eq. 6.19), we need to consider each of the entropies involved in the expression. $h(\Theta)$ is simply evaluated as above (Eq. 6.9). In

the mutual information, there are two terms that require a more involved calculation

$$\mathrm{I}(\Theta; \mathbf{\Phi}_{\mathrm{S}}(\Theta; N)) = h(\mathbf{\Phi}_{\mathrm{S}}(\Theta; N)) - h(\mathbf{\Phi}_{\mathrm{S}}(\Theta; N)|\Theta). \tag{6.20}$$

In order to proceed, we will use the Gaussian approximation of the singlet yield probability distribution for large N from the central limit theorem (Eq. 6.4). For a given heading direction $\Theta = \theta$, the mean and variance at each of the N_{rec} receptor cells (labelled by i) can be written in terms of the average singlet yield $\Phi^i_{\mathrm{S}}(\theta)$:

$$\begin{aligned} \mu_{i|\theta} &= \Phi^i_{\mathrm{S}}(\theta), \\ \sigma^2_{i|\theta} &= \Phi^i_{\mathrm{S}}(\theta)(1 - \Phi^i_{\mathrm{S}}(\theta))/N. \end{aligned} \tag{6.21}$$

so that the probability density function of the singlet yield signal being $\mathbf{\Phi}_{\mathrm{S}}(\Theta; N) = \boldsymbol{\phi}_{\mathrm{S}}(N) = \{\phi^i_{\mathrm{S}}(N)\}$ given a heading direction θ and number of photons N becomes[164]

$$p\left(\boldsymbol{\phi}_{\mathrm{S}}(N)|\theta\right) = \prod_{i=1}^{N_{\mathrm{rec}}} \mathcal{N}\left(\mu_{i|\theta}, \sigma^2_{i|\theta}\right). \tag{6.22}$$

The other important result that will be used below is the law of total probability,[11] which for our purposes takes the form

$$\begin{aligned} p\left(\boldsymbol{\phi}_{\mathrm{S}}(N)\right) &= \int p(\boldsymbol{\phi}_{\mathrm{S}}(N)|\theta) p(\theta) \mathrm{d}\theta \\ &= \sum_{k=1}^{K} p(\boldsymbol{\phi}_{\mathrm{S}}(N)|\theta_k) \mathrm{P}(\theta_k). \end{aligned} \tag{6.23}$$

This relation states that, in order to describe the probability distribution of the singlet yield signal, $\mathbf{\Phi}_{\mathrm{S}}(\Theta; N)$, we can consider the distribution of the signal for a fixed θ, and then sample over the distribution of Θ. In the second line, we have replaced the integral over θ with a sum as we will evaluate the integral using numerical quadrature, not having a closed form expression for how the average singlet yield signal varies with θ. $\mathrm{P}(\theta) = 1/K$ where K is the number of values of θ sampled to

calculate the integral. We use $K = 1000$ to converge the error to within 1°.

A. The conditional entropy

Calculating the conditional entropy is relatively straightforward as, for a given value of θ, the singlet yield at each receptor is described by an independent Gaussian

$$\begin{aligned} h(\mathbf{\Phi}_{\mathrm{S}}(\Theta;N)|\Theta) &= -\int\int p(\boldsymbol{\phi}_{\mathrm{S}}(N),\theta)\ln\big(p(\boldsymbol{\phi}_{\mathrm{S}}(N)|\theta)\big)\mathrm{d}\boldsymbol{\phi}_{\mathrm{S}}(N)\mathrm{d}\theta \\ &= -\frac{1}{K}\sum_{k=1}^{K}\int p(\boldsymbol{\phi}_{\mathrm{S}}(N)|\theta_k)\ln\big(p(\boldsymbol{\phi}_{\mathrm{S}}(N)|\theta_k)\big)\mathrm{d}\boldsymbol{\phi}_{\mathrm{S}}(N), \end{aligned} \tag{6.24}$$

where we have used $p(\boldsymbol{\phi}_{\mathrm{S}}(N),\theta) = p(\boldsymbol{\phi}_{\mathrm{S}}(N)|\theta)\mathrm{P}(\theta)$ in going from the first line to the second. As stated above, we are going to numerically sample over the distribution of Θ, and the integral over θ is approximated by a summation.

For each value of θ_k, the integral exactly corresponds to the entropy of a multivariate Gaussian (Eq. 6.12). Since the singlet yield at each receptor is independent for a fixed θ, the covariance matrix of this distribution is diagonal, meaning the total entropy is the sum of entropies of independent Gaussian variables representing the singlet yield at each receptor. We can therefore use Eq. 6.11 to write:

$$h(\mathbf{\Phi}_{\mathrm{S}}(\Theta;N)|\Theta) = \frac{1}{2K}\sum_{k=1}^{K}\sum_{i=1}^{N_{\mathrm{rec}}}\ln\left(2\pi e\sigma^2_{i|\theta_k}\right). \tag{6.25}$$

Meaning the conditional entropy can be calculated by summing the entropy of all receptors and numerically averaging over many values of θ.[71]

B. Signal entropy

The final quantity in Eq. 6.19 left to calculate is the entropy of the singlet yield signal, $h(\mathbf{\Phi}_{\mathrm{S}}(\Theta;N))$. Because of the variation of Φ_{S} with θ, the singlet yield at each receptor is not independent. For a pair of receptors, their singlet yield signals are correlated because of the fixed geometrical relation between them. Additionally, the

distribution of $\Phi_{\mathrm{S}}^{i}(\Theta;N)$ is not simply described by a Gaussian. Therefore we cannot straightforwardly evaluate the entropy. Instead, we compute the upper bound on the entropy using the multivariate Gaussian limit[30] in Eq. 6.12 (which is compatible with the bound in Eq. 6.19).

In order to compute this upper bound, we need to evaluate the elements of the covariance matrix, and so consider the probability distribution of pairs of receptors. We again use the law of total probability (Eq. 6.23) and the fact that the singlet yield at different receptors is independent for a given θ

$$\begin{aligned} p\Big(\phi_{\mathrm{S}}^{i}(N),\phi_{\mathrm{S}}^{j}(N)\Big) &= \sum_{k=1}^{K} p\Big(\phi_{\mathrm{S}}^{i}(N),\phi_{\mathrm{S}}^{j}(N)|\theta_k\Big)\mathrm{P}(\theta_k) \\ &= \frac{1}{K}\sum_{k=1}^{K} p\Big(\phi_{\mathrm{S}}^{i}(N)|\theta_k\Big)p\Big(\phi_{\mathrm{S}}^{j}(N)|\theta_k\Big). \end{aligned} \tag{6.26}$$

We can use this to evaluate the i,j element in the covariance matrix (where $\bar{\Phi}_{\mathrm{S}}^{i}$ is the average singlet yield at receptor i over all θ)

$$\begin{aligned} &\mathrm{E}\left[\Big(\phi_{\mathrm{S}}^{i}(N)-\bar{\Phi}_{\mathrm{S}}^{i}\Big)\Big(\phi_{\mathrm{S}}^{j}(N)-\bar{\Phi}_{\mathrm{S}}^{j}\Big)\right] \\ &\quad= \int p\left(\phi_{\mathrm{S}}^{i}(N),\phi_{\mathrm{S}}^{j}(N)\right)\Big)\Big(\phi_{\mathrm{S}}^{i}(N)-\bar{\Phi}_{\mathrm{S}}^{i}\Big)\Big(\phi_{\mathrm{S}}^{j}(N)-\bar{\Phi}_{\mathrm{S}}^{j}\Big)\mathrm{d}\phi_{\mathrm{S}}^{i}(N)\mathrm{d}\phi_{\mathrm{S}}^{j}(N) \\ &\quad= \frac{1}{K}\sum_{k=1}^{K}\int p\Big(\phi_{\mathrm{S}}^{i}(N)|\theta_k\Big)p\Big(\phi_{\mathrm{S}}^{j}(N)|\theta_k\Big)\Big(\phi_{\mathrm{S}}^{i}(N)-\bar{\Phi}_{\mathrm{S}}^{i}\Big)\Big(\phi_{\mathrm{S}}^{j}(N)-\bar{\Phi}_{\mathrm{S}}^{j}\Big)\mathrm{d}\phi_{\mathrm{S}}^{i}(N)\mathrm{d}\phi_{\mathrm{S}}^{j}(N) \\ &\quad= \frac{1}{K}\sum_{k=1}^{K}\mathrm{E}[\Phi_{\mathrm{S}}^{i}(\theta_k,N)-\bar{\Phi}_{\mathrm{S}}^{i}]\times\mathrm{E}[\Phi_{\mathrm{S}}^{j}(\theta_k,N)-\bar{\Phi}_{\mathrm{S}}^{j}] \end{aligned} \tag{6.27}$$

meaning the off-diagonal elements in the covariance matrix are simply the average of the covariance over all values of θ_k, which can be easily computed

$$\begin{aligned} &\mathrm{cov}[\Phi_{\mathrm{S}}^{i}(\theta_k,N),\Phi_{\mathrm{S}}^{j}(\theta_k,N)]_{\theta_k} \\ &\quad= \mathrm{E}[\Phi_{\mathrm{S}}^{i}(\theta_k,N)-\bar{\Phi}_{\mathrm{S}}^{i}]\times\mathrm{E}[\Phi_{\mathrm{S}}^{j}(\theta_k,N)-\bar{\Phi}_{\mathrm{S}}^{j}] \\ &\quad= \Big(\mu_{i|\theta_k}-\bar{\Phi}_{\mathrm{S}}^{i}\Big)\Big(\mu_{j|\theta_k}-\bar{\Phi}_{\mathrm{S}}^{j}\Big). \end{aligned} \tag{6.28}$$

Similarly, the diagonal components can be computed at each θ_k

$$\begin{aligned}
&\mathrm{cov}[\Phi_{\mathrm{S}}^i(\theta_k, N), \Phi_{\mathrm{S}}^i(\theta_k, N)]_{\theta_k} \\
&\quad = \mathrm{E}\left[\left(\Phi_{\mathrm{S}}^i(\theta_k, N) - \bar{\Phi}_{\mathrm{S}}^i\right)^2\right] \\
&\quad = \sigma_{i|\theta_k}^2 + \mu_{i|\theta_k}^2 - 2\mu_{i|\theta_k}\bar{\Phi}_{\mathrm{S}}^i + \left(\bar{\Phi}_{\mathrm{S}}^i\right)^2 .
\end{aligned} \tag{6.29}$$

Using these expressions, we can finally compute the total covariance matrix

$$\left(\Sigma_{\mathbf{\Phi}_{\mathrm{S}}(\Theta;N)}\right)_{ij} = \frac{1}{K}\sum_{k=1}^{K} \mathrm{cov}[\Phi_{\mathrm{S}}^i(\theta_k, N), \Phi_{\mathrm{S}}^j(\theta_k, N)]_{\theta_k} \tag{6.30}$$

meaning the entropy is bounded by

$$h(\mathbf{\Phi}_{\mathrm{S}}(\Theta; N)) \leq \frac{1}{2}\ln\left((2\pi e)^{N_{\mathrm{rec}}}\det(\Sigma_{\mathbf{\Phi}_{\mathrm{S}}(\Theta;N)}\right). \tag{6.31}$$

Therefore we can write the mutual information as

$$\begin{aligned}
\mathrm{I}(\theta; \mathbf{\Phi}_{\mathrm{S}}(\Theta; N)) &= h(\mathbf{\Phi}_{\mathrm{S}}(\Theta; N)) - h(\mathbf{\Phi}_{\mathrm{S}}(\Theta; N)|\Theta) \\
&\leq \frac{1}{2}\ln\left((2\pi e)^{N_{\mathrm{rec}}}\det(\Sigma_{\mathbf{\Phi}_{\mathrm{S}}(\Theta;N)})\right) - \frac{1}{2K}\sum_{k=1}^{K}\sum_{i=1}^{N_{\mathrm{rec}}}\ln\left(2\pi e\sigma_{i|\theta_k}^2\right).
\end{aligned} \tag{6.32}$$

Finally we are in a position to put together the entropy of the heading direction (Eq. 6.11) with the conditional entropy of the singlet yield (Eq. 6.25) and the bound on the entropy of the singlet yield (Eq. 6.31) to find a *strict* lower bound on the error in the estimator ($\hat{\Theta}$) of the heading direction (Θ) based on the singlet yield signal ($\mathbf{\Phi}_{\mathrm{S}}(\Theta; N)$) with N reactions cycles per magnetoreceptor cell[71]

$$\begin{aligned}
\epsilon^2 \geq\ & \frac{1}{2\pi e}\exp\left(2\ln(2\pi) - \ln\left((2\pi e)^{N_{\mathrm{rec}}}\det(\Sigma_{\mathbf{\Phi}_{\mathrm{S}}(\Theta;N)})\right)\right. \\
&\left. + \frac{1}{K}\sum_{k=1}^{K}\sum_{i=1}^{N_{\mathrm{rec}}}\ln\left(2\pi e\sigma_{i|\theta_k}^2\right)\right) \\
=\ & \frac{2\pi}{e} \times \frac{1}{(2\pi e)^{N_{\mathrm{rec}}}\det(\Sigma_{\mathbf{\Phi}_{\mathrm{S}}(\Theta;N)})} \times \prod_{k=1}^{K}\prod_{i=1}^{N_{\mathrm{rec}}}\left(2\pi e\sigma_{i|\theta_k}^2\right)^{1/K}.
\end{aligned} \tag{6.33}$$

VI Magnetoreceptors in the retina

Now that we have the necessary machinery to evaluate the accuracy of a RP compass for a given N, we need to define how the RPs are arrayed across the retina. Because of the curvature of the retina, and the relative orientation of the RP within the receptor cell, modelling the ensemble of RPs requires some geometrical manipulation.[165,166]

We assume for simplicity that the eye of a bird is roughly spherical. The relative direction of the external field vector is determined by the heading direction of the bird (the direction in which the bird is looking). Here, we denote the heading direction by θ and define $\theta = 0^\circ$ to be the direction of magnetic North. The other angle parameterising the field direction is the inclination angle (ϕ) and together these angles give the external field vector in the retina frame[114]

$$\mathbf{B}_{\mathrm{R}} = (\sin(\chi)\cos(\psi), \sin(\chi)\sin(\psi), \cos(\chi)), \tag{6.34}$$

where

$$\begin{aligned} \chi &= \arccos\big(-\cos(\theta)\cos(\phi)\big), \\ \psi &= \arctan\big(-\cos(\phi)\sin(\theta)/\sin(\phi)\big). \end{aligned} \tag{6.35}$$

In order to calculate Φ_{S} at each receptor, we require the field direction in the RP frame, and so need to first transform to the magnetoreceptor cell frame before transforming to the relative orientation of the RP within the receptor cell.[114] For simplicity, it is assumed that all RPs within a single receptor cell are perfectly aligned and that all receptor cells are identical, a simplification that is discussed below. The receptor cell orientation is defined by the angles $\{\kappa, \nu, \eta\}$. The cell is presumed to be normal to the retina surface, and the first two angles are determined by the position of the cell on the retina. If x and y are the coordinates of the cell when the retina

is projected onto a plane[114] (using an equal angle projection, Fig. 6.4B)

$$\begin{aligned} \kappa &= 2\arctan\left(\sqrt{x^2+y^2}\right), \\ \nu &= \arctan\left(x/y\right). \end{aligned} \tag{6.36}$$

The angle η gives the rotation about the long (z) axis of the cell. The choice of this angle is arbitrary as it combines with the z orientation of the RP within the cell.[185] The orientation of the RP within the cell is defined by angles $\{\alpha, \beta, \gamma\}$.

With these angles in hand, we can define the rotation which rotates the field vector in the retina frame to the RP frame[114]

$$\mathrm{R} = \mathrm{R}_z(\gamma)\mathrm{R}_y(\beta)\mathrm{R}_z(\alpha)\mathrm{R}_z(\eta)\mathrm{R}_y(\kappa)\mathrm{R}_z(\nu), \tag{6.37}$$

where

$$\begin{aligned} \mathrm{R}_y(\lambda) &= \begin{pmatrix} \cos(\lambda) & 0 & \sin(\lambda) \\ 0 & 1 & 0 \\ -\sin(\lambda) & 0 & \cos(\lambda) \end{pmatrix}, \\ \mathrm{R}_z(\lambda) &= \begin{pmatrix} \cos(\lambda) & -\sin(\lambda) & 0 \\ \sin(\lambda) & \cos(\lambda) & 0 \\ 0 & 0 & 1 \end{pmatrix}. \end{aligned} \tag{6.38}$$

Using this rotation matrix, we can find the field vector in the RP frame

$$\begin{aligned} \mathbf{B}_{\mathrm{RP}} &= \mathrm{R}\mathbf{B}_{\mathrm{R}} \\ &= (\sin(\zeta)\cos(\delta), \sin(\zeta)\sin(\delta), \cos(\zeta)) \end{aligned} \tag{6.39}$$

and so finally we have the (average) singlet yield at the receptor i whose position is defined by x and y with the bird's heading direction θ and inclination ϕ of the external field[114]

$$\Phi_{\mathrm{S}}^{i}(\theta) \equiv \Phi_{\mathrm{S}}(\zeta, \delta). \tag{6.40}$$

A. Visual Modulation Patterns

The singlet yield signal across the retina is generally visualised using Visual Modulation Patterns[165] (VMPs, see Fig. 6.4B). These represent the singlet yield at each "receptor cell" (we choose to group receptors, see below) as a pixel whose colour is determined by the singlet yield at that receptor cell (from blue to red), when the retina is projected onto a plane (by an equal angle projection modelling the retina as a hemisphere with the pupil at the zenith). In order to perform these calculations, it is necessary to make some arbitrary choices about values of the unknown angles above. For clarity in the VMPs, as well as ease of manipulation of the model system used below, we choose $\alpha + \eta = \pi/2$, $\beta = \pi/2$ and $\gamma = 0$. We assume that the exact choice of these angles is not important for our analysis,[166] but it should be noted that this does assume perfect orientation of the RPs in three dimensions in all the receptor cells.

For the inclination, we choose to consider the accuracy of the compass in Frankfurt (where many of the key behavioural experiments in the field have been conducted, e.g. Ref 211), where the inclination is[26] $\phi = 66°$. Further work could involve examining how the compass accuracy changes for different magnetic field inclinations, particularly near the equator or poles where the inclination tends towards 0° and 90° where there is no magnetic information available to an inclination compass.

B. Estimate of N

In order to guide our study to the pertinent parameter regime, we need an estimate of the number of photons N we can expect to impinge on a magnetoreceptor cell in a certain time interval. It has been previously estimated that on a cloudless, moonless night, there are 0.3 photons per μm^2 of retina per second.[81] A typical photoreceptor cell diameter is around 2 μm,[81] and the double cone photoreceptor cells (proposed as being well suited as magnetoreceptors[62,152,219]) are in an approximately hexagonal

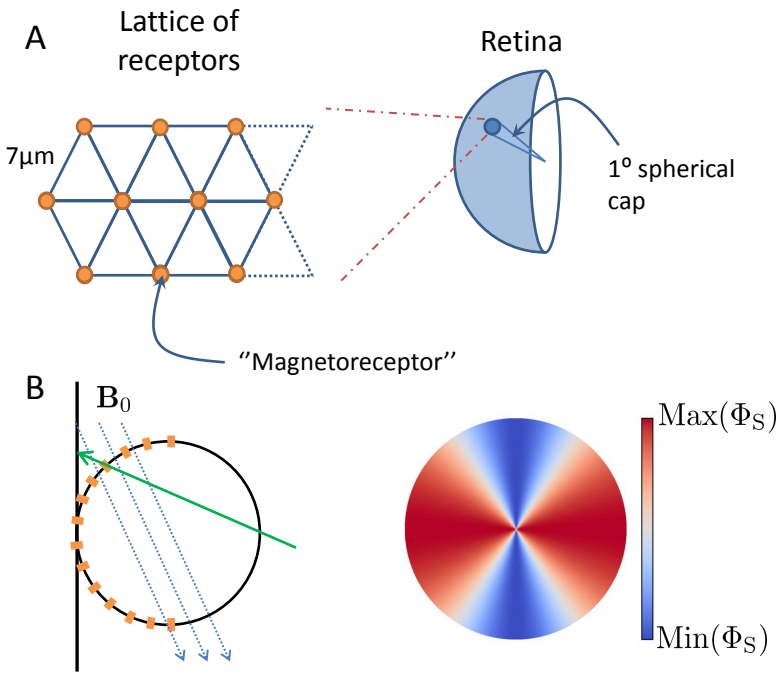


Figure 6.4: A, a schematic representation of magnetoreceptors in the retina wherein the magnetoreceptor cells are assumed to be in a hexagonal arrangement with a nearest-neighbour distance of 7 μm, and are grouped in 1° spherical caps. B, an illustration of how visual modulation patterns are constructed. With an external field vector $\mathbf{B}_0$ (blue arrows), the singlet yield at a receptor cell (orange) is projected onto a plane as an equal angle projection with the pupil at the zenith (green arrow). This is then plotted on the right, with the color of the pixel varying from blue to red denoting the singlet yield at the corresponding receptor cell.

lattice with nearest neighbour separation of 7 μm[108] (Fig. 6.4), meaning there is approximately 1 receptor cell per 10 μm^2. Putting these number together means roughly 1 photon impinges on a single double-cone photoreceptor cell per second.

Evaluating $\mathrm{I}(\Theta, \mathbf{\Phi}_S(\Theta; N))$ requires the diagonalization of a covariance matrix of dimension given by the number of magnetoreceptor cells in our model. As there are potentially tens of millions of receptors in the retina,[165] we must reduce the dimension of the system. We therefore choose to group receptor cells in 1° spherical caps of the retina (Fig. 6.4), over which we do not expect the average Φ_S to vary significantly,[27,74,165] to form a smaller number of grouped "effective magnetoreceptor cells". Each cap is then treated as a single receptor cell which absorbs the total number of photons impinging on all the constituent receptor cells.[71] The whole

ensemble of receptor cells is therefore described by a grid of these 1° spaced grouped receptor cells. It is known that similar grouping of photoreceptor cells is done at the level of the retinal ganglion cells by the visual system in low light conditions to improve contrast at the expense of resolution.[204] Since the increase in the number of photons per receptor compensates the reduction in the number of receptor cells, we consider this simplification to be valid.

To test the validity of this simplification, we have compared the lower bound error calculated using 1° and 2° receptor spacings, representing a four-fold decrease in the total number of grouped receptors and a four-fold increase in the number of photons per grouped receptor. The calculated lower bound errors agreed to within a few percent, justifying our model.

In order to calculate an estimate of N, we need to integrate the number of photons impinging on a spherical cap with angle $\frac{1}{2}^\circ$ (so that the total cap-to-cap angle is 1°). The area of a spherical cap is given by $2\pi r^2(1-\cos(\theta))$. A typical radius of a song bird eye is 4 mm,[194] meaning the area of the spherical cap is $\sim 4000\ \mu\text{m}^2$. The density of photoreceptors is $1/10\ \mu\text{m}^{-2}$. Bringing these values together with the area of a photoreceptor and the rate of photons impinging on the retina, we have a final estimate[71]

$$\begin{aligned} N\ \text{s}^{-1} &= 4000 \times \frac{1}{10} \times \pi \times 0.3 \\ &\sim 400\ \text{s}^{-1}(\text{per grouped photoreceptor}). \end{aligned} \tag{6.41}$$

Clearly, there is a time-dependence of N, as the longer the integration time, the more photons can be absorbed[204] (the shutter time in the visual system). It seems unlikely that this integration time would be much longer than a few minutes (the bird having to maintain a fixed head direction during this time), meaning the pertinent parameter regime is $10^2 \leq N \leq 10^4$.

This estimate represents a generous upper bound on the number of reaction cycles based on this level of illumination, as it assumes that the cryptochrome proteins

absorb 100% of the photons impinging on the cells, despite the presence of other light-activated proteins (i.e. opsins) in the receptor cells. Additionally, this assumes uniform illumination over different parts of the retina. Our averaging over spherical caps would to a large extent reduce the effect of point light sources (e.g. stars) which would only excite at most 1 magnetoreceptor cell. We assume that higher order effects arising from differential illumination at different points in the retina are negligible, something which could be explored in future work.

VII Model system

Having constructed the framework of our analysis, we begin with a simple parameterized model for the Φ_{S} signal which allows us to test this Information Theory approach[71] before applying it to realistic systems. If the polar and azimuthal angles defining the relative orientation of the magnetic field in the RP frame at receptor i are ζ and δ (as in Eq. 6.40), we choose the fractional singlet yield to be a negative Gaussian with mean ζ_0 which we set to be 90°, and a width which can be controlled by varying a parameter σ (Fig. 6.5D). The anisotropy of the signal is chosen to be equal to that for the 16-spin FAD-Trp spin system[74] with a reactive liftime $\tau = 1/k = 1$ μs.

$$\Phi_{\mathrm{S}}(\zeta, \delta; \zeta_0, \sigma) = 0.5 - 1.27 \times 10^{-3} \times \exp\left(-\frac{(\zeta - \zeta_0)^2}{2\sigma^2}\right). \tag{6.42}$$

Fig. 6.5A gives an example of how the singlet yield signal across the retina varies for different values of N ($\sigma = 26°$). If we consider for instance the signal for $N = 10^4$ photons per receptor, there is a significant amount of noise obscuring the signal, owing to the variance of $\Phi_{\mathrm{S}}^i(\Theta, N)$. Before considering the Information Theory lower bound, we attempt to compute the root mean squared error by some artificial data processing to assess the achievability of the bound.

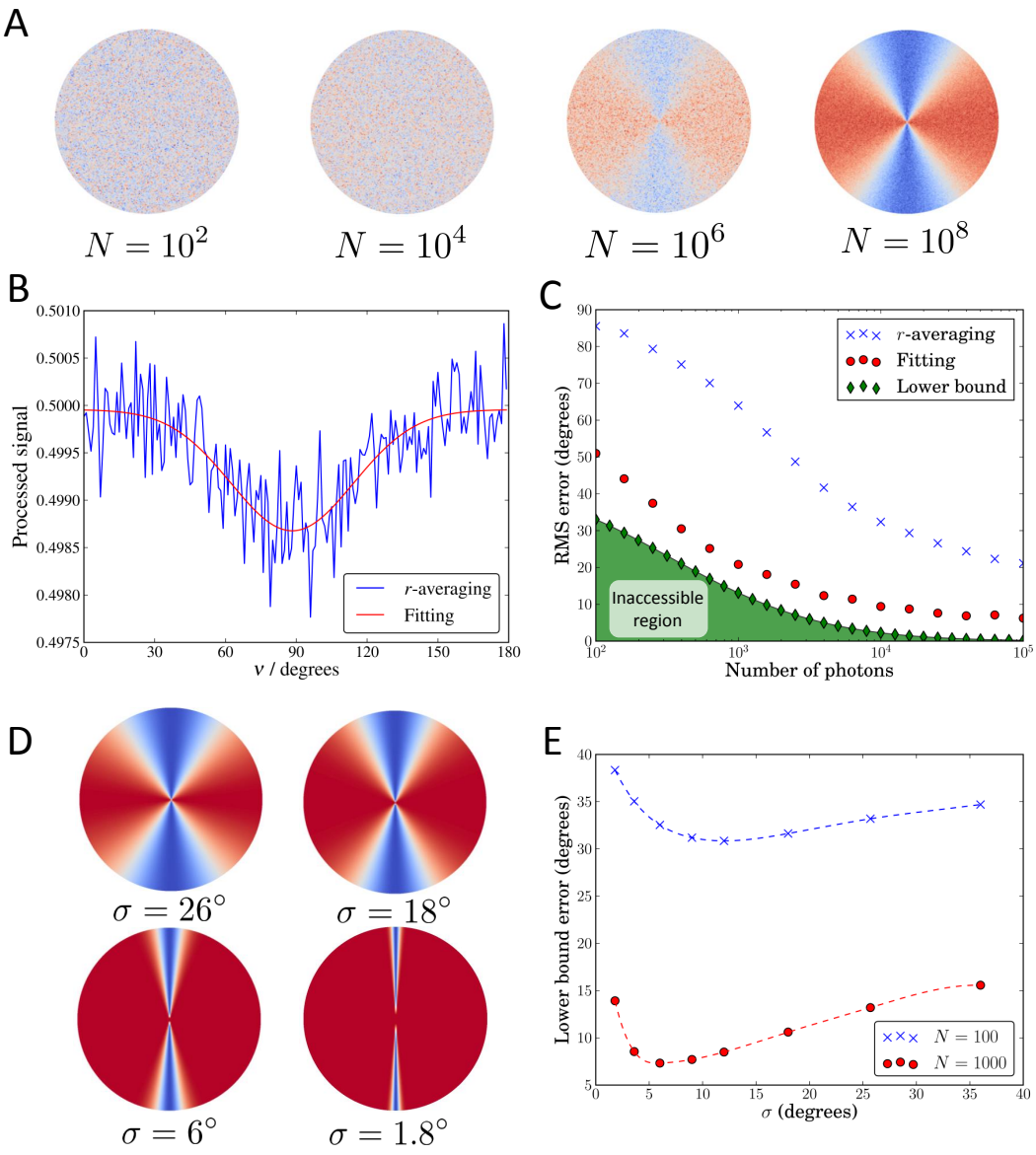


Figure 6.5: Calculating the heading error for the model system. A, Visual Modulation patterns for a range of N ($\sigma = 26°$) where each pixel represents $\Phi_S^i(\Theta, N)$ for a given i. B, example data processing on the $\mathbf{\Phi}_S(\Theta; N)$ signal for $N = 10^4$, first averaging across diameters in the VMP (labelled r-averaging) and then fitting this result for ζ_0 in the model singlet yield signal (Eq. 6.42). C, comparing the root mean squared error for the averaging and fitting methods with the Information Theory lower bound. D, VMPs in the infinite N limit for a range of σ. E, the lower bound error calculated for model Φ_S signals with varying width of the signal, parametrized by the variance of the Gaussian σ. Modified from Ref. 71.

A. Artificial data processing

We have constructed the relative orientations of RPs in the receptor cells such that, for this simple example, the signal should be constant along diameters of the VMP (Fig. 6.5D). Therefore, we choose initially to average over these diameters, and plot these averages against the polar angle in the retina (ν in Eq. 6.36) in Fig. 6.5B. We assume that the estimated field direction $\hat{\theta}$ is given by the minimum of these data, from which we can calculate the error. This procedure is then repeated for many realisations of the singlet yield signal, $\mathbf{\Phi}_{\mathrm{S}}(\Theta; N)$, and the mean-squared error calculated.

For a more sophisticated data processing, we then fit for ζ_0 in the model singlet yield signal (Eq. 6.42) using this averaged data, which gives the estimate of the field direction. Again, the way we have constructed the geometry of the system means that this should be the true result in the large N limit. Again, this is repeated many times, and the mean-squared error computed.

Fig. 6.5C compares the root-mean-squared error $\sqrt{\mathrm{E}[(\Theta - \hat{\Theta})^2]}$ from the averaging and curve fitting methods to the Information Theory lower bound. We can see that the curve fitting offers a relatively good proof of principle that the Information Theory bound is not far smaller than that achievable by a data processing algorithm we can design. Indeed, some more complex method could achieve a better agreement, but the importance of the Information Theory result is that it is a *strict* bound. On the other hand, more primitive interpretation techniques such as our averaging over diameters of the retina would give a far worse error.

B. Testing the compass needle

We can also use this model system to test how the width of the signal (Fig. 6.5D) affects the accuracy of the compass. In Chapter 4, we suggested that the very sharp singlet yield signal attainable for the FAD-Trp RP would offer better directional accuracy than a broader signal such as the FAD-Z signal.[74,160] However, Fig. 6.5E,

which plots the RMS heading error against the width of the model singlet yield for a fixed N, indicates that an arbitrarily sharp signal does not necessarily give the best accuracy of a RP compass under low light conditions. Indeed, with a limited number of photons, there is actually an optimal shape of the signal[71] to limit the error in heading. While we have yet to fully characterise this phenomenon, we tentatively suggest by way of explanation that, the smaller the value of N, the more averaging of the signal is required to generate a heading, and that broader signals are better suited to this coarse-graining than very sharp signals.

VIII Realistic Radical Pairs

Having tested our method with this toy system, we can move on to a more biologically realistic RP. As we have discussed in detail previously, there are two principal candidate cryptochrome-based RPs which are proposed as the sensing entities *in vivo*: FAD-Trp[130] and FAD-Z.[77,186] We will continue to use the same relative orientation of the RPs within the receptor cells as before, any choice being arbitrary given our ignorance about the configuration of the sensing proteins *in vivo*.

A. Comparing radical pairs

As we have detailed previously, there is circumstantial or inconclusive experimental evidence for both of these RPs. From a computational point of view, we discussed in Chapter 4 that, while FAD-Z offers a much larger anisotropy,[77] FAD-Trp can give a much sharper signal[74] (though perhaps in unrealistic parameter regimes) meaning there is no general consensus over which RP is more viable as the *in vivo* sensor from simple calculations. We asserted in our discussion in Chapter 4 that the sharp signal of the FAD-Trp RP means that it would offer a much more accurate compass bearing than the slowly varying FAD-Z signal. Here, we can test whether this is indeed true under low light conditions.

Fig. 6.6A shows the lower bound error calculated for three RP lifetimes of the FAD-Trp RP.[71] Referring back to Fig. 4.2, as the lifetime increases, the singlet yield signal exhibits both an increase in anisotropy and the appearance of the compass "needle"[74] for $\tau \geq 5$ μs. Therefore, it is unsurprising that the bound is lower for the longer lived RPs. Not shown are the results for FAD-Z, where this bound is essentially 0° for any $N \geq 100$. This indicates that, despite the slowly varying signal, FAD-Z could potentially offer a more accurate compass sense under low light conditions. However, if τ for the FAD-Trp RP is extended to 100 μs and longer, the signal is much sharper and again the bound is essentially 0° for $N \geq 100$.

However, this improvement in compass performance can equally be attributed to the increased anisotropy in the Φ_S signal on increasing the RP lifetime, which in turn improves the signal to noise ratio. As Fig. 6.5E indicates, under low light conditions, it is perhaps naïve to assume that an arbitrarily sharp direction dependence offers the best accuracy. Additionally, as discussed in Section 4.IV, RP lifetimes of this length are thought to be unrealistic because spin relaxation mechanisms would abolish the coherent oscillations in the spin dynamics at long times,[95,218] swamping any direction dependence of the reaction yield.

B. Full FAD-Trp system

One important point to mention is that the results discussed to this point have been calculated using the truncated 16-spin model of the FAD-Trp spin system used previously[116] (see Section 4.II). The reason for this is that, as outlined in Chapter 2, the computational difficulty of spin dynamics calculations scales exponentially, and for larger spin systems becomes too costly. Additionally, we have neglected dipolar and exchange interactions between the radicals, again as this reduces the cost of the calculation. However, it is generally found that both increasing the number of nuclei and including radical-radical interactions in the calculation generally reduces the size of the signal anisotropy.[124]

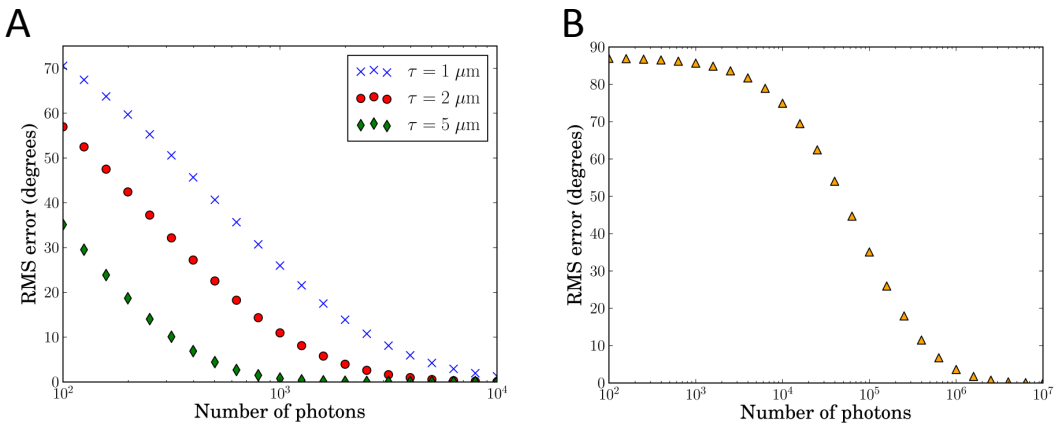


Figure 6.6: The lower bound error in heading accuracy for the FAD-Trp radical pair. A, for the truncated 16-spin model with no exchange or dipolar coupling. The data are labelled by the RP recombination lifetime $\tau = 1/k$. B, for the full 30-spin model with $\tau = 1$ μs. Modified from Ref. 71.

While calculation of the full 30-spin RP including exchange and dipolar interactions is not feasible using an exact quantum mechanical method, it is possible to perform approximate calculations on spin systems of this size using the semi-classical algorithm described in Ref. 132. Using results calculated by Alan Lewis and presented in his thesis (Ref. 124), we can expand our analysis to an approximate (there is an estimated 5% statistical error in the semi-classical results) description of the full FAD-Trp spin system including exchange and dipolar interactions appropriate for the separation and relative orientation of the FAD-Trp radicals in *Dm*CRY[122,225] ($\tau = 1$ μs).

This calculation reveals a decrease in the anisotropy of the signal in going from 14 nuclear spins to 28 of over an order of magnitude (Table 6.1). As expected, this decrease in the signal anisotropy in mirrored in the calculated RMS error (Fig. 6.6B), which shows that the error is large even for $N \geq 10^5$ photons per grouped receptor,[71] a serious problem for the operation of an FAD-Trp-based compass under low light conditions.

Radical Pair	No. of nuclei	τ (μs)	Max $[\Phi_S]$ - Min $[\Phi_S]$	$\sqrt{\epsilon^2}$ ($N = 10^3$)
FAD-Trp	7 + 7	1	1.27×10^{-3}	26°
FAD-Trp	7 + 7	5	3.69×10^{-3}	0.77°
FAD-Trp	15 + 13	1	9.77×10^{-5}	86°
FAD-Z	7 + 0	1	1.46×10^{-1}	$\sim 0°$
FAD-Asc	7 + 4	1	6.66×10^{-2}	$\sim 0°$

Table 6.1: The absolute size of the anisotropy and RMS heading error for $N = 10^3$ for a series of RP models.

An alternative RP?

It therefore seems that a different RP would be better suited to low light conditions. If we consider different potential counter radicals with the $FAD^{\bullet-}$ radical, evidently the $Z^{\bullet}$ radical would be a good option. However, as described previously,[77,89,90] there are a number of reservations about the involvement of this hypothetical radical in biological conditions. A small organic radical such as the ascorbate radical[116,150] could offer a better option. If we include a rapidly tumbling $Asc^{\bullet-}$ radical (hyperfine parameters in Appendix A) with the $FAD^{\bullet-}$ radical, we find that the anisotropy of the signal increases by a factor of around 50 compared to the FAD-Trp RP. This again leads to a very small heading error (Table 6.1), and confirms the idea that a small organic radical could prove to be a better counter radical for a magneto-sensing RP *in vivo*. However, the involvement of such a counter radical in the context of cryptochrome-based magnetoreception remains conjecture and the details of a proposed mechanism including an ascorbate (or similar) radical are only speculative.[150] Additionally, for both FAD-Z and FAD-Asc RPs, we might expect a similar decrease in anisotropy as observed for the FAD-Trp RP on inclusion of all the nuclear spins in the FAD radical and, in particular, radical-radical interactions, which could similarly reduce the accuracy of a compass based on these RPs.

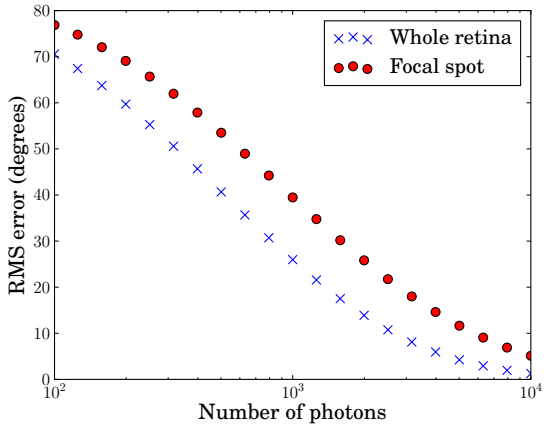


Figure 6.7: Comparing the lower bound error when the entire retina is uniformly illuminated ("whole retina") with the error when the photons are focussed onto the central 1% of the retina ("focal spot") for the FAD-Trp radical pair with a lifetime of $\tau = 1$ μs. The total number of photons in both calculations is constant, meaning the number of photons per receptor in the "focal spot" is 100 times that of the whole retina.

C. Focal point

One final aspect of our approach that deserves some attention is our assumption of uniform illumination over the retina. It may seem as though focussing the light onto a smaller area of the retina, which would reduce the uncertainty at a given receptor, would improve the accuracy of the RP compass. One simple test of this idea is to consider a system in which all of the photons entering the eye are focussed on to just a fraction of the entire retina. As a proof of principle, we choose the area of interest to be the central 1% of the retina i.e. a spherical cap defined by an angle of $\sim 8°$ such that its area is 1% that of the entire retina, onto which 100 times as many photons impinge. The singlet yield signal used is then only from this focal area of the retina, and we use this signal to compute the lower bound error and compare against the error as calculated previously.

Fig. 6.7 shows the results of calculations using this scheme of concentrating photons on to a central "focal spot" for the FAD-Trp RP with $\tau = 1$ μs. The results indicate that uniform illumination over the entire retina actually gives a *better* compass accuracy than this focussing scheme. This can be attributed to the

fact that, in focussing the photons over a small area, the increase in the number of photons per receptor is undone by having fewer receptors. As these receptors are concentrated about only a small area of the retina, the relative field direction and therefore the singlet yield signal varies only by a small amount in this focal region. As our approach offers a lower bound for any arbitrarily complex signal processing, we can see that an averaging scheme using the signal from the entire retina, over which the signal anisotropy will be larger, gives a smaller heading error than simply concentrating photons onto a small area of the retina.

IX Conclusions

It should be stressed that the lower bound we have calculated in this chapter represents the very best case scenario in many ways. Not only is it a *strict* lower bound of the error for even the most efficient possible processing of the signal from which to estimate the heading,[30] it assumes a 100% absorption efficiency of photons by CRY proteins despite the presence of other photo-active proteins in the photoreceptor cells. If even with these generous assumptions, the FAD-Trp RP seems ill suited to operating under low light conditions[71] unless the integration time over which the signal was averaged were incredibly long (> an hour), this raises serious questions over its involvement *in vivo*.

Not only this, but we have also not included any possible intrinsic noise in the signalling cascade. Not wanting to make any assumptions about the signal transduction, we have not considered, for instance, noise arising from thermal activation of the protein to the signalling state (a review of noise in the nervous system is given in Ref. 46). Additionally, our analysis has assumed perfect orientation of the CRY proteins within the receptor cells. If there were some static disorder of the proteins,[115] this could be another source of noise in the signal.

In summary, we have investigated how a RP compass would function under low light conditions, and how the quantum noise introduced by the small number of

available photons affects the accuracy of a RP compass under different conditions.[71] Our analysis suggests that the FAD-Trp RP would be poorly suited as the basis of a RP compass operating in low light conditions because of the very small signal it generates, unless the time integration in generating a heading estimate were exceedingly long. Not only this, but the fact that such small levels of noise can have a significant impact on the functioning of the compass may suggest that other sources of noise in the mechanism could be significant, and could form the basis of further study.

Assuming that our estimations for the magnitude of the noise are not grossly inaccurate, there are a number of *possible* conclusions to take from this work:

- This analysis argues against FAD-Trp as the sensing RP, and instead there is some other RP involved in the mechanism *in vivo*. This could involve the hypothesised $Z^{\bullet}$ radical,[77] or a small organic radical such as the ascorbate radical[116,150] as counter radicals to $FAD^{\bullet-}$. These RPs may exhibit larger signal anisotropies, though their realisation *in vivo* is currently unknown.

- Alternatively, there could be some unknown aspect of the mechanism that we are missing which allows a RP compass to operate even under noisy conditions. Perhaps this could be related to our conclusion in the previous chapter that there is some unknown aspect of the mechanism leads to a RP compass being exceptionally sensitive to weak radio frequency magnetic fields.

- Relatedly, the signal anisotropy could be boosted by some modification to the RP mechanism, making the RP compass more robust to noise. For instance, Ref. 94 suggests that a spin-selective scavenging side-reaction can greatly increase the anisotropy of the singlet yield signal available from a RP.

Acknowledgements

The idea of using a Shannon information theory approach to analyse the performance of a RP compass under low light conditions was developed in collaboration with Tom Hiscock. The proof of Eq. 6.2 was provided by Oliver Riordan and the kinetic Monte Carlo verification was guided by Daniel Kattnig. Thomas Scrivener provided a check of the derivation of Eq. 6.33 and separately verified the distribution of $\Phi_{\mathrm{S}}(N)$. Peter Hore and David Manolopoulos helped to improve the notation throughout this chapter, and contributed to the discussion of results. The approximate calculation of Φ_{S} for the full FAD-Trp system was performed by Alan Lewis and is presented in his DPhil thesis.[124]

Chapter 7

Conclusions

The radical pair hypothesis of magnetoreception has prompted a great deal of study, investigating the possibility that this sensory system could be based on an unambiguously quantum mechanical mechanism.[4,19,56,74,116,159,177,224] While the body of behavioural evidence supporting this hypothesis is growing,[130,167,207,209] complementary theoretical and computational studies are currently inconclusive, in no small part owing to the complexity of the problem.

In this thesis, we have presented some novel algorithms which greatly increase the efficiency of RP simulations in both static and time-dependent magnetic fields. While these methods have facilitated calculations of spin systems that are larger than previously possible,[72,74] therefore offering a more accurate description of the spin dynamics in the RP, there are still a number of limitations that reduce the potential importance of our conclusions. For instance, being unable to include radical-radical exchange and dipolar coupling in a spin system including more than $\sim$8 nuclei is a serious drawback of these methods. While the semiclassical method presented in Ref. 125 offers a way of circumventing this, there is some evidence[123] that this method cannot capture certain quantum phenomena in the spin dynamics. The long-standing challenge of simulating a system including as many coupled spins as possible[132] remains one of the primary areas for further work in the field.

The other obvious factor neglected in our calculations is spin relaxation. Again,

this an area of very active research,[95,218] the computational challenge of simulating a large spin system only being exacerbated by including spin relaxation. This is of particular importance if we are considering long-time phenomena in the RP. Both the "spike" in the singlet yield[74] presented in Chapter 4 and the resonance effects[73] suggested in Chapter 5 as being responsible for the disruption of birds' magnetic orientation by radio frequency magnetic fields[43,167,168,179] rely on spin coherence lifetimes considerably longer than thought achievable in biological systems.[81,97] However, without a suitable method for including spin relaxation mechanisms in these calculations, any conclusions we draw from the results can only be tentative. In particular, the derivation of a novel algorithm which could account for spin relaxation in the presence of a time-dependent external field is an important avenue for further work.

Having said this, our Floquet theory-based method[72] presented in Chapter 3 has allowed us to progress from the largely simplified calculations of RPs in the presence of time-dependent magnetic fields presented previously,[56,203,220] and our results offer new and potentially important insights.[73] Our analysis of the sometimes contradictory experimental results in Chapter 5 confirmed the suggestion[97] that the field strengths used in the behavioural studies are so small that extraordinarily long spin coherence lifetimes would be required for the RPs to be sensitive to such weak magnetic fields.[73] It appears therefore that either the RP model is incomplete, and some unknown aspect of the mechanism leads to greatly increased sensitivity to time-dependent fields, or that there is some systematic artifact present in all the behavioural studies. Interpretation of these behavioural results remains one of the primary open questions in the field.

One consistent theme in this thesis has been the comparison of the two candidate sensing RPs: FAD-Trp[130] and FAD-Z.[77,186] First, in Chapter 4, we compared the shapes of the singlet yield signal arising from the two candidate RPs. While the FAD-Z system would offer a much larger signal anisotropy, under certain conditions

we found that FAD-Trp could offer a very sharp signal, which it has been suggested could offer very good directional accuracy.[74] However, the spike feature is very sensitive to radical-radical coupling and spin relaxation, meaning this behaviour is unlikely to be relevant for realistic RPs. On the other hand, there has been some suggestion that the proposed Z radical, superoxide $O_2^{\bullet -}$, is unsuitable as the counter radical.[77,89,90] The rationale is that the strong spin-orbit coupling expected in superoxide would lead to very efficient spin relaxation, rendering the FAD-Z radical pair insensitive to an external magnetic field.

In Chapter 5 we attempted to address the contradictory behavioural evidence around the magnetic disorientation of birds in the presence[43,167,168,179] of time-dependent fields in reference to the two candidate RPs. The disparity in the experimental results centres around whether a single-frequency RF magnetic field oscillating at the Larmor frequency[167,168] or broadband noise magnetic fields[43,179] are more effective at disrupting the biological magnetic compass. We found that the conflicting experimental results were each compatible with one of the candidate RP sensors. The FAD-Z radical pair would be particularly sensitive to a Larmor frequency oscillatory field, whereas a RP in which both radicals have many nuclei with non-zero spin would be more sensitive to band-limited noise.[73] While the broadband noise magnetic field effect is more general, the Larmor frequency perturbation on the FAD-Z signal is more significant and more easily rationalised as causing disruption of the RP compass. We suggested a number of experiments to try to distinguish between the two candidate RPs which would also offer significant evidence for our interpretation of the experimental results in the framework of the RP mechanism. We also put forward a number of experimental protocols with a view to improving the reproducibility of future behavioural studies. These experiments could prove pivotal to elucidating the details of the *in vivo* mechanism, and represent a very important area for further work.

Finally, in Chapter 6 we considered the performance of the FAD-Trp and FAD-Z

radical pairs under low light conditions, where the limited number of reaction cycles introduces an uncertainty into the singlet yield.[71] It appears that the far greater signal anisotropy of FAD-Z is more robust to the quantum noise inherent in the RP mechanism than the small, albeit more sharply peaked, signal of FAD-Trp. Indeed, it appears that the FAD-Trp radical pair is particularly poorly suited to functioning under low light conditions, perhaps having serious implications for its relevance to the *in vivo* sensing mechanism. As has been considered in several studies,[94,124] the absolute size of the signal available from a RP sensor is highly significant, and further study should be devoted to a complete description of a RP system which could offer a large signal anisotropy. The Information theory-based technique[71,180] used in this chapter could also in future be extended to consider the effect of other sources of noise on a RP compass, such as static disorder of the sensing proteins, or thermal noise.

Appendix A

Hyperfine tensors

I FAD Radical

The hyperfine tensors of the FAD radical anion were calculated using density functional theory (DFT) in Gaussian-03[53] at the UB3LYP/EPR-III level.[169] For the H8 and H7 methyl groups are assumed to rotate quickly enough to average the hyperfine tensors of the three protons, and their anisotropic components are very small and are therefore neglected. The Hβ protons were assigned isotropic hyperfine couplings equal to the largest of the components for the methyl group in lumiflavin.[116]

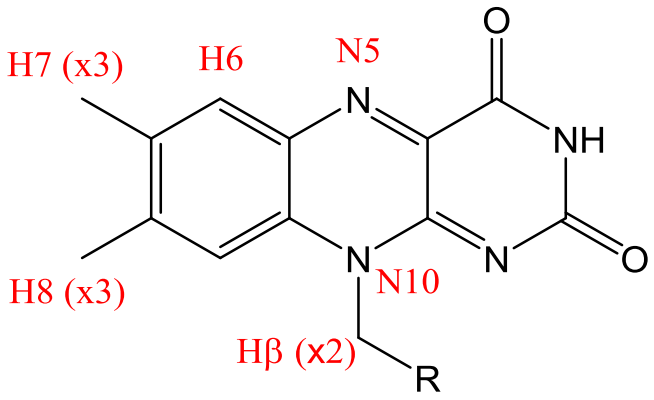


Figure A.1: Nucleus labels of FAD radical in DFT calculations.

Nucleus	**A** mT	a_{iso} mT	T_{qq} mT
N5	$\begin{pmatrix} -0.0989 & 0.0039 & 0.0 \\ 0.0039 & -0.0881 & 0.0 \\ 0.0 & 0.0 & 1.7569 \end{pmatrix}$	0.5233	1.2336 −0.6101 −0.6234
N10	$\begin{pmatrix} -0.0190 & -0.0048 & 0.0 \\ -0.0048 & -0.0196 & 0.0 \\ 0.0 & 0.0 & 0.6046 \end{pmatrix}$	0.1887	0.4159 −0.2031 −0.2128
H6	$\begin{pmatrix} -0.2569 & -0.1273 & 0.0 \\ -0.1273 & -0.4711 & 0.0 \\ 0.0 & 0.0 & -0.4336 \end{pmatrix}$	-0.3872	0.1896 −0.0464 −0.1432
H8 (×3)	$\begin{pmatrix} 0.4399 & 0.0 & 0.0 \\ 0.0 & 0.4399 & 0.0 \\ 0.0 & 0.0 & 0.4399 \end{pmatrix}$	0.4399	0.0 0.0 0.0
Hβ (×2)	$\begin{pmatrix} 0.4070 & 0.0 & 0.0 \\ 0.0 & 0.4070 & 0.0 \\ 0.0 & 0.0 & 0.4070 \end{pmatrix}$	0.4070	0.0 0.0 0.0
H7 (×3)	$\begin{pmatrix} -0.1416 & 0.0 & 0.0 \\ 0.0 & -0.1416 & 0.0 \\ 0.0 & 0.0 & -0.1416 \end{pmatrix}$	-0.1416	0.0 0.0 0.0

Table A.1: Hyperfine tensors (**A**) for the $FAD^{\bullet-}$ radical.[116] The isotropic (a_{iso} mT) and anisotropic (T_{qq} mT) interactions are given.

II Tryptophan Radical

The hyperfine tensors of the Tryptophan anion were calculated using DFT in Gaussian-03[53] at the UB3LYP/EPR-III level.[169] These tensors are in the same axis system as the FAD radical as above, appropriate for the relative orientation of the FAD cofactor and Trp-342 in the crystal structure of *Dm*CRY.[122,225] The rotation matrix which maps the axes of the FAD and Trp radicals is

$$R = \begin{pmatrix} -0.3454 & 0.6869 & -0.6395 \\ -0.8269 & 0.0995 & 0.5535 \\ 0.4438 & 0.7199 & 0.5336 \end{pmatrix} \tag{A.1}$$

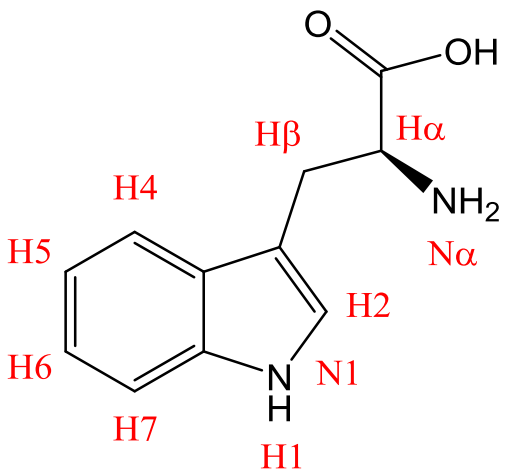


Figure A.2: Nucleus labels of Trp radical in DFT calculations.

Nucleus	**A** mT			a_{iso} mT	T_{qq} mT
N1	−0.0336	0.0924	−0.1354	0.3215	0.7596
	0.0924	0.3303	−0.5318		−0.3745
	−0.1354	−0.5318	0.6680		−0.3851

H1	$\begin{pmatrix} -0.9920 & -0.2091 & -0.2003 \\ -0.2091 & -0.2631 & 0.2803 \\ -0.2003 & 0.2803 & -0.5398 \end{pmatrix}$	-0.5983	0.5914 −0.1071 −0.4843
H2	$\begin{pmatrix} -0.2843 & 0.1757 & 0.1525 \\ 0.1757 & -0.2798 & 0.0975 \\ 0.1525 & 0.0975 & -0.2699 \end{pmatrix}$	-0.2780	0.2855 −0.0919 −0.1936
H4	$\begin{pmatrix} -0.5596 & -0.1956 & -0.1657 \\ -0.1956 & -0.4020 & 0.0762 \\ -0.1657 & 0.0762 & -0.5021 \end{pmatrix}$	-0.4880	0.3001 −0.0480 −0.2520
H6	$\begin{pmatrix} -0.0506 & 0.0622 & 0.0889 \\ 0.0622 & -0.3100 & -0.0297 \\ 0.0889 & -0.0297 & 0.2642 \end{pmatrix}$	-0.2083	0.1979 −0.0494 −0.1485
H7	$\begin{pmatrix} -0.4355 & -0.1541 & -0.1239 \\ -0.1541 & -0.2777 & 0.0864 \\ -0.1239 & 0.0864 & -0.3770 \end{pmatrix}$	-0.3636	0.2540 −0.0594 −0.1945
Hβ1	$\begin{pmatrix} 1.5808 & -0.0453 & -0.0506 \\ -0.0453 & 1.5575 & 0.0988 \\ -0.0506 & 0.0988 & 1.6752 \end{pmatrix}$	1.6046	0.1521 −0.0456 −0.1065
Hα	$\begin{pmatrix} -0.0601 & 0.0037 & 0.0331 \\ 0.0037 & -0.0251 & 0.0111 \\ 0.0331 & 0.0111 & -0.1940 \end{pmatrix}$	-0.0931	−0.1092 0.0395 0.0698
Nα	$\begin{pmatrix} 0.1295 & -0.0134 & 0.0075 \\ -0.0134 & 0.1729 & -0.0249 \\ 0.0075 & -0.0249 & 0.1371 \end{pmatrix}$	0.1465	−0.0224 −0.0270 0.0431
Hβ2	$\begin{pmatrix} 0.1634 & -0.0230 & -0.0064 \\ -0.0230 & -0.0082 & 0.0158 \\ -0.0064 & 0.0158 & -0.0182 \end{pmatrix}$	0.0457	−0.0758 −0.0454 0.1211

H5	$\begin{pmatrix} 0.0051 & 0.0616 & 0.0694 \\ 0.0616 & -0.0665 & 0.0391 \\ 0.0694 & 0.0391 & -0.0586 \end{pmatrix}$	-0.0400	$\begin{matrix} -0.0632 \\ -0.0616 \\ 0.1248 \end{matrix}$

Table A.2: Hyperfine tensors ($\mathbf{A}$) for the $Trp^{\bullet+}$ radical.[116] The isotropic (a_{iso} mT) and anisotropic (T_{qq} mT) interactions are given.

III Experimentally measured components

Flavin radical	Protein	Reference	Nucleus	$A_{xx} = A_{yy}$	A_{zz}
neutral	*Anabarna* flavodoxin	134	N10	3±1	31 ± 1
neutral	*Anabarna* ferredoxin				
	$NADP^+$ reductase	133	N10	2.7 ± 1.3	29.7 ± 1.9
neutral	Na^+ translocating				
	NADH:quinone		N5	0.2 ± 2.0	52.5 ± 0.5
	oxidoreductase				
	Vibrio cholerae	6	N10	2.0 ± 1.0	28.9 ± 0.6
anionic	Na^+ translocating				
	NADH:quinone		N5	2.3 ± 0.6	57.6 ± 0.5
	oxidoreductase				
	Vibrio cholerae	6	N10	1.6 ± 0.6	22.8 ± 0.6

Table A.3: Hyperfine tensor components of flavin radicals as found experimentally. The signs of the components were not determined.

IV Ascorbate Radical

Nucleus	**A** mT	a_{iso} mT	T_{qq} mT
H1	$\begin{pmatrix} 0.176 & 0.0 & 0.0 \\ 0.0 & 0.176 & 0.0 \\ 0.0 & 0.0 & 0.176 \end{pmatrix}$	0.176	0.0 0.0 0.0
H2	$\begin{pmatrix} 0.019 & 0.0 & 0.0 \\ 0.0 & 0.019 & 0.0 \\ 0.0 & 0.0 & 0.019 \end{pmatrix}$	0.019	0.0 0.0 0.0
H3 (×2)	$\begin{pmatrix} 0.007 & 0.0 & 0.0 \\ 0.0 & 0.007 & 0.0 \\ 0.0 & 0.0 & 0.007 \end{pmatrix}$	0.007	0.0 0.0 0.0

Table A.4: Hyperfine tensors (**A**) for the $Asc^{\bullet -}$ radical.[92] The isotropic (a_{iso} mT) and anisotropic (T_{qq} mT) interactions are given.

Bibliography

[1] K. P. Able and M. A. Able. Daytime calibration of magnetic orientation in a migratory bird requires a view of skylight polarization. *Nature*, 364(6437):523, 1993.

[2] S. Åkesson, J. Morin, R. Muheim, and U. Ottosson. Avian orientation at steep angles of inclination: experiments with migratory white–crowned sparrows at the magnetic North Pole. *Proceedings of the Royal Society of London B: Biological Sciences*, 268(1479):1907–1913, 2001.

[3] P. W. Atkins and R. S. Friedman. *Molecular quantum mechanics*. Oxford university press, 2011.

[4] J. N. Bandyopadhyay, T. Paterek, and D. Kaszlikowski. Quantum coherence and sensitivity of avian magnetoreception. *Physical review letters*, 109(11):110502, 2012.

[5] J. C. T. Barnard. Asymmetric Reaction in Radical Pair Compass Magnetoreception. Master's thesis, University of Oxford, 2016.

[6] B. Barquera, J. E. Morgan, D. Lukoyanov, C. P. Scholes, R. B. Gennis, and M. J. Nilges. X-and W-Band EPR and Q-Band ENDOR Studies of the Flavin Radical in the Na+-Translocating NADH: Quinone Oxidoreductase from Vibrio c holerae. *Journal of the American Chemical Society*, 125(1):265–275, 2003.

[7] O. Bazalova, M. Kvicalova, T. Valkova, P. Slaby, P. Bartos, R. Netusil, K. Tomanova, P. Braeunig, H.-J. Lee, I. Sauman, et al. Cryptochrome 2 mediates directional magnetoreception in cockroaches. *Proceedings of the National Academy of Sciences*, 113(6):1660–1665, 2016.

[8] R. Beason and P. Semm. Does the avian ophthalmic nerve carry magnetic navigational information? *Journal of Experimental Biology*, 199(5):1241–1244, 1996.

[9] N. J. Beaudry and R. Renner. An intuitive proof of the data processing inequality. *arXiv preprint arXiv:1107.0740*, 2011.

[10] C. M. Bender and G. V. Dunne. Large-order perturbation theory for a non-Hermitian PT-symmetric Hamiltonian. *Journal of Mathematical Physics*, 40(10):4616–4621, 1999.

[11] D. P. Bertsekas and J. N. Tsitsiklis. *Introduction to probability*, volume 1. Athena Scientific Belmont, MA, 2002.

[12] T. Biskup, E. Schleicher, A. Okafuji, G. Link, K. Hitomi, E. D. Getzoff, and S. Weber. Direct observation of a photoinduced radical pair in a cryptochrome blue-light photoreceptor. *Angewandte Chemie International Edition*, 48(2):404–407, 2009.

[13] P. Bolte, F. Bleibaum, A. Einwich, A. Günther, M. Liedvogel, D. Heyers, A. Depping, L. Wöhlbrand, R. Rabus, U. Janssen-Bienhold, et al. Localisation of the putative magnetoreceptive protein cryptochrome 1b in the retinae of migratory birds and homing pigeons. *PLoS One*, 11(3):e0147819, 2016.

[14] G. E. Box, W. G. Hunter, J. S. Hunter, et al. Statistics for experimenters. 1978.

[15] R. N. Bracewell and R. N. Bracewell. *The Fourier transform and its applications*, volume 31999. McGraw-Hill New York, 1986.

[16] H.-P. Breuer and F. Petruccione. *The theory of open quantum systems*. Oxford University Press on Demand, 2002.

[17] B. Brocklehurst and K. A. McLauchlan. Free radical mechanism for the effects of environmental electromagnetic fields on biological systems. *International journal of radiation biology*, 69(1):3–24, 1996.

[18] J. G. Bryan and G. P. Wadsworth. Introduction to probability and random variables. 1960.

[19] J. Cai, G. G. Guerreschi, and H. J. Briegel. Quantum control and entanglement in a chemical compass. *Physical review letters*, 104(22):220502, 2010.

[20] F. Cailliez, P. Muller, T. Firmino, P. Pernot, and A. de la Lande. Energetics of photoinduced charge migration within the tryptophan tetrad of an animal (6–4) photolyase. *Journal of the American Chemical Society*, 138(6):1904–1915, 2016.

[21] A. Carrillo, M. F. Cornelio, and M. C. de Oliveira. Environment-induced anisotropy and sensitivity of the radical pair mechanism in the avian compass. *Physical Review E*, 92(1):012720, 2015.

[22] A. R. Cashmore, J. A. Jarillo, Y.-J. Wu, and D. Liu. Cryptochromes: blue light receptors for plants and animals. *Science*, 284(5415):760–765, 1999.

[23] T. Charpentier, C. Fermon, and J. Virlet. Efficient time propagation technique for MAS NMR simulation: Application to quadrupolar nuclei. *Journal of Magnetic Resonance*, 132(2):181–190, 1998.

[24] N. Chernetsov, A. Pakhomov, D. Kobylkov, D. Kishkinev, R. A. Holland, and H. Mouritsen. Migratory Eurasian reed warblers can use magnetic declination to solve the longitude problem. *Current Biology*, 27(17):2647–2651, 2017.

[25] S.-I. Chu and D. A. Telnov. Beyond the Floquet theorem: generalized Floquet formalisms and quasienergy methods for atomic and molecular multiphoton processes in intense laser fields. *Physics reports*, 390(1-2):1–131, 2004.

[26] A. Chulliat, S. Macmillan, P. Alken, C. Beggan, M. Nair, B. Hamilton, A. Woods, V. Ridley, S. Maus, and A. Thomson. The US/UK world magnetic model for 2015-2020. 2015.

[27] F. Cintolesi, T. Ritz, C. Kay, C. Timmel, and P. Hore. Anisotropic recombination of an immobilized photoinduced radical pair in a 50-μT magnetic field: a model avian photomagnetoreceptor. *Chemical Physics*, 294(3):385–399, 2003.

[28] W. W. Cochran, H. Mouritsen, and M. Wikelski. Migrating songbirds recalibrate their magnetic compass daily from twilight cues. *Science*, 304(5669):405–408, 2004.

[29] V. Courtillot and J. L. Le Mouel. Time variations of the Earth's magnetic field: from daily to secular. *Annual Review of Earth and Planetary Sciences*, 16(1):389–476, 1988.

[30] T. M. Cover and J. A. Thomas. *Elements of information theory*. John Wiley & Sons, 2012.

[31] A. Davila, G. Fleissner, M. Winklhofer, and N. Petersen. A new model for a magnetoreceptor in homing pigeons based on interacting clusters of superparamagnetic magnetite. *Physics and Chemistry of the Earth, Parts A/B/C*, 28(16-19):647–652, 2003.

[32] A. Dellis and I. Kominis. The quantum Zeno effect immunizes the avian compass against the deleterious effects of exchange and dipolar interactions. *Biosystems*, 107(3):153–157, 2012.

[33] P. A. Dirac. The quantum theory of the electron. *Proc. R. Soc. Lond. A*, 117(778):610–624, 1928.

[34] P. A. M. Dirac. *The principles of quantum mechanics*. Number 27. Oxford university press, 1981.

[35] C. A. Dodson, P. Hore, and M. I. Wallace. A radical sense of direction: signalling and mechanism in cryptochrome magnetoreception. *Trends in biochemical sciences*, 38(9):435–446, 2013.

[36] P. O. Dunn and D. W. Winkler. Climate change has affected the breeding date of tree swallows throughout North America. *Proceedings of the Royal Society of London B: Biological Sciences*, 266(1437):2487–2490, 1999.

[37] A. Eckardt and E. Anisimovas. High-frequency approximation for periodically driven quantum systems from a Floquet-space perspective. *New journal of physics*, 17(9):093039, 2015.

[38] M. Edén, Y. K. Lee, and M. H. Levitt. Efficient simulation of periodic problems in NMR. application to decoupling and rotational resonance. *Journal of Magnetic Resonance, Series A*, 120(1):56–71, 1996.

[39] O. Efimova and P. Hore. Role of exchange and dipolar interactions in the radical pair model of the avian magnetic compass. *Biophysical Journal*, 94(5):1565–1574, 2008.

[40] S. T. Emlen. Migratory orientation in the indigo bunting, passerina cyanea: part i: evidence for use of celestial cues. *The Auk*, 84(3):309–342, 1967.

[41] S. T. Emlen and J. T. Emlen. A technique for recording migratory orientation of captive birds. *The Auk*, 83(3):361–367, 1966.

[42] C. Engelhard, X. Wang, D. Robles, J. Moldt, L.-O. Essen, A. Batschauer, R. Bittl, and M. Ahmad. Cellular metabolites enhance the light sensitivity of Arabidopsis cryptochrome through alternate electron transfer pathways. *The Plant Cell*, 26(11):4519–4531, 2014.

[43] S. Engels, N.-L. Schneider, N. Lefeldt, C. M. Hein, M. Zapka, A. Michalik, D. Elbers, A. Kittel, P. Hore, and H. Mouritsen. Anthropogenic electromagnetic noise disrupts magnetic compass orientation in a migratory bird. *Nature*, 509(7500):353, 2014.

[44] W. L. Engels. Day-length and termination of photorefractoriness in the annual testicular cycle of the transequatorial migrant dolichonyx (the bobolink). *The Biological Bulletin*, 123(1):94–104, 1962.

[45] R. R. Ernst, G. Bodenhausen, A. Wokaun, et al. *Principles of nuclear magnetic resonance in one and two dimensions*, volume 14. Clarendon Press Oxford, 1987.

[46] A. A. Faisal, L. P. Selen, and D. M. Wolpert. Noise in the nervous system. *Nature reviews neuroscience*, 9(4):292, 2008.

[47] U. Fano. Description of states in quantum mechanics by density matrix and operator techniques. *Reviews of Modern Physics*, 29(1):74, 1957.

[48] T. P. Fay, L. P. Lindoy, and D. E. Manolopoulos. Spin-selective electron transfer reactions of radical pairs: beyond the Haberkorn master equation. *In preparation.*

[49] G. Fedele, E. W. Green, E. Rosato, and C. P. Kyriacou. An electromagnetic field disrupts negative geotaxis in Drosophila via a CRY-dependent pathway. *Nature communications*, 5:4391, 2014.

[50] G. Feenders, M. Liedvogel, M. Rivas, M. Zapka, H. Horita, E. Hara, K. Wada, H. Mouritsen, and E. D. Jarvis. Molecular mapping of movement-associated areas in the avian brain: a motor theory for vocal learning origin. *PLoS One*, 3(3):e1768, 2008.

[51] G. Floquet. Sur les equations differentielles lineaires. *Ann. ENS [2]*, 12(1883):47–88, 1883.

[52] L. E. Foley, R. J. Gegear, and S. M. Reppert. Human cryptochrome exhibits light-dependent magnetosensitivity. *Nature communications*, 2:356, 2011.

[53] M. Frisch, G. Trucks, H. Schlegel, G. Scuseria, M. Robb, J. Cheeseman, J. Montgomery Jr, T. Vreven, K. Kudin, J. Burant, et al. Gaussian 03, revision c. 02; gaussian, inc.: Wallingford, ct, 2004.(b) frisch, mj et al.

[54] L. Frydman and J. S. Harwood. Isotropic spectra of half-integer quadrupolar spins from bidimensional magic-angle spinning NMR. *Journal of the American Chemical Society*, 117(19):5367–5368, 1995.

[55] C. Gardiner and P. Zoller. *Quantum noise: a handbook of Markovian and non-Markovian quantum stochastic methods with applications to quantum optics*, volume 56. Springer Science & Business Media, 2004.

[56] E. M. Gauger, E. Rieper, J. J. Morton, S. C. Benjamin, and V. Vedral. Sustained quantum coherence and entanglement in the avian compass. *Physical review letters*, 106(4):040503, 2011.

[57] R. J. Gegear, A. Casselman, S. Waddell, and S. M. Reppert. Cryptochrome mediates light-dependent magnetosensitivity in Drosophila. *Nature*, 454(7207):1014, 2008.

[58] B. C. Gilbert and M. Davies. *Electron spin resonance*, volume 14. Royal Society of Chemistry, 1994.

[59] R. E. Gill, T. L. Tibbitts, D. C. Douglas, C. M. Handel, D. M. Mulcahy, J. C. Gottschalck, N. Warnock, B. J. McCaffery, P. F. Battley, and T. Piersma. Extreme endurance flights by landbirds crossing the Pacific Ocean: ecological corridor rather than barrier? *Proceedings of the Royal Society of London B: Biological Sciences*, 276(1656):447–457, 2009.

[60] B. Giovani, M. Byrdin, M. Ahmad, and K. Brettel. Light-induced electron transfer in a cryptochrome blue-light photoreceptor. *Nature Structural and Molecular Biology*, 10(6):489, 2003.

[61] S. K. Gray and D. E. Manolopoulos. Symplectic integrators tailored to the time-dependent Schrödinger equation. *The Journal of chemical physics*, 104(18):7099–7112, 1996.

[62] A. Günther, A. Einwich, E. Sjulstok, R. Feederle, P. Bolte, K.-W. Koch, I. A. Solovyov, and H. Mouritsen. Double-cone localization and seasonal expression pattern suggest a role in magnetoreception for European robin cryptochrome 4. *Current Biology*, 2018.

[63] E. Gwinner. Circannuale Periodik der Mauser und der Zugunruhe bei einem Vogel. *Naturwissenschaften*, 54(15):447–447, 1967.

[64] R. Haberkorn. Density matrix description of spin-selective radical pair reactions. *Molecular Physics*, 32(5):1491–1493, 1976.

[65] B. C. Hall. *Quantum theory for mathematicians*, volume 267. Springer, 2013.

[66] C. M. Hein, S. Engels, D. Kishkinev, and H. Mouritsen. Robins have a magnetic compass in both eyes. *Nature*, 471(7340):E1, 2011.

[67] A. Helbig. Depolarization of natural skylight disrupts orientation of an avian nocturnal migrant. *Experientia*, 46(7):755–758, 1990.

[68] K. B. Henbest, P. Kukura, C. T. Rodgers, P. Hore, and C. R. Timmel. Radio frequency magnetic field effects on a radical recombination reaction: a diagnostic test for the radical pair mechanism. *Journal of the American Chemical Society*, 126(26):8102–8103, 2004.

[69] A. Hilfinger, T. M. Norman, G. Vinnicombe, and J. Paulsson. Constraints on fluctuations in sparsely characterized biological systems. *Physical review letters*, 116(5):058101, 2016.

[70] E. Hill and T. Ritz. Can disordered radical pair systems provide a basis for a magnetic compass in animals? *Journal of The Royal Society Interface*, 7(Suppl 2):S265–S271, 2010.

[71] H. G. Hiscock, T. W. Hiscock, D. R. Kattnig, T. Scrivener, A. M. Lewis, D. E. Manolopoulos, and P. J. Hore. Navigating in low light: Quantum noise in the radical pair compass. *In preparation*.

[72] H. G. Hiscock, D. R. Kattnig, D. E. Manolopoulos, and P. J. Hore. Floquet theory of radical pairs in radiofrequency magnetic fields. *The Journal of Chemical Physics*, 145(12):124117, 2016.

[73] H. G. Hiscock, H. Mouritsen, D. E. Manolopoulos, and P. Hore. Disruption of magnetic compass orientation in migratory birds by radiofrequency electromagnetic fields. *Biophysical journal*, 113(7):1475–1484, 2017.

[74] H. G. Hiscock, S. Worster, D. R. Kattnig, C. Steers, Y. Jin, D. E. Manolopoulos, H. Mouritsen, and P. Hore. The quantum needle of the avian magnetic compass. *Proceedings of the National Academy of Sciences*, 113(17):4634–4639, 2016.

[75] T.-S. Ho, S.-I. Chu, and J. V. Tietz. Semiclassical many-mode Floquet theory. *Chemical Physics Letters*, 96(4):464–471, 1983.

[76] H. J. Hogben, T. Biskup, and P. Hore. Entanglement and sources of magnetic anisotropy in radical pair-based avian magnetoreceptors. *Physical review letters*, 109(22):220501, 2012.

[77] H. J. Hogben, O. Efimova, N. Wagner-Rundell, C. R. Timmel, and P. Hore. Possible involvement of superoxide and dioxygen with cryptochrome in avian

magnetoreception: origin of Zeeman resonances observed by in vivo EPR spectroscopy. *Chemical Physics Letters*, 480(1-3):118–122, 2009.

[78] R. Holland. True navigation in birds: from quantum physics to global migration. *Journal of Zoology*, 293(1):1–15, 2014.

[79] R. A. Holland. Differential effects of magnetic pulses on the orientation of naturally migrating birds. *Journal of The Royal Society Interface*, 7(52):1617–1625, 2010.

[80] J. P. Hoover. Decision rules for site fidelity in a migratory bird, the prothonotary warbler. *Ecology*, 84(2):416–430, 2003.

[81] P. Hore and H. Mouritsen. The radical-pair mechanism of magnetoreception. *Annual review of biophysics*, 45:299–344, 2016.

[82] D. H. Hubel. *Eye, brain, and vision.* Scientific American Library/Scientific American Books, 1995.

[83] S. Ihara. *Information theory for continuous systems*, volume 2. World Scientific, 1993.

[84] F. Illas, I. P. Moreira, C. De Graaf, and V. Barone. Magnetic coupling in biradicals, binuclear complexes and wide-gap insulators: a survey of ab initio wave function and density functional theory approaches. *Theoretical Chemistry Accounts*, 104(3-4):265–272, 2000.

[85] W. P. Irwin and K. J. Lohmann. Disruption of magnetic orientation in hatchling loggerhead sea turtles by pulsed magnetic fields. *Journal of Comparative Physiology A*, 191(5):475–480, 2005.

[86] E. T. Jaynes. Information theory and statistical mechanics. *Physical review*, 106(4):620, 1957.

[87] S. Johnsen and K. J. Lohmann. The physics and neurobiology of magnetoreception. *Nature Reviews Neuroscience*, 6(9):703, 2005.

[88] J. A. Jones and P. J. Hore. Spin-selective reactions of radical pairs act as quantum measurements. *Chemical Physics Letters*, 488(1-3):90–93, 2010.

[89] T. Y. Karogodina, I. G. Dranov, S. V. Sergeeva, D. V. Stass, and U. E. Steiner. Kinetic Magnetic-Field Effect Involving the Small Biologically Relevant Inorganic Radicals NO and O2.-. *ChemPhysChem*, 12(9):1714–1728, 2011.

[90] T. Y. Karogodina, S. V. Sergeeva, and D. V. Stass. Magnetic field effect in the reaction of recombination of nitric oxide and superoxide anion. *Applied Magnetic Resonance*, 36(2-4):195, 2009.

[91] G. Katsoprinakis, A. Dellis, and I. Kominis. Coherent triplet excitation suppresses the heading error of the avian compass. *New Journal of Physics*, 12(8):085016, 2010.

[92] D. R. Kattnig. Unpublished data.

[93] D. R. Kattnig. Radical-pair-based magnetoreception amplified by radical ccavenging: resilience to spin relaxation. *The Journal of Physical Chemistry B*, 121(44):10215–10227, 2017.

[94] D. R. Kattnig and P. Hore. The sensitivity of a radical pair compass magnetoreceptor can be significantly amplified by radical scavengers. *Scientific reports*, 7(1):11640, 2017.

[95] D. R. Kattnig, I. A. Solov'yov, and P. Hore. Electron spin relaxation in cryptochrome-based magnetoreception. *Physical Chemistry Chemical Physics*, 18(18):12443–12456, 2016.

[96] D. R. Kattnig, J. K. Sowa, I. A. Solov'yov, and P. Hore. Electron spin relaxation can enhance the performance of a cryptochrome-based magnetic compass sensor. *New Journal of Physics*, 18(6):063007, 2016.

[97] K. Kavokin. The puzzle of magnetic resonance effect on the magnetic compass of migratory birds. *Bioelectromagnetics*, 30(5):402–410, 2009.

[98] K. Kavokin, N. Chernetsov, A. Pakhomov, J. Bojarinova, D. Kobylkov, and B. Namozov. Magnetic orientation of garden warblers (Sylvia borin) under 1.4 mhz radiofrequency magnetic field. *Journal of the Royal Society Interface*, 11(97):20140451, 2014.

[99] N. Keary, T. Ruploh, J. Voss, P. Thalau, R. Wiltschko, W. Wiltschko, and H.-J. Bischof. Oscillating magnetic field disrupts magnetic orientation in Zebra finches, Taeniopygia guttata. *Frontiers in zoology*, 6(1):25, 2009.

[100] J. Kirschvink. *Sensory Transduction: Society of General Physiologists 45th Annual Symposium: Marine Biological Laboratory, Woods Hole, Massachusetts, 5-8 September 1991*. Rockefeller Univ. Press, 1992.

[101] J. L. Kirschvink. Uniform magnetic fields and double-wrapped coil systems: improved techniques for the design of bioelectromagnetic experiments. *Bioelectromagnetics*, 13(5):401–411, 1992.

[102] J. L. Kirschvink. Nonthermal Levels of Radiation to Biological Systems. *Bioelectromagnetics*, 17:187–194, 1996.

[103] J. L. Kirschvink and J. L. Gould. Biogenic magnetite as a basis for magnetic field detection in animals. *Biosystems*, 13(3):181–201, 1981.

[104] J. L. Kirschvink and M. M. Walker. Particle-size considerations for magnetite-based magnetoreceptors. In *Magnetite biomineralization and magnetoreception in organisms*, pages 243–254. Springer, 1985.

[105] J. L. Kirschvink, M. M. Walker, and C. E. Diebel. Magnetite-based magnetoreception. *Current opinion in neurobiology*, 11(4):462–467, 2001.

[106] D. Kishkinev, N. Chernetsov, D. Heyers, and H. Mouritsen. Migratory reed warblers need intact trigeminal nerves to correct for a 1,000 km eastward displacement. *PLoS One*, 8(6):e65847, 2013.

[107] D. Kishkinev, N. Chernetsov, A. Pakhomov, D. Heyers, and H. Mouritsen. Eurasian reed warblers compensate for virtual magnetic displacement. *Current Biology*, 25(19):R822–R824, 2015.

[108] Y. A. Kram, S. Mantey, and J. C. Corbo. Avian cone photoreceptors tile the retina as five independent, self-organizing mosaics. *PloS one*, 5(2):e8992, 2010.

[109] G. Kramer. Experiments on bird orientation and their interpretation. *Ibis*, 99(2):196–227, 1957.

[110] N. Lambert, S. De Liberato, C. Emary, and F. Nori. Radical-pair model of magnetoreception with spin–orbit coupling. *New Journal of Physics*, 15(8):083024, 2013.

[111] L. D. Landau and E. M. Lifshitz. *Quantum mechanics: non-relativistic theory*, volume 3. Elsevier, 2013.

[112] L. Landler, M. S. Painter, P. W. Youmans, W. A. Hopkins, and J. B. Phillips. Spontaneous magnetic alignment by yearling snapping turtles: rapid association of radio frequency dependent pattern of magnetic input with novel surroundings. *PLoS One*, 10(5):e0124728, 2015.

[113] J. C. Lau, H. J. Hogben, T. Biskup, D. R. Kattnig, P. Hore, et al. Alternative radical pairs for cryptochrome-based magnetoreception. *Journal of The Royal Society Interface*, 11(95):20131063, 2014.

[114] J. C. Lau, C. T. Rodgers, and P. Hore. Compass magnetoreception in birds arising from photo-induced radical pairs in rotationally disordered cryptochromes. *Journal of The Royal Society Interface*, page rsif20120374, 2012.

[115] J. C. Lau, N. Wagner-Rundell, C. T. Rodgers, N. J. Green, and P. Hore. Effects of disorder and motion in a radical pair magnetoreceptor. *Journal of The Royal Society Interface*, page rsif20090399, 2009.

[116] A. A. Lee, J. C. S. Lau, H. J. Hogben, T. Biskup, D. R. Kattnig, and P. J. Hore. Alternative radical pairs for cryptochrome-based magnetoreception. *Journal of The Royal Society Interface*, 11(95), 2014.

[117] N. Lefeldt, D. Dreyer, N.-L. Schneider, F. Steenken, and H. Mouritsen. Migratory blackcaps tested in Emlen funnels can orient at 85 degrees but not at 88 degrees magnetic inclination. *Journal of Experimental Biology*, 218(2):206–211, 2015.

[118] M. Leskes, P. Madhu, and S. Vega. Floquet theory in solid-state nuclear magnetic resonance. *Progress in nuclear magnetic resonance spectroscopy*, 57(4):345–380, 2010.

[119] I. Lestas, G. Vinnicombe, and J. Paulsson. Fundamental limits on the suppression of molecular fluctuations. *Nature*, 467(7312):174, 2010.

[120] T. Levante, M. Baldus, B. Meier, and R. Ernst. Formalized quantum mechanical Floquet theory and its application to sample spinning in nuclear magnetic resonance. *Molecular Physics*, 86(5):1195–1212, 1995.

[121] M. H. Levitt and M. Eden. Numerical simulation of periodic nuclear magnetic resonance problems: fast calculation of carousel averages. *Molecular Physics*, 95(5):879–890, 1998.

[122] C. Levy, B. D. Zoltowski, A. R. Jones, A. T. Vaidya, D. Top, J. Widom, M. W. Young, N. S. Scrutton, B. R. Crane, and D. Leys. Updated structure of Drosophila cryptochrome. *Nature*, 495(7441):E3, 2013.

[123] A. Lewis. Unpublished results.

[124] A. Lewis. *Spin Dynamics in Radical Pairs*. PhD thesis, University of Oxford, 2017.

[125] A. M. Lewis, D. E. Manolopoulos, and P. Hore. Asymmetric recombination and electron spin relaxation in the semiclassical theory of radical pair reactions. *The Journal of Chemical Physics*, 141(4):044111, 2014.

[126] X. Li, Q. Wang, X. Yu, H. Liu, H. Yang, C. Zhao, X. Liu, C. Tan, J. Klejnot, D. Zhong, et al. Arabidopsis cryptochrome 2 (cry2) functions by the photoactivation mechanism distinct from the tryptophan (trp) triad-dependent photoreduction. *Proceedings of the National Academy of Sciences*, 108(51):20844–20849, 2011.

[127] M. Liedvogel, G. Feenders, K. Wada, N. F. Troje, E. D. Jarvis, and H. Mouritsen. Lateralized activation of Cluster N in the brains of migratory songbirds. *European Journal of Neuroscience*, 25(4):1166–1173, 2007.

[128] M. Liedvogel, K. Maeda, K. Henbest, E. Schleicher, T. Simon, C. R. Timmel, P. Hore, and H. Mouritsen. Chemical magnetoreception: bird cryptochrome 1a is excited by blue light and forms long-lived radical-pairs. *PloS one*, 2(10):e1106, 2007.

[129] K. Maeda, K. B. Henbest, F. Cintolesi, I. Kuprov, C. T. Rodgers, P. A. Liddell, D. Gust, C. R. Timmel, and P. Hore. Chemical compass model of avian magnetoreception. *Nature*, 453(7193):387, 2008.

[130] K. Maeda, A. J. Robinson, K. B. Henbest, H. J. Hogben, T. Biskup, M. Ahmad, E. Schleicher, S. Weber, C. R. Timmel, and P. Hore. Magnetically sensi-

tive light-induced reactions in cryptochrome are consistent with its proposed role as a magnetoreceptor. *Proceedings of the National Academy of Sciences*, 109(13):4774–4779, 2012.

[131] E. P. Malkemper, S. H. Eder, S. Begall, J. B. Phillips, M. Winklhofer, V. Hart, and H. Burda. Magnetoreception in the wood mouse (Apodemus sylvaticus): influence of weak frequency-modulated radio frequency fields. *Scientific reports*, 5:9917, 2015.

[132] D. E. Manolopoulos and P. Hore. An improved semiclassical theory of radical pair recombination reactions. *The Journal of chemical physics*, 139(12):124106, 2013.

[133] J. I. Martínez, P. J. Alonso, C. Gómez-Moreno, and M. Medina. One- and two-dimensional ESEEM spectroscopy of flavoproteins. *Biochemistry*, 36(49):15526–15537, 1997.

[134] J. I. Martínez, P. J. Alonso, and M. Medina. The electronic structure of the neutral isoalloxazine semiquinone within Anabaena flavodoxin: New insights from HYSCORE experiments. *Journal of Magnetic Resonance*, 218:153–162, 2012.

[135] J. G. Mather and R. R. Baker. Magnetic sense of direction in woodmice for route-based navigation. *Nature*, 291(5811):152, 1981.

[136] M. McElhinny and P. L. McFadden. *The magnetic field of the earth: paleomagnetism, the core, and the deep mantle*, volume 63. Academic Press, 1998.

[137] B. R. McGarvey. The isotropic hyperfine interaction. *The Journal of Physical Chemistry*, 71(1):51–66, 1967.

[138] K. A. McLauchlan and U. Steiner. Invited article: the spin-correlated radical pair as a reaction intermediate. *Molecular Physics*, 73(2):241–263, 1991.

[139] C. Mettke-Hofmann and E. Gwinner. Long-term memory for a life on the move. *Proceedings of the National Academy of Sciences*, 100(10):5863–5866, 2003.

[140] F. R. Moore. Sunset and the orientation behaviour of migrating birds. *Biological Reviews*, 62(1):65–86, 1987.

[141] C. V. Mora, M. Davison, J. M. Wild, and M. M. Walker. Magnetoreception and its trigeminal mediation in the homing pigeon. *Nature*, 432(7016):508, 2004.

[142] H. Mouritsen. Spatiotemporal orientation strategies of long-distance migrants. In *Avian migration*, pages 493–513. Springer, 2003.

[143] H. Mouritsen. Sensory biology: search for the compass needles. *Nature*, 484(7394):320, 2012.

[144] H. Mouritsen. Magnetoreception in birds and its use for long-distance migration. In *Sturkie's Avian Physiology (Sixth Edition)*, pages 113–133. Elsevier, 2015.

[145] H. Mouritsen, G. Feenders, M. Liedvogel, K. Wada, and E. D. Jarvis. Night-vision brain area in migratory songbirds. *Proceedings of the National Academy of Sciences of the United States of America*, 102(23):8339–8344, 2005.

[146] H. Mouritsen, U. Janssen-Bienhold, M. Liedvogel, G. Feenders, J. Stalleicken, P. Dirks, and R. Weiler. Cryptochromes and neuronal-activity markers colocalize in the retina of migratory birds during magnetic orientation. *Proceedings of the National Academy of Sciences of the United States of America*, 101(39):14294–14299, 2004.

[147] H. Mouritsen and O. N. Larsen. Migrating songbirds tested in computer-controlled Emlen funnels use stellar cues for a time-independent compass. *Journal of Experimental Biology*, 204(22):3855–3865, 2001.

[148] R. Muheim, J. Bäckman, and S. Åkesson. Magnetic compass orientation in European robins is dependent on both wavelength and intensity of light. *Journal of Experimental Biology*, 205(24):3845–3856, 2002.

[149] P. Müller, J. Yamamoto, R. Martin, S. Iwai, and K. Brettel. Discovery and functional analysis of a 4th electron-transferring tryptophan conserved exclusively in animal cryptochromes and (6-4) photolyases. *Chemical Communications*, 51(85):15502–15505, 2015.

[150] C. Nielsen, D. R. Kattnig, E. Sjulstok, P. Hore, and I. A. Solov'yov. Ascorbic acid may not be involved in cryptochrome-based magnetoreception. *Journal of The Royal Society Interface*, 14(137):20170657, 2017.

[151] M. A. Nielsen and I. Chuang. Quantum computation and quantum communication, 2000.

[152] C. Nießner, S. Denzau, J. C. Gross, L. Peichl, H.-J. Bischof, G. Fleissner, W. Wiltschko, and R. Wiltschko. Avian ultraviolet/violet cones identified as probable magnetoreceptors. *PLoS One*, 6(5):e20091, 2011.

[153] C. Nießner, J. C. Gross, S. Denzau, L. Peichl, G. Fleissner, W. Wiltschko, and R. Wiltschko. Seasonally changing cryptochrome 1b expression in the retinal ganglion cells of a migrating passerine bird. *PloS one*, 11(3):e0150377, 2016.

[154] C. Nießner and M. Winklhofer. Radical-pair-based magnetoreception in birds: radio-frequency experiments and the role of cryptochrome. *Journal of Comparative Physiology A*, 203(6-7):499–507, 2017.

[155] D. C. Outlaw, G. Voelker, B. Mila, and D. J. Girman. Evolution of long-distance migration in and historical biogeography of Catharus thrushes: a molecular phylogenetic approach. *The Auk*, 120(2):299–310, 2003.

[156] N. Ozturk, C. P. Selby, Y. Annayev, D. Zhong, and A. Sancar. Reaction mechanism of Drosophila cryptochrome. *Proceedings of the National Academy of Sciences*, 108(2):516–521, 2011.

[157] N. Ozturk, C. P. Selby, D. Zhong, and A. Sancar. Mechanism of photosignaling by Drosophila cryptochrome role of the redox status of the flavin chromophore. *Journal of Biological Chemistry*, 289(8):4634–4642, 2014.

[158] A. Pakhomov, J. Bojarinova, R. Cherbunin, R. Chetverikova, P. S. Grigoryev, K. Kavokin, D. Kobylkov, R. Lubkovskaja, and N. Chernetsov. Very weak oscillating magnetic field disrupts the magnetic compass of songbird migrants. *Journal of The Royal Society Interface*, 14(133):20170364, 2017.

[159] J. A. Pauls, Y. Zhang, G. P. Berman, and S. Kais. Quantum coherence and entanglement in the avian compass. *Physical Review E*, 87(6):062704, 2013.

[160] J. B. Pedersen, C. Nielsen, and I. A. Solovyov. Multiscale description of avian migration: from chemical compass to behaviour modeling. *Scientific reports*, 6:36709, 2016.

[161] J. Phillips and O. Sayeed. Wavelength-dependent effects of light on magnetic compass orientation in Drosophila melanogaster. *Journal of Comparative Physiology A*, 172(3):303–308, 1993.

[162] J. B. Phillips and S. C. Borland. Behavioural evidence for use of a light-dependent magnetoreception mechanism by a vertebrate. *Nature*, 359(6391):142, 1992.

[163] W. H. Press. *Numerical recipes 3rd edition: The art of scientific computing*. Cambridge university press, 2007.

[164] O. Riordan. Private communication.

[165] T. Ritz, S. Adem, and K. Schulten. A model for photoreceptor-based magnetoreception in birds. *Biophysical journal*, 78(2):707–718, 2000.

[166] T. Ritz, M. Ahmad, H. Mouritsen, R. Wiltschko, and W. Wiltschko. Photoreceptor-based magnetoreception: optimal design of receptor molecules, cells, and neuronal processing. *Journal of the Royal Society Interface*, 7(Suppl 2):S135–S146, 2010.

[167] T. Ritz, P. Thalau, J. B. Phillips, R. Wiltschko, and W. Wiltschko. Resonance effects indicate a radical-pair mechanism for avian magnetic compass. *Nature*, 429(6988):177, 2004.

[168] T. Ritz, R. Wiltschko, P. Hore, C. T. Rodgers, K. Stapput, P. Thalau, C. R. Timmel, and W. Wiltschko. Magnetic compass of birds is based on a molecule with optimal directional sensitivity. *Biophysical journal*, 96(8):3451–3457, 2009.

[169] C. T. Rodgers. *Magnetic Field Effects in Chemical Systems*. PhD thesis, University of Oxford, 2007.

[170] C. T. Rodgers, K. B. Henbest, P. Kukura, C. R. Timmel, and P. Hore. Low-field optically detected EPR spectroscopy of transient photoinduced radical pairs. *The Journal of Physical Chemistry A*, 109(23):5035–5041, 2005.

[171] C. T. Rodgers and P. J. Hore. Chemical magnetoreception in birds: the radical pair mechanism. *Proceedings of the National Academy of Sciences*, 106(2):353–360, 2009.

[172] C. T. Rodgers, S. A. Norman, K. B. Henbest, C. R. Timmel, and P. Hore. Determination of radical re-encounter probability distributions from magnetic field effects on reaction yields. *Journal of the American Chemical Society*, 129(21):6746–6755, 2007.

[173] A. Sancar. Structure and function of DNA photolyase. *Biochemistry*, 33(1):2–9, 1994.

[174] R. Santra and L. S. Cederbaum. Non-hermitian electronic theory and applications to clusters. *Physics reports*, 368(1):1–117, 2002.

[175] I. Scholz, J. D. van Beek, and M. Ernst. Operator-based floquet theory in solid-state NMR. *Solid state nuclear magnetic resonance*, 37(3-4):39–59, 2010.

[176] K. Schulten, H. Staerk, A. Weller, H.-J. Werner, and B. Nickel. Magnetic field dependence of the geminate recombination of radical ion pairs in polar solvents. *Zeitschrift für Physikalische Chemie*, 101(1-6):371–390, 1976.

[177] K. Schulten, C. E. Swenberg, and A. Weller. A biomagnetic sensory mechanism based on magnetic field modulated coherent electron spin motion. *Zeitschrift für Physikalische Chemie*, 111(1):1–5, 1978.

[178] K. Schulten and P. G. Wolynes. Semiclassical description of electron spin motion in radicals including the effect of electron hopping. *The Journal of Chemical Physics*, 68(7):3292–3297, 1978.

[179] S. Schwarze, N.-L. Schneider, T. Reichl, D. Dreyer, N. Lefeldt, S. Engels, N. Baker, P. Hore, and H. Mouritsen. Weak broadband electromagnetic fields are more disruptive to magnetic compass orientation in a night-migratory songbird (Erithacus rubecula) than strong narrow-band fields. *Frontiers in behavioral neuroscience*, 10:55, 2016.

[180] C. E. Shannon. A mathematical theory of communication (parts I and II). *Bell System Tech. J.*, 27:379–423, 1948.

[181] C. E. Shannon. Coding theorems for a discrete source with a fidelity criterion. *IRE Nat. Conv. Rec*, 4(142-163):1, 1959.

[182] J. Shirley. *Interaction of a Quantum System with a strong oscillating field*. PhD thesis, California Institute of Technology, 1963.

[183] J. H. Shirley. Solution of the Schrödinger equation with a Hamiltonian periodic in time. *Physical Review*, 138(4B):B979, 1965.

[184] I. Solov'yov, P. J. Hore, T. Ritz, and K. Schulten. Chemical compass for bird navigation. In *Quantum effects in biology*, pages 218–236. Cambridge University Press, 2014.

[185] I. A. Solov'yov, H. Mouritsen, and K. Schulten. Acuity of a cryptochrome and vision-based magnetoreception system in birds. *Biophysical journal*, 99(1):40–49, 2010.

[186] I. A. Solov'yov and K. Schulten. Magnetoreception through cryptochrome may involve superoxide. *Biophysical journal*, 96(12):4804–4813, 2009.

[187] I. A. Solovyov, D. E. Chandler, and K. Schulten. Magnetic field effects in Arabidopsis thaliana cryptochrome-1. *Biophysical Journal*, 92(8):2711–2726, 2007.

[188] I. A. Solovyov and W. Greiner. Theoretical analysis of an iron mineral-based magnetoreceptor model in birds. *Biophysical Journal*, 93(5):1493–1509, 2007.

[189] I. A. Solovyov and W. Greiner. Iron-mineral-based magnetoreceptor in birds: polarity or inclination compass? *The European Physical Journal D*, 51(1):161–172, 2009.

[190] U. E. Steiner and T. Ulrich. Magnetic field effects in chemical kinetics and related phenomena. *Chemical Reviews*, 89(1):51–147, 1989.

[191] A. M. Stoneham, E. M. Gauger, K. Porfyrakis, S. C. Benjamin, and B. W. Lovett. A new type of radical-pair-based model for magnetoreception. *Biophysical journal*, 102(5):961–968, 2012.

[192] P. Thalau, T. Ritz, H. Burda, R. E. Wegner, and R. Wiltschko. The magnetic compass mechanisms of birds and rodents are based on different physical principles. *Journal of the royal Society Interface*, 3(9):583–587, 2006.

[193] P. Thalau, T. Ritz, K. Stapput, R. Wiltschko, and W. Wiltschko. Magnetic compass orientation of migratory birds in the presence of a 1.315 mhz oscillating field. *Naturwissenschaften*, 92(2):86–90, 2005.

[194] R. J. Thomas, T. Széskely, I. C. Cuthill, D. G. Harper, S. E. Newson, T. D. Frayling, and P. D. Wallis. Eye size in birds and the timing of song at dawn. *Proceedings of the Royal Society of London B: Biological Sciences*, 269(1493):831–837, 2002.

[195] U. Till, C. Timmel, B. Brocklehurst, and P. Hore. The influence of very small magnetic fields on radical recombination reactions in the limit of slow recombination. *Chemical physics letters*, 298(1-3):7–14, 1998.

[196] C. Timmel, F. Cintolesi, B. Brocklehurst, and P. Hore. Model calculations of magnetic field effects on the recombination reactions of radicals with anisotropic hyperfine interactions. *Chemical physics letters*, 334(4-6):387–395, 2001.

[197] C. Timmel, U. Till, B. Brocklehurst, K. McLauchlan, and P. Hore. Effects of weak magnetic fields on free radical recombination reactions. *Molecular Physics*, 95(1):71–89, 1998.

[198] M. Vácha, T. Pužová, and D. Drštková. Effect of light wavelength spectrum on magnetic compass orientation in Tenebrio molitor. *Journal of Comparative Physiology A*, 194(10):853, 2008.

[199] M. Vácha, T. Pužová, and M. Kvíćalová. Radio frequency magnetic fields disrupt magnetoreception in American cockroach. *Journal of Experimental Biology*, 212(21):3473–3477, 2009.

[200] A. F. Voter. Introduction to the kinetic Monte Carlo method. In *Radiation effects in solids*, pages 1–23. Springer, 2007.

[201] H. Wagner and F. Sauer. Die Sternenorientierung nächtlich ziehender grasmücken (sylvia atricapilla, borin und curruca). *Ethology*, 14(1):29–70, 1957.

[202] M. M. Walker, T. E. Dennis, and J. L. Kirschvink. The magnetic sense and its use in long-distance navigation by animals. *Current opinion in neurobiology*, 12(6):735–744, 2002.

[203] Z. B. Walters. Quantum dynamics of the avian compass. *Physical Review E*, 90(4):042710, 2014.

[204] E. J. Warrant. Seeing better at night: life style, eye design and the optimum strategy of spatial and temporal summation. *Vision research*, 39(9):1611–1630, 1999.

[205] S. Weber, K. Möbius, G. Richter, and C. W. Kay. The electronic structure of the flavin cofactor in DNA photolyase. *Journal of the American Chemical Society*, 123(16):3790–3798, 2001.

[206] M. B. Wilk and R. Gnanadesikan. Probability plotting methods for the analysis for the analysis of data. *Biometrika*, 55(1):1–17, 1968.

[207] R. Wiltschko. *Magnetic orientation in animals*, volume 33. Springer Science & Business Media, 2012.

[208] R. Wiltschko, M. Ahmad, C. Nießner, D. Gehring, and W. Wiltschko. Light-dependent magnetoreception in birds: the crucial step occurs in the dark. *Journal of The Royal Society Interface*, 13(118):20151010, 2016.

[209] R. Wiltschko, K. Stapput, P. Thalau, and W. Wiltschko. Directional orientation of birds by the magnetic field under different light conditions. *Journal of the Royal Society Interface*, page rsif20090367, 2009.

[210] R. Wiltschko, P. Thalau, D. Gehring, C. Nießner, T. Ritz, and W. Wiltschko. Magnetoreception in birds: the effect of radio-frequency fields. *Journal of The Royal Society Interface*, 12(103):20141103, 2015.

[211] W. Wiltschko. Über den Einfluß statischer Magnetfelder auf die Zugorientierung der Rotkehlchen (Erithacus rubecula). *Ethology*, 25(5):537–558, 1968.

[212] W. Wiltschko, U. Munro, H. Ford, and R. Wiltschko. Red light disrupts magnetic orientation of migratory birds. *Nature*, 364(6437):525, 1993.

[213] W. Wiltschko and R. Wiltschko. Magnetic compass of European robins. *Science*, 176(4030):62–64, 1972.

[214] W. Wiltschko and R. Wiltschko. Magnetic orientation in birds. *Journal of Experimental Biology*, 199(1):29–38, 1996.

[215] W. Wiltschko and R. Wiltschko. The effect of yellow and blue light on magnetic compass orientation in european robins, erithacus rubecula. *Journal of Comparative Physiology A*, 184(3):295–299, 1999.

[216] W. Wiltschko and R. Wiltschko. Light-dependent magnetoreception in birds: the behaviour of European robins, Erithacus rubecula, under monochromatic light of various wavelengths and intensities. *Journal of Experimental Biology*, 204(19):3295–3302, 2001.

[217] M. Winklhofer, E. Dylda, P. Thalau, W. Wiltschko, and R. Wiltschko. Avian magnetic compass can be tuned to anomalously low magnetic intensities. *Proceedings of the Royal Society of London B: Biological Sciences*, 280(1763):20130853, 2013.

[218] S. Worster, D. R. Kattnig, and P. Hore. Spin relaxation of radicals in cryptochrome and its role in avian magnetoreception. *The Journal of Chemical Physics*, 145(3):035104, 2016.

[219] S. Worster, H. Mouritsen, and P. Hore. A light-dependent magnetoreception mechanism insensitive to light intensity and polarization. *Journal of The Royal Society Interface*, 14(134):20170405, 2017.

[220] B.-M. Xu, J. Zou, H. Li, J.-G. Li, and B. Shao. Effect of radio frequency fields on the radical pair magnetoreception model. *Physical Review E*, 90(4):042711, 2014.

[221] T. Yoshii, M. Ahmad, and C. Helfrich-Förster. Cryptochrome mediates light-dependent magnetosensitivity of drosophila's circadian clock. *PLoS biology*, 7(4):e1000086, 2009.

[222] M. Zapka, D. Heyers, C. M. Hein, S. Engels, N.-L. Schneider, J. Hans, S. Weiler, D. Dreyer, D. Kishkinev, J. M. Wild, et al. Visual but not trigeminal mediation of magnetic compass information in a migratory bird. *Nature*, 461(7268):1274, 2009.

[223] M. Zapka, D. Heyers, M. Liedvogel, E. D. Jarvis, and H. Mouritsen. Night-time neuronal activation of Cluster N in a day-and night-migrating songbird. *European Journal of Neuroscience*, 32(4):619–624, 2010.

[224] Y. Zhang, G. P. Berman, and S. Kais. Sensitivity and entanglement in the avian chemical compass. *Physical Review E*, 90(4):042707, 2014.

[225] B. D. Zoltowski, A. T. Vaidya, D. Top, J. Widom, M. W. Young, and B. R. Crane. Structure of full-length Drosophila cryptochrome. *Nature*, 480(7377):396, 2011.